Università degli Studi di Perugia

Dottorato in Fisica e Tecnologie fisiche - Ciclo XXVIII

Time dependence of electrons and positrons fluxes measured with the AMS-02 spectrometer

Relatore:
Bruna Bertucci

Autore:
Maura Graziani

Correlatore:
Matteo Duranti

Coordinatore del Corso di Dottorato: Maurizio Busso

Anno Accademico 2014 - 2015

Contents

Introduction

The Alpha Magnetic Spectrometer, AMS-02, is a general purpose high energy particle physics detector. It was launched into space with the Space Shuttle STS-134 mission and installed onboard the ISS in 2011, on May 19*th*, to conduct a unique long duration mission of fundamental physics research in space. The experimental challenge of this spectrometer is the accurate measurement of the Cosmic Rays (CR) composition and energy spectra, up to the TeV energy scale, that could reveal the presence of primordial anti-matter or give the signature of exotic sources, as for example secondaries from dark matter annihilation.

In this thesis, we present the precision measurement of the time dependency induced by solar activity on electrons and positron fluxes at energies below 40 GeV based on the analysis of the first 30 months of AMS-02 collected data.

Electrons (e^-) and positrons (e^+) are a rare component of the cosmic radiation since they represent only a $\sim 1\%$ and $\sim 0.1\%$ of the total CR flux, which is dominated by protons (90%) and alpha particles (8%). From the experimental point of view is therefore a challenge to select their signals and to collect an adequate statistics. In spite of this, a constant effort has been put in their measurement since decades due to the unique knowledge that they can bring on CR astrophysical sources and InterStellar Medium (ISM) properties as well as for their potential in probing new exotic sources.
Due to their low mass, $e^{\pm}$ suffer of dramatic energy losses due to the interactions with the magnetic field and background photons in the ISM: high energy $e^{\pm}$ observed near earth are therefore of galactic origin and their sources are mostly located within few kpc. In the most common astrophysical models, e^- are mainly of primary origin, i.e. produced and accelerated in astrophysical sources, whereas e^+ are mostly produced in the interactions of protons and nuclei with the ISM material: their flux is faint and expected to extinguish more rapidly with increasing energy with

respect to that of e^-. These features make the e^+ a sensitive channel for indirect Dark Matter detection or to search for new astrophysical sources.

However, $e^\pm$ spectra, when measured near Earth, are significantly affected by the solar activity and subject to the so-called *solar modulation* (SM) effect. The solar activity has a cycle which period is ~ 11 years, during which it increases reaching a maximum and then decreases again. The intensity of cosmic ray radiation is correlated (or rather anticorrelated) with the activity of the sun.

In order to have a correct understanding of spectra of $e^\pm$ out of the heliosphere, the SM should be well known and taken into account. A detailed study of the $e^\pm$ fluxes evolution with time is needed in order to develop and test different models of the SM effects based on the interaction of cosmic rays with the heliosphere and to study the charge-sign dependent modulation effects. Most of previous studies on charge-sign dependence of the solar modulation compared the combined $e^- + e^+$ flux time behaviour with that of CR protons and helium of the same rigidity. However, only simultaneous measurements of e^- and e^+ (or protons and anti-protons) over a complete solar activity cycle can represent a sound test of the current charge-sign dependent modulation models.

AMS-02 can provide the most accurate measurements of the time dependence of electron and positron fluxes since 2011 thanks to its high acceptance and the excellent performances of the detector. In this work, we fully take advantage of the AMS-02 performances to carry out the first precision measurement of charge sign dependent effects in e^+ and e^-.

After an overview on the Cosmic Rays physics (Chapter 1), we will introduce the main characteristics of the AMS-02 instrument (Chapter 2). The approach used for the measurement will be then discussed (Chapter 3) defining all the elements that will enter in the flux definition, in particular the detector acceptance and exposure time calculation. The event selection and the techniques used to distinguish $e^\pm$ signal from proton background will be then presented in detail (Chapter 4) as well as the time-dependent analysis (Chapter 5). Discussion of the results and their measurement uncertainties (Chapter 6) will conclude this dissertation.

Chapter 1

Cosmic Rays

Cosmic Rays are charged particles with galactic and extragalactic origin that reach the Earth atmosphere from all directions. During the travel from their source to the Earth, the CRs undergo to energy losses and acceleration processes due to their interaction with matter and magnetic fields present in the interstellar medium.
The CRs that reach the Earth are mainly constituted by protons ($\sim$ 90%), helium nuclei ($\sim$ 8%), electrons ($\sim$ 1%), $\sim$ 1% of nuclei and traces of anti-matter (positrons, antiprotons) that has been produced in the interaction of the CRs with the interstellar medium.

The observed spectra of the CRs reach energies up to 10^{19} eV and their understanding requires a deep knoledge of the origin and propagation of the cosmic rays themselves.

CRs constitute a unique tool to understand the various energetic processes and the sources present in the universe. For electrons and positrons, due to their small mass compared to the proton mass, the radiative energy losses are much stronger than the radiative losses of protons and nuclei. This make electrons and positrons sensitive to nearby sources like pulsars or supernova remnants (SNR) in the range of the order of only 1 Kpc. Moreover, they can be used for the indirect detection of dark matter or other exotic sources.
For all these reasons, electrons and positrons cover a particular importance in the astrophysics.

However, Solar modulation has a relevant effect on the cosmic-ray spectra at low energies (<20 GeV) and should be studied in order to have the correct understanding of the primary cosmic electrons and positrons spectra.

This section is dedicated to the cosmic radiation. After a brief history of the Cosmic Rays, the properties of the energy spectra, the origin and propagation and the solar modulation of CRs will be discussed, focusing on the electrons and positrons component.

1.1 A brief history of Cosmic Ray

The history of the discovery of cosmic rays could start in 1900 when was observed that electroscopes discharge even if they are kept in the dark well away from sources of natural radioactivity. In 1910 Wulf compares the radiation at the bottom and the top of the Eiffel Tower in order to test the hypothesis according which, since the natural radiation sources are on the ground, if one moves far away enough from those sources should be detected less radiation. The result that he found was the opposite: the ionization fell from 6 ions per cm^{-3} to 3.5 ions per cm^{-3} as he ascended the Eiffel Tower (330 m). However his results were not initially accepted.

A big improvements occurred when first Hess (in 1912) and then Kolhörster flown respectively up to 5 Km and up to 9 Km in open balloons. Hess and Kolhörster found the startling result that the average ionisation increased with respect to the ionisation at sea-level above about 1.5 km. This was a clear evidence that the radiation observed was coming from above the Earth's atmosphere, from the space. For this reason the particles that constitute this radiation were called *Cosmic Rays*.

Before the building of the first accelerators in 1950, the *Cosmic Rays* constituted a unique laboratory for the discovery of new particles. Anderson in 1932 and Blackett and Occhialini in 1933 discovered the positron, already predicted by the Dirac's theory of the electrons. Evidence for particles closely resembling the mesons predicted by Yukawa were found in the late 1930s and measurements of the amount of ionisation led to estimates of their mass of about 200 m_e. In 1947, were observed the π and μ mesons. In particular, the late 1940s was an exciting epoch for the cosmic ray physic since cosmic rays provided a readily available source of very high energy particles and through the nuclear emulsion technique many new types of particles were discovered.

By 1953, the accelerators technology had been developed to the point where energies comparable to those available in the cosmic rays could be produced in the laboratory with known energies and directed precisely onto the chosen target. After about 1953, the future of high energy physics lay in the accelerators rather than in the use of cosmic rays. Interest in cosmic rays was shifted to the problems of their origin, chemical composition and their propagation in astrophysical environments from their sources to the Earth. All these questions are still matter of intense research. Moreover, it was known that the observed cosmic rays at the surface of the Earth are secondary (or higher) products from the single cosmic rays entering the top of the atmosphere. The study was revolutionized starting from 1960 with the development of rockets and satellites which could stay outside the atmosphere for a long period and allowed to study the primary cosmic rays.

1.2 Modern detection of Cosmic Rays

Figure 1.1 shows a scheme of the various technique used to the detection of cosmic rays.

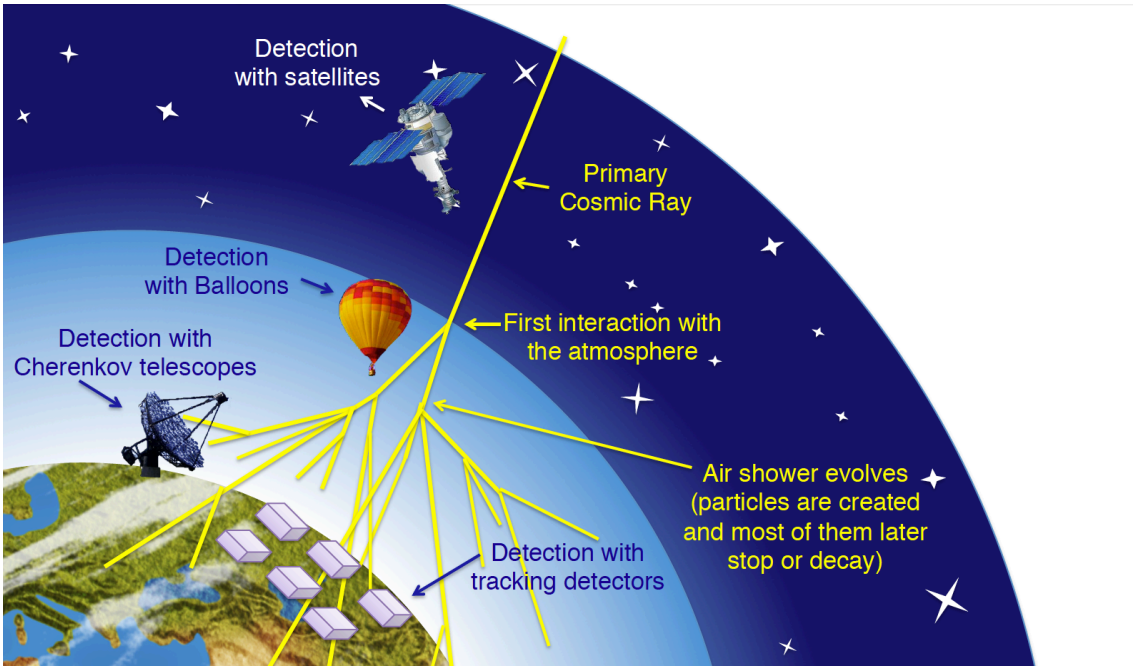

FIGURE 1.1: Illustration of the various instrumentations and techniques used to detect cosmic rays.

The experimental cosmic ray physics is divided in two different observational categories: satellite or balloon experiments, and ground experiments. For energies up

to several hundreds of TeV, the intensity of the flux is high enough to consider experiments in space or high up in the atmosphere to measure the arriving particles. Above these energies, the big surfaces or/and long exposure times required to provide statistically significant measurements of the arriving flux are not yet technologically achievable in space.
The solution is then to move to indirect detection from ground of the extensive air showers produced when cosmic rays interact with the constituents of the atmosphere.

1.2.1 Balloon Flights

Since the first balloon flights have measured cosmic rays in the nineties, the technological progress has been tremendous and balloons remain a very popular approach to cosmic-ray studies. Balloon missions are both cheaper and often more convenient to conduct than space experiments. Some of the most important measurements remain referenced by balloon measurements, such as nuclei isotopic compositions and secondary to primary nuclei ratios. One of the main difficulties in interpreting balloon measurements is to deal with the presence of a given amount of residual atmosphere which requires to accurately model the resulting interactions cosmic rays may undergo before being detected.

ATIC
The Advanced Thin Ionization Calorimeter (ATIC) is an experiment primarily devoted to the measurement of energy and composition of cosmic rays. It is composed of several layers of bismuth germanate scintillating material that allows to measure the particle energy, while the charge is obtained using a silicon matrix. ATIC completed three successful flights since the year 2000 and was able to measure the energy spectra of nuclei up to iron from 50 GeV to hundreds of TeV. ATIC also published in 2008 [1] the observation of an excess of electrons in the energy range 300 to 800 GeV compared to the expected galactic background. Since ATIC cannot distinguish electrons from positrons, this result can be compatible with the famous positron excess measured the same year by the PAMELA collaboration [2], the Fermi LAT experiment [3], and more recently confirmed by AMS-02 [4, 5].

CREAM
The Cosmic Ray Energetics and Mass experiment (CREAM) consists of various particle physics detectors optimized to discriminate nuclei from proton to iron in a

range of energy between $10^{11}\,eV$ and $10^{15}\,eV$. The balloon was flown successfully six times above Antarctica at an altitude ranging between 38 and 40 Km, above roughly 99.5% of the atmosphere. The energy range covered is large and intended to overlap the region where air shower detections can be adopted. Direct measurements at these energies have the potential to provide an energy calibration for the indirect measurements. The instrument consists of several complementary detecting devices: a Timing Charge Detector, a Cerenkov Detector, a Transition Radiation Detector, a Cerenkov Camera, a Silicon Charge Detector, scintillating fiber hodoscopes, and a tungsten-scintillating fiber calorimeter. CREAM has up to now produced the best measurements of secondary to primary nuclei ratios [6], an essential information for the constraint of cosmic ray propagation models.

1.2.2 Satellite Experiments

For a long time, the technology of particle physics detection on ground was judged too challenging to be implemented in space. The majority of space experiments were dedicated solely to the measurement of the cosmic electro-magnetic radiation or to the exploration of the Earth magnetic structure. The qualification flight of the AMS experiment in 1998 validated the use of modern particle physics technology in space. The PAMELA instrument was however the first long duration particle physics experiment in space.

PAMELA

The Payload for Anti-Matter and Light-nuclei Astrophysics (PAMELA) is an Italian particle detector that has been taking data in space since June 2006. It is installed on the Russian satellite Resurs-DK1 and follows an orbit at an altitude between 350 Km and 610 Km. With its magnetic spectrometer, it was the first experiment to measure with high precision cosmic antimatter. The instrument combines a plurality of particle physics detection techniques, such as a Magnetic Spectrometer, based on a neodymion-iron-boron permanent magnet and a precision tracking system, a sampling imaging Calorimeter, a Time of Flight Sysmtem, an anti-coincidence system made of plastic scintillation counters, and a dedicated neutron counter.
The PAMELA measurements led the route to several unexpected results. Most famous is the observed excess in the positron to electron ratio [2], starting at an energy of about 50 GeV which was later confirmed by FERMI [3] and AMS-02 [4, 5]. PAMELA also measured a break in the spectral index of proton and helium nuclei,

challenging the standard view of a smooth power-law spectrum for all cosmic species up to the knee.

FERMI

The FERMI instrument, previously named GLAST, consists of a Large Area Telescope (LAT) and a Gamma Ray Burst Monitor (GBR). The LAT is the main instrument on-board and comprises a tracker and calorimeter system that allows to perform precise measurements of the arrival direction and energy of photons that convert into electron-positron pairs in the detector material. The energy range covered by the LAT is between 10 KeV and 300 GeV.

The conversion is ensured by high-Z conversion foils placed on top of the tracker planes. Anticoincidence counters allow to select photons against the high background of charged particles (up to a thousand time more abundant). The main goal of FERMI is to measure the diffuse galactic $\gamma - ray$ emission and various $\gamma - ray$ sources. Such measurements have the potential to bring crucial information to the cosmic ray picture. Despite the fact that the detector is optimized for photon detection in the GeV range, it can also detect electrons. Without a magnet on-board, it is not possible to separate directly electrons from positrons. However, the FERMI collaboration was able to distinguish the two leptonic components using the properties of the Earth magnetic field. This allowed the collaboration to measure the ratio of positron to electrons up to 870 GeV [3] and confirm the excess observed by PAMELA.

The Alpha Magnetic Spectrometer The AMS story starts with a precursor flight in 1998 with a reduced qualification model (AMS-01) of what was designed to be the final AMS-02 instrument. The AMS-01 detector was flown on-board the Space Shuttle Discovery during the STS-91 mission, demonstrating the feasibility of large-scale particle physics detectors in space. AMS-01 successfully collected more than 100 million particles which led to several publications. Based on the experience gained from AMS-01, AMS-02 took another 14 years to be built. It is now taking data on the International Space Station and has set the new reference for precision measurements in space. AMS covers a variety of physics topics such as heavy anti-matter, dark matter, cosmic ray chemical composition and anisotropies, as well photon studies. The AMS project is reviewed in deep in section 2.

Next: DAMPE, ISS CREAM and HERD The Dark Matter Particle Explorer (**DAMPE**) is one of the five satellite missions of the Chinese Academy of

Sciences (CAS) space science program, with a launch date planned to be in 2015-2016. DAMPE is designed to increase the sensitivity and energy reach for electrons, photons and cosmic ray particles (proton and heavy nuclei). The energy range is planned to be from 5 GeV to 10 TeV for electrons and photons and 100 GeV to 100 TeV for cosmic ray nuclei, with extremely good energy resolution. The main scientific goals of DAMPE are to identify potential Dark Matter signatures and help in the understanding of the origin and propagation mechanisms of high energy cosmic rays, as well as potential new discoveries in high energy gamma astronomy.

ISS-Cream is a mission based on a transformation of the **CREAM** 1.2.1 instrument for accommodation on the International Space Station (ISS). The goal is to extend the energy range of direct measurements of cosmic rays to the highest energy possible, around 10^{14} eV, very close to the knee. The long exposure above the atmosphere offers orders of magnitude greater statistics without the secondary particle background inherent to balloon experiments. A launch of ISS-CREAM instrument is scheduled for 2015 on a SpaceX service flight to the ISS. The launch site is Cape Canaveral, FL.

The High Energy Cosmic Radiation Detection facility (**HERD**) is planned for launch and installation onboard the chinese space station around 2020. HERD will perform accurate, high statistics measurements of electrons, $\gamma - rays$ up to TeV energies and cosmic ray nuclei up to PeV energies. Extending the direct measurements of cosmic rays to energies around the knee may have the potential to improve fundamentally our understanding of the cosmic ray picture. The disentanglement of the various cosmic ray components at these energies will help to discriminate different theoretical models.

1.2.3 Ground-based Detectors

When a cosmic ray enters in the Earth's atmosphere, it interacts with its constituents and forms an extensive air shower. Electromagnetic showers initiated by photons or electrons can be distinguished from hadron showers based on several observable properties.

Different detection techniques can be used. The classical approach uses an array of scintillation detectors which measures the local density of charged particles at ground, which allows in turn to estimate the position of the shower core and the

total number of particles in the shower. The latter is directly correlated to the particle energy. Combined with measurements of the arrival time of the particles at neighboring detectors, it is possible to reconstruct the arrival direction of the primary particle. Examples of experiments using such technologies are the KASKADE [7], KASKADE-Grande [8] or the older AGASA [9]. With arrays of few hundreds of scintillation detectors, they measure cosmic rays with energies around the knee up to around 10^{18} eV.

Based on the same shower reconstruction methodology, another detection technique uses Cerenkov light detectors. Due to a much deeper collection volume with respect to scintillators, they are usually more sensitive to showers with large zenith angles, allowing a much greater sky coverage. Horizontal showers, initiated by very high energy neutrinos, are also believed to be detectable. An example of experiment using such devices is the Pierre Auger Observatory [10], currently the largest operating experiment in the world. It consists of an array of 1600 water Cerenkov tanks distributed over an area of 3000 Km^2 in the high fields of the Andes in Argentina. The Pierre Auger collaboration was able to detect the highest energies ever observed in the universe, above 10^{19} eV.

Another category of experiments uses the fact that light charged particles in extensive air showers travel with relativistic speeds and emit Cerenkov radiation. Arrays of photomultipliers equipped with light collecting cones inside imaging telescopes with large collection areas can be used to measure the Cerenkov emission. Detectors based on Cerenkov light detection are mainly designed to measure photon initiated showers in the TeV region. Recent experiments include H.E.S.S. [11], MAGIC [12] and VERITAS [**?**].

Finally, at very high energies ($\sim$ E=10^{17} eV), shower particles excite nitrogen molecules in the atmosphere which results in the emission of fluorescence light. The instrumentation is rather similar to the one used for Cerenkov light detection. The Fly's Eye experiment [13] was operated during more than 10 years and consisted in two stations of 67 spherical mirrors. It was upgraded with its successor, the High Resolution Fly's Eye (HiRes) which took data up to 2006. The Pierre Auger Observatory also uses four fluorescence light sites (each comprise six telescopes) overlooking the 1600 surface detectors which makes it a hybrid detector. The detection of the same shower by the two complementary methods provides very important cross-checks in terms of the energy measurement. The KASKADE-Grande can also be operated

in hybrid mode. The Telescope Array (TA) [14] is located in Utah, USA, and consists of 576 scintillator stations and three fluorescence detector sites. Fluorescence measurements are difficult because they require that the atmospheric conditions are well known. Moreover, the detectors can only be operated during cloudless and moonless nights which significantly reduces the duty cycle of these detectors.

1.3 Energy spectra of cosmic rays

The Cosmic Rays that reach the atmosphere of the Earth include all stable charged particles and nuclei with lifetimes of order 10^6 years or longer. They belong to a *non-thermal* class particles which energy spectra follows a power law:

$$\frac{dN}{dE} \propto E^{-\gamma} \tag{1.1}$$

Where N is the number of particles and E the particle kinetic energy. A wide range of energies, ranging from 10^8 eV/nucleon to 10^{20} eV/nucleon have been observed. The spectrum observed at the top of the atmosphere, is constituted by *primary* cosmic rays (i.e. particles accelerated at astrophysical sources) and by *secondaries* cosmic rays (i.e. particles produced in interaction of the primaries with interstellar medium). Electrons, protons and helium, as well as carbon, oxygen, iron, and other nuclei synthesized in stars, are primaries. Nuclei such as lithium, beryllium, and boron (which are not abundant end-products of stellar nucleosynthesis) are secondaries. Antiprotons and positrons are also in large part secondary. Whether a small fraction of these particles may be primary is a open question of great interest.

Figure 1.2 shows the *all-particle* differential energy spectrum multiplied by $E^{2.6}$ in order to display the features of the steep spectrum that are otherwise difficult to discern: it is clearly visible that the spectral index is not the same for the whole energy range. The first change of the spectral index is observed between 10^{15} and 10^{16} eV, this region is known as the *knee* of the spectrum. The second change is around $10^{18.5}$ eV is called the *ankle* of the spectrum. The change in the spectral index could reflect the different acceleration processes and origin of the observed cosmic rays as will be discuss in the following section.

At low energies (E<10–20 GeV), the intensity of the incoming charged particles is modulated by the solar wind. As will be extensively discuss in section 1.4.2 there is

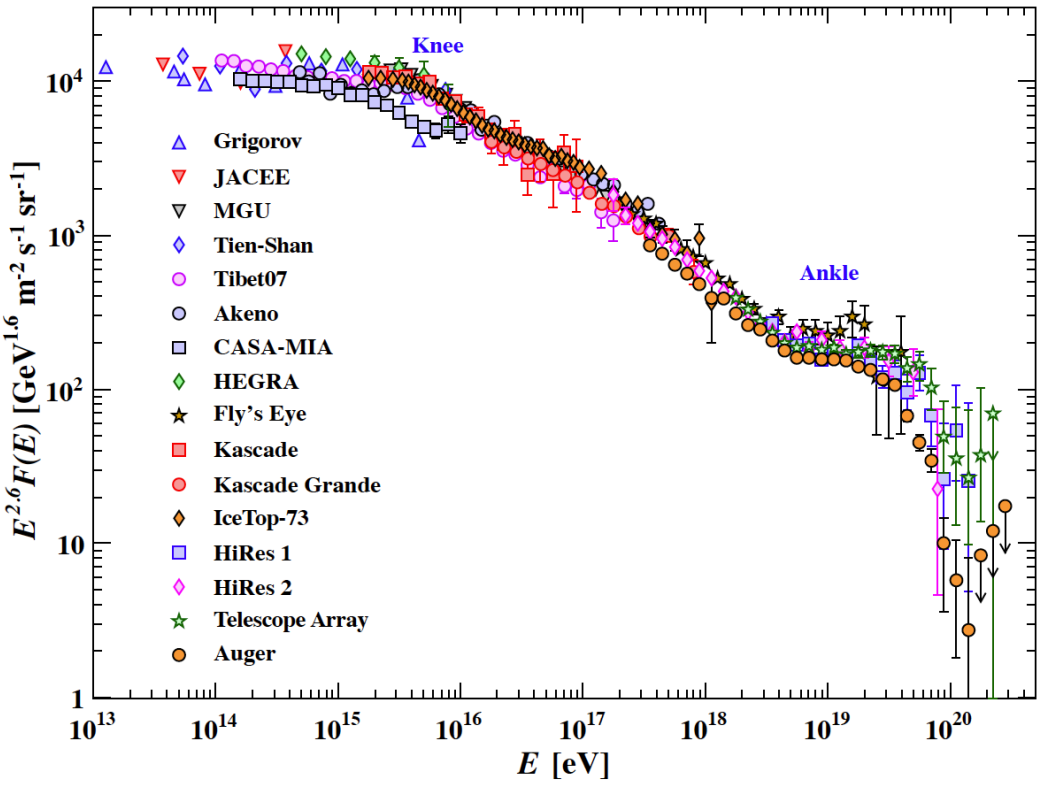

FIGURE 1.2: The all-particle spectrum as a function of E (energy-per-nucleus) from air shower measurements (from [15]).

a significant anticorrelation between solar activity and the intensity of the cosmic rays. In addition, the lower-energy cosmic rays are affected by the geomagnetic field, which they must penetrate in order to reach the top of the atmosphere. Thus the intensity of any component of the cosmic radiation in the GeV range depends both on the location and time (see section 1.4.1).

1.3.1 Origin and acceleration of Cosmic Rays

The sources and acceleration mechanisms of CRs are still an open problem. However, it is quite sure that Supernova remnants and pulsars are sources of cosmic rays. From the observation of radio spectra of these astrophysical object it is possible to know the value of the spectral index of cosmic rays at the moment of their injection in the interstellar medium. After their production, CRs are accelerated and ejected into the ISM. The Fermi mechanism [16] is able to explain how the shock wave produced by the explosion of a supernova is able to accelerate CRs up to energies of 10^{15} GeV. The mechanisms that are able to accelerate CRs at higher energies, should be different from the supernova shockwave and they are still a mystery.

Another fundamental question is if the CRs that we are able to observed, have a *galactic* or *extragalactic* origin.

The case of electrons is simple. The microwave background radiation permeates all space and therefore all relativistic electrons are subject to *Inverse Compton* losses. For example, taking a E=100 GeV electron, if we consider only the *Inverse Compton* energies losses, the source cannot be at distant more than 4.2 Mpc. They cannot come neither from local supercluster because its centre is about 20 Mpc away. Therefore it should be concluded that the electrons, at least, must have a galactic origin.

For protons and nuclei the situation is quite different since the loss of energy due to interaction with the interstellar medium it is almost negligible if compared with the one that we have for electrons. The trajectory of protons and nuclei is influenced by the Lorentz force due to the galactic magnetic field (B). The thickness of the Galactic disc is ∼300 pc and the radius of the halo about 10 Kpc.

For low values of rigidity ($R = p/Ze$) protons and nuclei have the gyroradius r ($r = R/Bc$) of the particle's orbit, less then the thickness of the Galactic disc. This means that these cosmic rays cannot escape from the galaxy and moreover that their origin should be *galactic*.

For protons it is possible to demonstrate [17], that for energies $< 10^{15}$ GeV they are contained into the galactic disk. For energies $\sim 10^{15}\,GeV$, the gyroradius r is quite similar to the thickness of the disc and for energies $> 10^{18}$ GeV they cannot be contained and it is impossible to confine them to the plane of the Galaxy. It is clear that they should be came straight from their sources if they are in the Galaxy.

The different sources and acceleration mechanism are reflected by the spectral index in the flux of all particles (see 1.2). Assuming the cosmic ray spectrum below 10^{18} eV is of galactic origin, the *knee* could reflect the fact that most of the cosmic accelerators in the galaxy have reached their maximum energy. Some types of expanding supernova remnants, for example, are estimated not to be able to accelerate protons above energies in the range of 10^{15} eV.

Concerning the ankle, one possibility is that it is the result of a higher energy population of particles that overtakes a lower energy population, for example an extragalactic flux begins to dominate over the galactic flux. Another possibility is

that the dip structure in the region of the ankle is due to $\gamma p \rightarrow e^+ + e^-$ energy losses of extragalactic protons on the 2.7 K cosmic microwave radiation (CMB) [18].

In the highest energy region E> 10^{19} eV, the flux is suppressed by the so called Greisen-Zatsepin-Kuzmin (GZK) mechanism [19]: CRs start to interact with Cosmic Microwave Background (CMB) photons through the Δ^+ resonance ($p+\gamma_{CMB} \rightarrow \Delta^+$ and their path length in the ISM steeply decreases. Cosmic rays are not expected to be observed above this limit without invoking exotic explanations, and the flux measured by ground experiments above 10^{19} eV shows a significant suppression as predicted by this model.

1.3.2 Cosmic Rays propagation

The CR propagation is generally described by a Fokker-Planck type equation [20] which includes source distribution, particle diffusion in the galactic magnetic field, energy losses, nuclear interactions, decays and acceleration processes. According to this equation, the density per momentum units p for the i^{th} specie (ψ_i), can be written as:

$$\begin{aligned}\frac{\partial \psi_i(\overrightarrow{r},p,t)}{\partial t} = q(\overrightarrow{r},p,t) + \overrightarrow{\nabla}\cdot(D_{xx}\overrightarrow{\nabla}\psi_i - \overrightarrow{V}\psi_i) + \frac{\partial}{\partial p}p^2 D_{pp}\frac{\partial}{\partial p}\frac{1}{p^2}\psi_i + \\ -\frac{\partial}{\partial p}[\dot{p}\psi_i - \frac{p}{3}(\overrightarrow{\nabla}\cdot\overrightarrow{V})\psi_i] - (\frac{1}{\tau_f}+\frac{1}{\tau_r})\psi_i\end{aligned} \tag{1.2}$$

The temporal, spatial and energetic evolution of the CR densities is ruled by several factors:

Source term, $q(\overrightarrow{r},p,t)$
The source term includes primary, spallation, and decay contributions. $q(\overrightarrow{r},p,t)$ represents any possible production mechanism for primary particles. The spatial distribution of CRs sources is assumed to be correlated with the density of known pulsars or SNRs. The energy injection spectrum of the source term is modeled as a power law spectrum $\frac{\partial}{\partial p}q \propto p^\gamma$

Diffusion in the galactic cosmic rays, D_{xx}, D_{pp}
The concept of CR diffusion explains why energetic charged particles have highly isotropic distributions and why they are well retained in the Galaxy. The terms D_{xx}, D_{pp} describe the diffusion of the particles in the turbulent magnetic field. The galactic magnetic field that tangles the trajectories of particles plays a crucial role

in this process.

The cosmic rays propagate through the Galaxy from their sources to the Earth, under the influence of the galactic magneti field B_{gauss}, which curves their trajectories. The curvature depends, in addition to the intensity of galactic magnetic field ($B_G \sim 6\mu G$ [21]), by the particle rigidity R, defined as the ratio between the particle momentum and its charge. Different particles with the same rigidity are equally affected by the magnetic fields.

The galactic magnetic field can be decomposed in a regular component, which follows the distribution of the arms of the Galaxy, and a turbulent component in the form of perturbations of the regular field. The resonant scattering of charged CRs with these random small fluctuations $\delta B << B$ leads to a diffusive motion.

Typical values of the diffusion coefficient found from a fit to CR data are $D_{xx} \sim (3 - -5) \times 10^{28}\,\mathrm{cm}^2 s^{-1}$ at energy $\sim$1 GeV/n.

In addition to the spatial diffusion, the interaction with the turbulent galactic fields induces a stochastic acceleration, also known as re-acceleration [22]. This process is modeled by a diffusion in momentum space with a coefficient $D_{pp} \propto |\overrightarrow{V}|^2 |D_{xx}$, where the Alfvén velocity $\overrightarrow{V}$ is the characteristic velocity of the fluctuation propagation in the magnetic field.

Convection with galactic wind, $\overrightarrow{\nabla} \cdot \overrightarrow{V} \psi_i$

CRs may not only diffuse in our Galaxy: the existence of galactic winds in many galaxies suggests that convective (or advective) transport may be important. Winds are common in galaxies and can be CRs driven. The effect of this galactic wind is to dilute the energy of the particles located in the disc in a larger volume, so that the adiabatic expansion results in a kind of energy loss (*adiabatic deceleration*), depending on the wind velocity $V = V(t, r)$. The topology, the speed and the evolution of the galactic winds are highly constrained by measurements of secondary to primary CR ratios, like the boron to carbon ratio (B/C), and of the unstable isotope ratios, like the $^{10}Be =^{9} Be$ ratio.

Nuclear processes, τ_f and τ_r

The terms τ_f and τ_r indicate respectively the timescale for loss by fragmentation and the timescale for radioactive decay. Unstable nuclei can decay into other nuclear products with a total lifetime $\Gamma = (\tau_f + \tau_r)$, thus decreasing their density by the factor $\Gamma \psi_i$ and increasing the product densities by a factor proportional to the decay probabilities. Spallation processes of CRs with the ISM also contribute to

the evolution of the density. Nuclear processes are responsible for the production of secondary species that are not accelerated in astrophysical sources.

Energy losses, $-\frac{\partial}{\partial p}(\dot{p}\psi_i)$
The terms $\frac{\partial}{\partial p}[\dot{p}\psi_i$ indicate the energy losses by the particles through various process that occurred during the propagation in the interstellar medium. Protons and nuclei mainly loose their energy due to the ionization process. Instead, as will be shown in the next chapter, the electrons and positrons loose their energy mainly for synchrotron and Inverse Compton processes.

In the case of the steady-state assumption $\frac{\partial\psi_i(\overrightarrow{r},p,t)}{\partial t} = 0$ the result to the equation 1.2 completely describes the Local Interstellar Spectrum (LIS) for each species before entering in the solar system. The equation can be solved both in the semi-analytical and numerical way, using dedicated package like GALPROP [23] or DRAGON [24].

1.3.3 Electrons and positrons propagation

In the case of electrons (e^-) and positrons (e^+), in the equation 1.2 all the terms related to nuclear process can be neglected. The $e^\pm$ propagation can be described by equation:

$$\frac{\partial\psi_{e^\pm}(\overrightarrow{r},p,t)}{\partial t} = q(\overrightarrow{r},p,t) + D_{xx}\cdot\overrightarrow{\nabla}^2\psi_{e^\pm} - \frac{\partial}{\partial p}(\dot{p}\psi_{e^\pm}) \tag{1.3}$$

It is possible to easily resolve this equation making some assumptions and obtaining, however, many of the most important results for the propagation of electrons in the galaxy. First of all, we consider a steady-state solution $\frac{\partial\psi_{e^\pm}(\overrightarrow{r},p,t)}{\partial t} = 0$. Taking into account an infinite, uniform distribution of sources, each injecting cosmic ray electrons with a spectrum $N(E) \propto E^{-\gamma}$ ($q(\overrightarrow{r},E,t) = KE^{-\gamma}$), the diffusion is not important and the equation 1.3 can be written as:

$$q(\overrightarrow{r},p,t) = \frac{d}{dp}(\dot{p}\psi_{e^\pm}(\overrightarrow{r},p,t)) \quad\rightarrow\quad \int_0^\infty q(\overrightarrow{r},p,t)\,\mathrm{d}p = \int_0^\infty \mathrm{d}[\dot{p}\psi_{e^\pm}(\overrightarrow{r},p,t)] \tag{1.4}$$

Assuming $\psi_{e^\pm}(\overrightarrow{r},p,t)\rightarrow 0$ for $p\rightarrow\infty$, equation 1.4 gives:

$$\psi_{e^\pm}(\overrightarrow{r},p,t) = \frac{Kp^{-(\gamma-1)}}{(\gamma-1)\cdot(-\frac{dE}{dt})} = \frac{Kp^{-(\gamma-1)}}{(\gamma-1)\cdot b(E)} \tag{1.5}$$

The various energy loss mechanisms $b(E) = -\frac{dE}{dt}$ (that affect the electrons from their sources to the Earth), distort the initial energy spectrum and thus potentially provide information about the life histories of the cosmic ray electrons. In order to know in which way the energy losses modulate the initial energy spectrum, we need to know the form of $b(E)$. The electrons interact with matter, magnetic fields and radiation trough the *Ionization*, *Bremmstrhalung*, *Synchrotron radiation* and *Inverse Compton*. However, the main sources of b(E) in the case of electrons are *Bremmstrhalung* and *Synchrotron radiation*.

Ionization losses

Generally the Ionization losses are of little importance for electrons. The energy loss due to the ionization process for electrons is described by the Bethe-Block formula:

$$-\frac{dE}{dx} = \frac{e^4 NZ}{8\pi\epsilon_0^2 m_e v^2}[ln\frac{\gamma^2 m_e v^2 E}{2I^2} - (\frac{2}{\gamma} - \frac{1}{\gamma^2}) \times ln2 + \frac{1}{\gamma^2} + \frac{1}{8}(1 - \frac{1}{\gamma})^2] \qquad (1.6)$$

Since it is a process $\propto 1/\gamma$, for protons and electrons of the same kinetic energy, the energy loss rate is greater in the case of protons. The energy loss per time unit is proportional to $ln\, E$:

$$-(\frac{dE}{dt})_{ionization} \propto ln\, E \qquad (1.7)$$

Bremmstrhalung

The *bremsstrahlung* radiation occurs when a charge particle enters in a nuclear field. The particle is accelerated or decelerated due to the Coulumb force and it emits electromagnetic radiation. The energy loss per unit time for *bremsstrahlung* process in the relativistic case, can be written:

$$-(\frac{dE}{dt})_{brem} = \frac{Z^2 z^4\, e^2\, E}{12\,\pi^3\,\epsilon_0^3\, M^2\, c^4 \hbar}\, ln(\frac{192}{Z^{1/3}}) \qquad (1.8)$$

Where Z is the charge of the target and z and M are respectively the charge and the mass of the incident particle. The process strongly depends by the mass of the incident particle ($\propto 1/M^2$) for this reason is more important for electrons than for protons. The energy loss per unit time is proportional to E: at low energies electrons and positrons primarily lose energy by ionization. While ionization loss rate rises logarithmically with energy, the bremsstrahlung losses rise nearly linearly with energy and dominate above a few tens of MeV.

Synchrotron

The *synchrotron emission* is the radiation of a high energy charged particle traveling

in a magnetic field. This same mechanism is responsible for the radio emission from the Galaxy, from supernova remnants and extragalactic radio sources. The energy loss for unit time can be written as:

$$-(\frac{dE}{dt})_{sync} = \frac{4}{3}\sigma_T c(\frac{E^2}{(mc^2)^2})U_{mag} \tag{1.9}$$

where σ_T is the Thomson cross-section and U_{mag} is the energy density of the magnetic field. The energy loss is $\propto E^2$: the *synchrotron emission* gives the main contribution to the energy loss for relativistic and ultra-relativistic electrons and positrons.

adiabatic losses

If the relativistic electrons are confined within a region of volume V, the pressure of the electrons causes the volume expansion and the electrons lose energy adiabatically through the work done in this expansion. This is an important loss process in the evolution of radio sources and supernova remnants. The energy lost by the electrons goes into the bulk kinetic energy of expansion of the emitting region. The energy loss rate in a case of a spherical expansion with radius R, can be written:

$$-\frac{dE}{dt}_{adiabatic} = (\frac{1}{R}\frac{dR}{dt})E \tag{1.10}$$

The condition for important adiabatic losses is that the time-scale of the expansion should be of the order of the time in which the particles have been in the emitting volume. If the particles have always been in the source during its expansion, adiabatic losses are always important.

Inverse Compton scattering

In the *Inverse Compton scattering* electrons collide with a photon that gains energy at the expense of electrons, contrary to what happens in the *Compton scattering*. The situation most often encountered in astrophysical conditions is the limit in which the energy of the photon in the centro of momentum frame of the collision is much less than the rest mass energy of the electron ($\gamma h\nu \ll m_e c^2$). The energy loss per unit time, is:

$$(\frac{dE}{dt})_{IC} = \frac{4}{3}\sigma_T c U_{rad}(\frac{E^2}{(mc^2)^2}) \tag{1.11}$$

1.9 and 1.11 have the same characteristic. The reason for this is that in both cases, the particle is being accelerated by the electric field which it sees. *Inverse Compton*

scattering of cosmic ray electrons in our Galaxy is important for the following reasons. First, there is an average energy density of optical photons due to the light of all the stars which amounts to $U_{rad} \sim 0.6\, eV\, cm^{-3}$. Second, there is the microwave background radiation which fills the whole Universo. Its energy density is about $0.25\, eV\, cm^{-3}$.
Comparing equations 1.9 and 1.11 and putting $B = 3{\times}10^{-6}\, G$ and $U_{rad} = 0.6\, eV\, cm^{-3}$:

$$\frac{(dE/dt)_{IC}}{(dE/dt)_{sync}} = \frac{U_{rad}}{U_{mag}} = 3 \tag{1.12}$$

Inverse Compton losses are bound to be important for cosmic ray electrons. Electrons outside the Galaxy would have very little energy loss due to synchrotron radiation, because we can set very low limits on the intergalactic magnetic field. However, the microwave background is omnipresent and therefore the electrons must lose all their energy in the scattering with photons of the microwave background.

summary of energy losses for cosmic electrons and positrons
Taking into account all the energy loss processes described above, the term $b(E)$ in the equation 1.5 can be written as:

$$b(E) = -(\frac{dE}{dt}) = A \cdot (ln\, E) + B \cdot E + C \cdot E^2 \tag{1.13}$$

where the first term ($\propto ln\, E$) is due to the ionization losses, the second one ($\propto E$) to the Bremsstrahlung and adiabatic losses and the third one ($\propto E^2$) is due to Synchrotron and Inverse Compton scattering losses.
From 1.5 follows that:

- if ionization losses dominate $\rightarrow$ $\psi_{e^{\pm}}(\overrightarrow{r}, p, t) \propto E^{-(\gamma-1)}$;
- if Bremsstrahlung or adiabatic losses dominate $\rightarrow$ $\psi_{e^{\pm}}(\overrightarrow{r}, p, t) \propto E^{-\gamma}$
- if Synchrotron or Inverse Compton losses dominate $\rightarrow$ $\psi_{e^{\pm}}(\overrightarrow{r}, p, t) \propto E^{-(\gamma+1)}$;

Figure 1.3 shows the values of the loss function 1.13 as a function of the energy of the electron for an intercluster medium (ICM) electron density of $n_e = 1.0 \times 10{-}3\,\mathrm{cm}^{-3}$ and a typical ICM magnetic field of $B = 1\,\mu$G [25]. From the figure is clear that the Inverse Compton losses are dominant for energies $> 0.1\, GeV$ while Coulomb losses dominate for sufficiently small energies ($E < 0.1\, GeV$) or for higher densities.

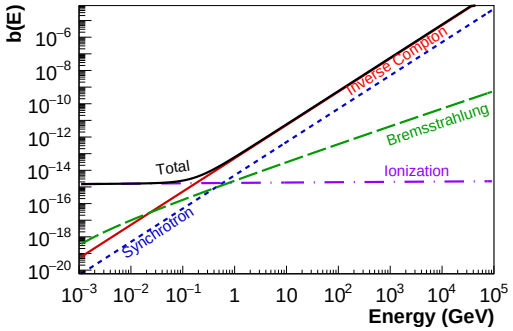

FIGURE 1.3: Values of the loss functions 1.13 as a function of the energy of the electron for an intercluster medium (ICM) electron density of $n_e = 1.0 \times 10{-}3\,\mathrm{cm}^{-3}$ and a typical ICM magnetic field of $B = 1\,\mu\mathrm{G}$ [25].

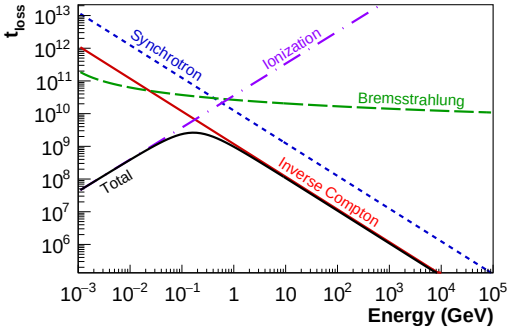

FIGURE 1.4: Instantaneous loss timescale ($t_{loss} = \frac{E}{b(E)}$) as a function of energy of the electron for an intercluster medium (ICM) electron density of $n_e = 1.0 \times 10{-}3\,\mathrm{cm}^{-3}$ and a typical ICM magnetic field of $B = 1\,\mu\mathrm{G}$ [25].

Bremsstrahlung losses are unlikely to be dominant unless the density is higher than the typical one in the bulk of the ICM. Similarly, synchrotron losses are unlikely to be dominant unless the magnetic field is much stronger than $1\,\mu$G. Figure 1.4 shows the time scale for particle losses $t_{loss} = \frac{E}{b(E)}$ calculated with the same condition of 1.4. The maximum loss time ($\sim 10^9$ years is reached for energies 0.1–0.5 GeV.

The solution of Equation 1.5 shows that the typical path length of $e^{\pm}$ with energies above ~ 1 GeV is smaller than the galactic halo. Therefore, $e^{\pm}$ CRs detected at the Earth above the GeV energies must have galactic origins. Moreover, differently from hadrons, the propagation volume they occupy drastically decreases with increasing energies. In the galactic environment, a 100 GeV $e^{\pm}$ has to originate from a distance $d < 1$ Kpc. At 10 TeV, the distance decreases to 200 pc. This is remarkable, as the measurement of high energy $e^{\pm}$ could potentially improve the knowledge of the galactic neighborhood with importants consequences on the phenomenological interpretation of the measurements of all the CR species.

1.4 The influence of local environment on CRs spectrum

Below ~20–30 GeV the CRs spectrum is strongly influenced by two local phenomena:the solar wind, which composes the heliosphere and extends up to the boundaries of the solar system, and the geomagnetic field, which composes the Earth's

magnetosphere. Both the effects produce a distortion of the interstellar spectra measured at Earth.
In the following will be discussed first the dynamics of charged particles in a dipole magnetic field as a zero-order approximation of the magnetic field of the Earth. Then will be discussed the influence of the solar activity.

1.4.1 Geomagnetic Cutoff

When the charged particles reach the Earth, they interact with the geomagnetic field due to the Lorentz force that curves their trajectory. Particles with low rigidities ($R = p/eZ$) are more deviated by the magnetic field and maybe they are not be able to reach the detector. For a given arrival direction and location, there will exist a minimum value of the particle rigidity (R_{cutoff}) for which galactic CRs are allowed to penetrate the magnetosphere and to be detected.
In the first approximation, the geomagnetic field can be represented as an offset and tilted dipole field with moment $M = 8.1 \cdot 10^{25}\,\mathrm{G\,cm^3}$, an inclination of 11^o to the axis of the earth rotation and a displacement of about 400 Km with respect to the Earth center. Due to this tilt and offset, the intensity of the geomagnetic field presents some distortion as shown in figure 1.5, the highs of which is in the South Atlantic. In this region, named *South Atlantic Anomaly (SAA)*, the field strength is the weakest and the the charged particles penetrate deeper in this region and the radiation becomes stronger. Moreover, the geomagnetic field is not constant in time as shown in figure 1.6: Geophysicists have noted that the strength of Earth's magnetic field has been decaying, about 5 percent globally over the past century. However, it is not changing in a uniform way; it grows growing stronger in some places and weaker in others.

In the dipole approximation, R_{cutoff} was analytically evaluated by Støermer [27, 28] that found the relation:

$$R_{cutoff} = \frac{M\,cos^4\lambda}{d^2[1 + (1 \pm cos^3\lambda cos\phi sin\xi]^2} \tag{1.14}$$

where M is the dipole moment. The arrival direction is defined by ξ and ϕ, respectively the polar angle from local zenith and the azimuthal angle counted clockwise form local magnetic East. The $\pm$ sign applies to negatively/positively charged particles. The arrival location is defined by the geomagnetic coordinates (d, λ), a

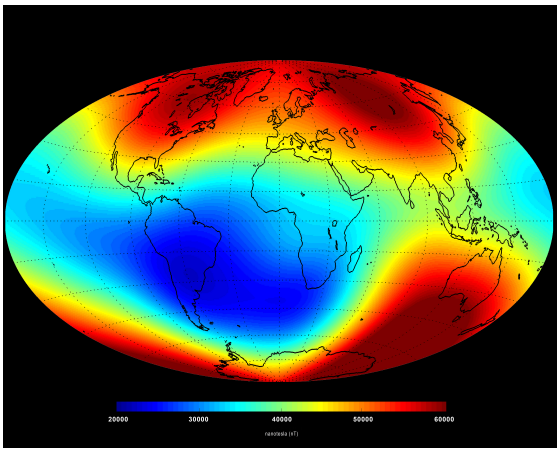

FIGURE 1.5: The average strength of Earth's magnetic field at the surface (measured in nanotesla) between January 1 and June 30, 2014, as measured by the Swarm constellation of satellites [26].

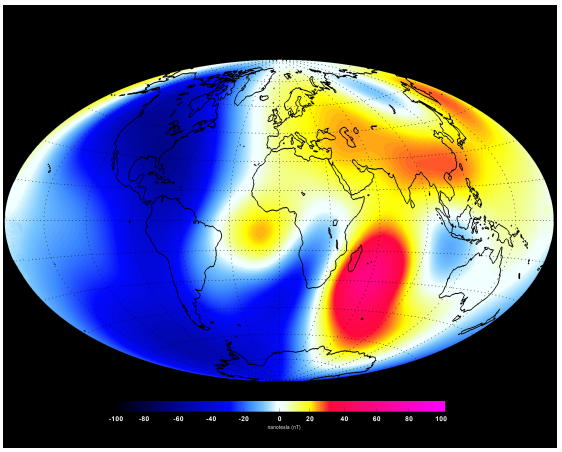

FIGURE 1.6: Changes in the Earth's magnetic field at the surface (measured in nanotesla) between January 1 and June 30, 2014, as measured by the Swarm constellation of satellites [26].

commonly used coordinate system relative to the dipole axis. d is the distance from the dipole center, usually expressed in Earth radii units ($d = r/R_{Earth}$), and λ is the latitude along the dipole. These quantities come from the simple dipole field description, where the components of the field are:

$$B_r = -\frac{M}{r^3} 2sin\lambda \qquad B_\lambda = \frac{M}{r^3} cos\lambda \tag{1.15}$$

and the field lines have the form $r \propto cos^2\lambda$. For vertically incident particles ($\xi = 0$) the azimuthal dependence of the cut-off simply vanishes, putting in evidence the cutoff behavior as a function of the geomagnetic latitude:

$$R_{cutoff}(\xi = 0) = \frac{M}{4\,d^2}\, cos^4\lambda \tag{1.16}$$

The cut-off is maximum at the geomagnetic equator, with a value of $\sim 15\,\mathrm{GV}$, and vanishes at the poles.

1.4.2 Cosmic rays in the heliosphere

When the cosmic rays reach the heliosphere, the low energy part of their energy spectrum is affected by the magnetic field carried by the solar wind. The solar wind consists of particles, ionized atoms from the solar corona, and fields, in particular magnetic fields. It is characterized by the different quantities, like particles velocity,

flux and concentration, temperature ecc... However the value of these quantities varies considerably during one period of solar activity.

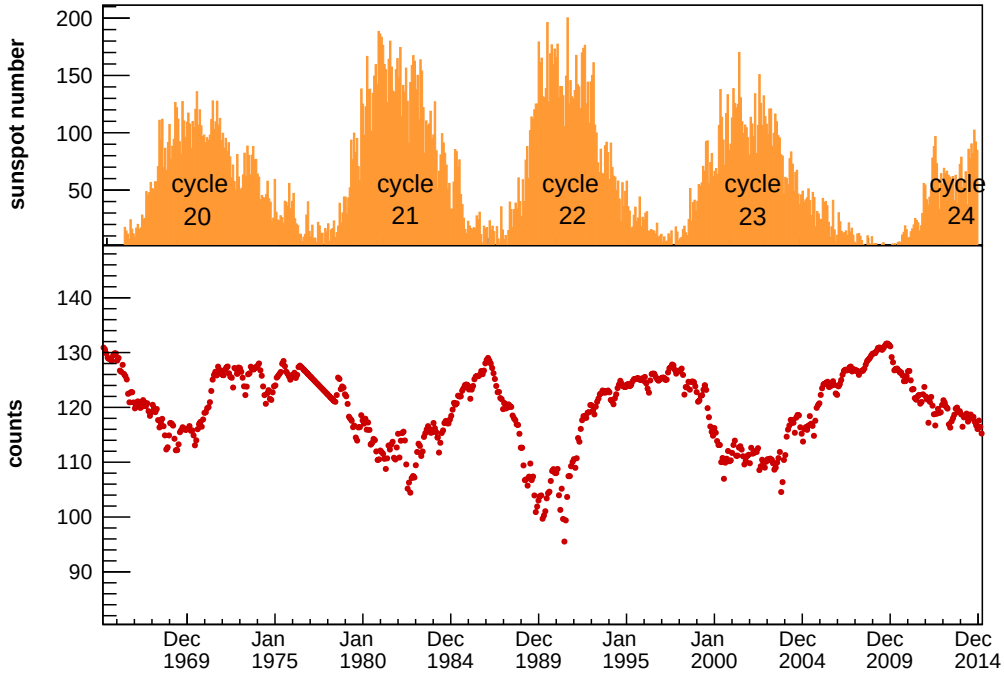

FIGURE 1.7: Sunspot number as a function of time (data from http://www.sidc.be/silso/datafiles) compared with neutron monitor counters as a function of time (data from http://neutronm.bartol.udel.edu/Welcome.html).

A good measure for the solar activity is the sunspot number, which has been observed almost continuously for the last centuries. During each *solar cycle*, which period is $\sim 11\,years$, the sunspot number rises from a low level to a large value and then comes down again. It is possible looking for some correlation (or rather anticorrelation) with the cosmic ray intensity and solar activity, by using a space-ground detector as the *neutron monitor*, a very stable counter which measures the total flux of neutrons or muons. Figure 1.7 shows the neutron counters compared with the solar activity as a function of time and is clear that the cosmic ray flux is very well correlated with solar activity. This phenomenon is known as *solar modulation*. As this effect involves all the cosmic rays that are detected at Earth (or in near space), it must be taken into account for interpretation of the measured spectra.

1.4.3 Force field approximation

An approximate description of the cosmic rays solar modulation, can be given considering a spherically symmetric configuration in which the solar wind carries magnetic irregularities radially with speed $V(r)$ [29]. This magnetic irregularities are assumed to act as "magnetic scattering centers" for the cosmic rays. In this situation the motion of the CRs can be described by the formula:

$$\begin{aligned} \frac{1}{r^2}\frac{\partial}{\partial r}(r^2 S) &= -\frac{V}{3}\frac{\partial^2}{\partial r \partial T}(\alpha T U) \\ s &= VU - \kappa\frac{\partial U}{\partial r} - \frac{V}{3}\frac{\partial}{\partial T}(\alpha T U) \end{aligned} \tag{1.17}$$

Where $U(r,T)$ is the differential density and $S(r,T)$ the radial current density of cosmic rays particles in the kinetic energy range $(T, T+dT)$; r is the radial distance from the Sun; κ is the diffusion coefficient and $\alpha = \frac{E+m}{E}$ where m and E are respectively the mass and the total energy of the cosmic ray particles.

In the *Force field approximation* it is possible to obtain a general solution that can be applied directly to the observation with satisfactory results. In this approximation, the term S is negligible, the diffusion coefficient κ can be written as a separable function of r and the rigidity R of the particle as $k = \beta\kappa_1(r,t)\kappa_2(R)$ with k_2 independent from time t [30]. In this case, the local cosmic-ray flux Φ can be written as a function of the interstellar cosmic-ray flux Φ_{IS} as follow:

$$J(E) = \frac{E^2 - m^2}{(E + |z|\phi)^2 - m^2} \cdot J_{IS}(E + |z|\phi) \tag{1.18}$$

where z is the particle charge and ϕ is a single parameter describing the solar modulation. It has the dimension of a rigidity and is of the order of 500 MV but it changes with time according to the solar cycle.

charge dependence of solar modulation

It can be expected that solar modulation depends on the charge sign of the particle, affecting positrons and electrons differently. The projection of the solar magnetic dipole on the solar rotation axis (A) can be either positive or negative. At each sunspot maximum, the dipole reverses direction, leading to alternating magnetic polarity in successive solar cycles as shown in figure 1.8. The Parker field [31] has opposite magnetic polarity above and below the helioequator, but the spiral field

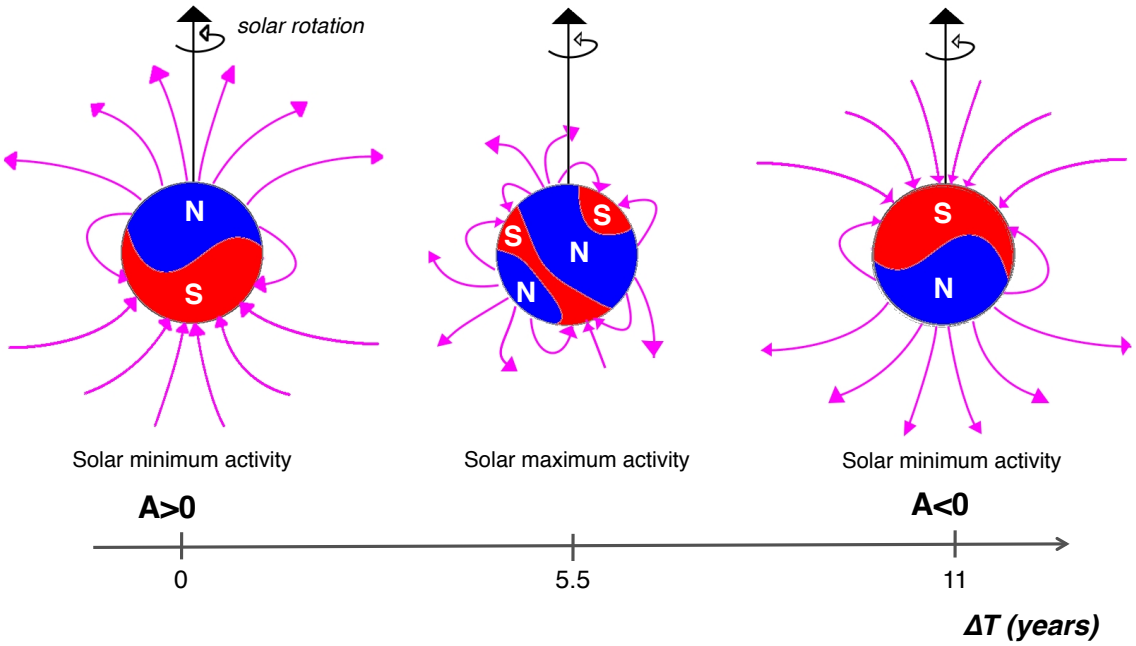

FIGURE 1.8: Configuration of the coronal solar magnetic lines (magenta lines) during an entire solar cycle of 11 years starting from a minimum of solar activity with positive polarity (A>0) and reaching the next solar minimum with negative polarity (A>0).

lines themselves are mirror images of each other. This antisymmetry produces drift velocity fields that (for positive particles) converge on the heliospheric equator in the A>0 state or diverge from it in the A<0 state. Negatively charged particles behave in the opposite manner, and the drift patterns interchange when the solar polarity reverses.

Moreover this effect is maximum during the minimum solar activity when the solar magnetic field is regular. During the maximum of the solar activity because of the irregularity of the solar magnetic lines, the diffusion processes dominate over the magnetic drift and the effect of the solar modulation is the same both for negative and positive charges.

1.5 The importance of cosmic electrons and positrons

The electrons and positrons are a rare component of CRs since they constitute respectively only a $\sim 1\%$ and $\sim 0.1\%$ of cosmic radiation. However, a big effort from

the sperimental point of view has been performed in order to detect this small component. The correct detection of electrons and positron covers a great importance in the astrophysics field since their energy losses through the interaction with ISM are different from the hadronic one. Electrons and positrons give complementary information about the origin and propagation of CRs respect to the hadronic component. Due to the strong energy losses, the electrons with energy above GeV that reach the Earth are galactic, with the source inside $\sim$ Kpc.

The electrons observed at the atmosphere are mostly primaries ($\sim$ 90%) and they are produced in the SNR (confirmed also by the observation of synchrotron X-ray emission). A small component ($\sim$ 90%) is constituted by secondary electrons produced by the interaction of primary CRs with the ISM.
The same argument cannot be applied for positrons that are mainly secondaries produced by the interaction of hadrons with ISM.

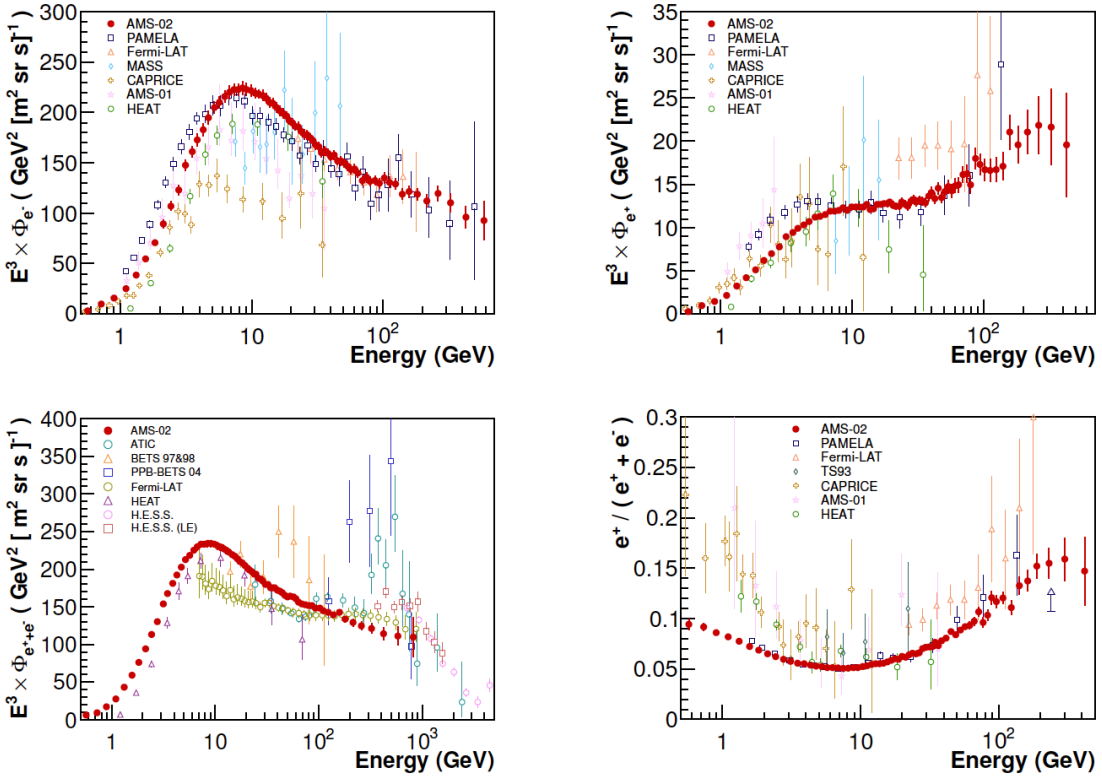

FIGURE 1.9: Experimental measurements of the e^- flux (Top Left), of the e^+ flux (Top Right), of the $(e^+ + e^-)$ flux (Bottom Left) and of the positron fraction, $e^+/(e^+ + e^-)$ (Bottom Right). Cosmic $e^\pm$ have been measured in the last 20 years by balloon [1, 32–39], space [2, 3, 40–43] and ground [44, 45]experiments. The latest measurements provided by the AMS experiment [5, 46, 47] increased the accuracy of the data and reached energy ranges never explored so far. The direct comparison of different experimental results below 30 GeV has to further take into account of solar modulation effects due to the different solar activity in the data taking periods.

The recent results of $e^{\pm}$ have sparked a big interested since they cannot be explained by the standard model propagation of CRs. Figure 1.9 shows all the latest measurements of cosmic $e^{\pm}$: electrons flux (Φ_{e^-}), positrons flux (Φ_{e^+}), all electrons flux ($\Phi_{e^++e^-}$) and positrons fraction ($\frac{\Phi_{e^+}}{\Phi_{e^++e^-}}$). Until 2011, the most precise results have been released by the H.E.S.S. ground telescopes, by the ATIC balloon experiment and by the PAMELA and Fermi-LAT satellite experiments. AMS operating on board of the ISS has provided $e^{\pm}$ data with unprecedented accuracy in the energy range [0.5 - 1000.0] GeV, with a huge impact on the understanding of the physics of the CRs $e^{\pm}$ component.

For energies below 20 GeV, the measurements from various experiments are not in agreement. This is due to the solar modulation since the data have been taken in different periods. Above 20–30 GeV the effects of solar modulation are insignificant.

The data shows that Φ_{e^-} and Φ_{e^+} have different spectral index. This indicates that electrons and positrons have different origin. Above $\sim$ 20 GeV and up to 200 GeV the electron flux decreases more rapidly with energy than the positron flux, that is, the electron flux is softer than the positron flux. This is not consistent with only the secondary production of positrons.

This feature is confirmed by the positrons fraction. Between 0.5–8 GeV the data are consistent with the secondary production predicted by the standard model but for energies $>$ 8 GeV the positron fraction shows an unexpected increase. From the separate fluxes measurement is clear that the excess in the positrons fraction is due to an excess of positrons and not to a decrease of electrons.

The measurement of the all electrons completes the $e^{\pm}$ measurements. The $\Phi_{e^++e^-}$ measured with higher accuracy than the separate fluxes, has been measured by AMS from 0.5 GeV to 1 TeV. The AMS $\Phi_{e^++e^-}$ is softer than previous measurements, and does not confirm the feature in the spectrum first observed above 300 GeV by the PPB-BETS and by the ATIC experiments **??**. The AMS $\Phi_{e^++e^-}$ measurement is in agreement at high energies with the data provided by the H.E.S.S. ground based experiment and by the Fermi-LAT satellite experiment within the systematics introduced by each detector energy scale uncertainties.

In order to explain the observed excess of positrons at high energies, should be taken into account an additional unaccounted primary source of e^+. The observed data, can be described by a minimal model in which Φ_{e-} and Φ_{e+} are parametrized as the sum of its individual diffuse power law spectrum ($A_{e^\pm}E^{-\gamma_{e^\pm}}$) and a common source

term ($C_{CS}E^{-\gamma_{CS}}e^{-E/E_{cutoff}}$) with an exponential cutoff parameter, E_{cutoff} [4, 5]:

$$\begin{aligned}\Phi_{e^-} &= A_{e^-}E^{-\gamma_{e^-}} + C_{CS}E^{-\gamma_{CS}}e^{-E/E_{cutoff}} \\ \Phi_{e^+} &= A_{e^+}E^{-\gamma_{e^+}} + C_{CS}E^{-\gamma_{CS}}e^{-E/E_{cutoff}}\end{aligned} \tag{1.19}$$

Many interesting interpretations have been formulated about the common source of electrons and positrons [48–51]. Two possible scenario have been taken into account both show in figures 1.10 and 1.11. In the first, the excess of positrons comes from pulsars. In this case, after a flattening out with energy, the positron fraction will begin to slowly decrease and a dipole anisotropy should be observed. In the second, the shape of the positron fraction is due to dark matter collisions. In this case, after the flattening out, the fraction will decrease rapidly with energy due to the finite and specific mass of the dark matter particle, and no dipole anisotropy will be observed. The extension of positron fraction up to TeV region, will help to discern between pulsar and dark matter models.

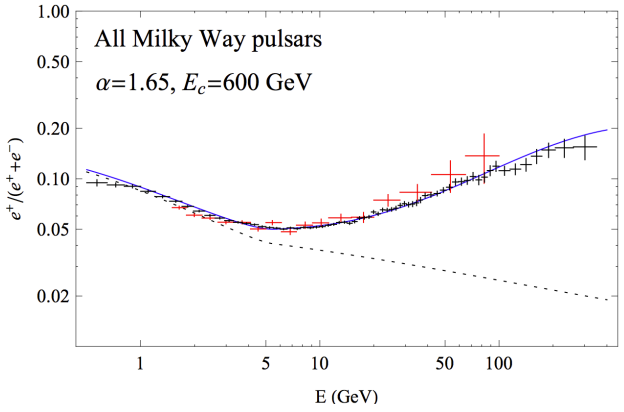

FIGURE 1.10: The predicted cosmic ray positrons fraction (blue line) from the sum of all pulsars throughout the Milky Way, for an injected spectrum of $dN_{e^\pm}/dE_{e^\pm} \propto E_{e^\pm}^{-1.55}exp(-E_{e^\pm}/600\,GeV)$[48]. The dashed line represent the result expected by the standard model of CRs propagation. The black points are the data from AMS-02 [4] and red points from PAMELA [2].

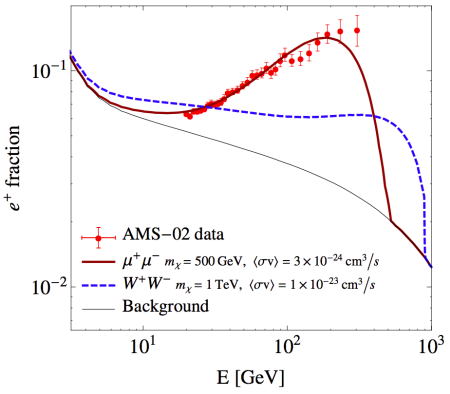

FIGURE 1.11: Comparison of the positron fraction measured by AMS-02 [4] to two particular dark matter scenarios. [49]

1.5.1 The Importance of cosmic electrons and positron at low energies

The spectrum of primary CRs electrons and positrons that reaches the Earth, is strongly modulated by the solar activity in the low energy part as explained in section Understanding the origin and propagation of cosmic rays requires knowledge of the cosmic-ray energy spectra in the interstellar medium, i.e. uninfluenced by the Sun's magnetic field. Solar modulation has a relevant effect on the cosmic-ray spectra at these energies that needs to be disentangled to allow to a comprehensive picture to emerge.

If the high energies part of electrons and positrons spectrum (E—100 GeV) seems to be dominated by local sources, the low energies part can be influenced by the different mechanisms of energies losses. Recent observations of the radio emission due to the synchrotron radiation [52], shows that the electrons spectrum at low energies can be described by a power law with an energy break around 3.87 GeV. The Synchrotron radiation probes interstellar electrons from 0.5 to 20 GeV and hence can be used in conjunction with direct measurements to construct the full spectrum from GeV to TeV. At low energies this allow an independent estimate of solar modulation for testing heliospheric propagation models. In contrast such a probe of the low-energy interstellar spectrum is not available for CR nuclei.
The observed break might simply reflect the fact that at lower energies the scattering on thermal ions and electrons ($b_{loss} \propto E$) becomes more important than inverse Compton losses ($b_{loss} \propto E^2$).

Chapter 2

The Alpha Magnetic Spectrometer

The Alpha Magnetic Spectrometer (AMS) is a large acceptance ($0.45\,\mathrm{m}^2\,\mathrm{sr}$) cosmic ray detector which has been installed on the International Space Station (ISS) in May 2011 during the STS-134 NASA Endeavour Space Shuttle mission, where it will collect cosmic rays until the end of the ISS mission, currently set to 2024. AMS-02 is an improved version of the AMS-01 magnetic spectrometer, which flew on the Shuttle Discovery [53] (STS-91 NASA mission) in June 1998. AMS has been designed and built taking advantages from the experience of the high energy particle physics experiments.

In this chapter, the various AMS components and the data acquisition on board of ISS will be presented.

2.1 AMS-02 detector

Figure 2.1 show a schematic view of AMS: the core of the instrument is a spectrometer, composed of a permanent magnet, which produces a magnetic field with an intensity of 0.14 T, and of 9 layers of double-sided micro-strip silicon sensors. The task of the spectrometer is the reconstruction of the trajectory and the measurement of the rigidity ($R = P/eZ$, momentum/charge ratio).
Above and below the spectrometer two planes of time of flight counters (ToF) provide the main trigger of AMS-02 and distinguish between up-going and down-going particles. This information combined with the trajectory curvature given by the spectrometer, is used to reconstruct the sign of the charge. A Transition Radiation

Detector (TRD) is located at the top of the instrument. The detector is completed with a Ring Imaging Cherenkov detector (RICH) and an electromagnetic calorimeter (ECAL).The central part of AMS-02 is surrounded by an anti-coincidence system (ACC) that provides the veto signal in the trigger for the high inclined particles.

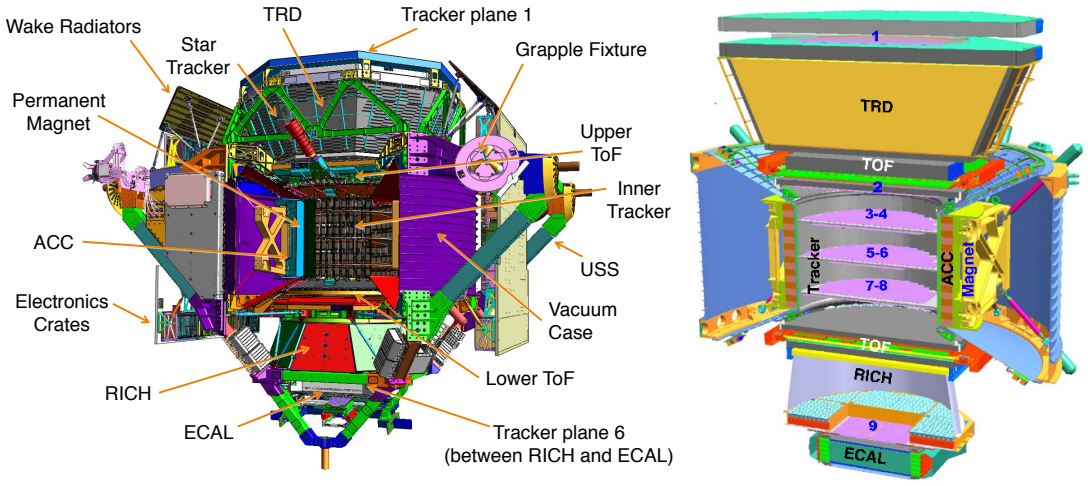

FIGURE 2.1: Two schematic views of AMS. The various detectors are labelled.

The main goal of the AMS experiment is to search for *antimatter of primordial origin* looking for the presence of anti-nuclei in the cosmic rays. Experimental evidences indicate so far that our galaxy is made of matter. However, there are more than hundred million galaxies in the Universe and the Big Bang theory of the origin of the universe requires equal amounts of matter and antimatter. Whether or not there is significant antimatter is still a mystery and one of the fundamental questions on the origin and nature of the universe. The detection of even a single anti-nucleus in the cosmic radiation, as a nucleus of $\overline{\text{He}}$, can be a direct proof of the existence of antimatter domains, since the probability of a spallation production of $\overline{\text{He}}$ is very low [54].

Another interesting discover potential for AMS concerns the *indirect dark matter detection*. The visible matter in the universe, such as stars, adds up to less than 5% of the total mass that is known to exist from many other observations. The other 95% of matter is dark, either dark matter, which is estimated at ∼27% of the energy balance of the universe; the remaining part is made up by dark energy. The exact nature of both is still unknown. The dark matter particles could be annihilating with each other and giving off an excess of standard charged particles that can be detected by AMS-02. The unexpected rising in the positrons fraction observed by PAMELA [2], was already confirmed with a very high accuracy by AMS [5]. The

observed positron excess may imply a heavy Dark Matter WIMP particle or a new mechanism of acceleration in the pulsars. Through the measurement antiproton to proton ratio and positron fraction to high energies, AMS has the potential to shed a light on the origin of these observed features, either from exotic sources such as dark matter particles or other astrophysical sources such as pulsars.

The high statistics measurements of AMS-02 of *all the charged species of the cosmic rays*, including chemical species up to Iron and isotopes up to Carbon, will largely improve our knowledge of the Interstellar medium in which cosmic rays propagate and will help to solve several astrophysics fundamental questions. The measurement of the nuclear and isotopic composition of cosmic rays can be used to validate or discard models for particle propagation in the interstellar medium. The accurate determination of the Boron to Carbon ratio over a wider range of energies will be crucial to determine propagation parameters like the thickness of the galactic halo or the galactic wind velocity [55].

AMS is able to perform a precise measurements of low energy CR fluxes (few hundred MV to tens of GV) covering a whole solar cycle (i.e. 11 years). This can be used to study the *effect of solar modulation* in great detail. The understanding of the origin and propagation of cosmic rays requires knowledge of the cosmic-ray energy spectra in the interstellar medium, i.e. uninfluenced by the Sun's magnetic field. The measurements of low energy CR fluxes during an entire solar cycle will help in the understanding of solar physics and in the propagation of CRs in the Heliosphere environment

Since AMS was scheduled to travel with the shuttle and operate in space, the requirements for its building were extremely challenging. Several constraints have been imposed by the transport on the Space Shuttle, by the transfer and the permanence on the ISS, as the strict weight limit of 7 tons, the very low power consumption ($\leqslant$2 kW) and the limited data rate (less then 20 Mbits per second). Each sub-system and electronic component has been produced in prototypes (engineering, qualification and flight models) tested in order to provide the expected physic performance and the mandatory Space safety [56]. AMS-02 is survived to accelerations up to $9\,g$ and vibrations up to $150\,dB$ during shuttle launch, and daily it withstands temperature cyclic variations between -80° C and 50° C in vacuum.

2.1.1 The Permanent Magnet

The permanent magnet of the AMS-01 precursor flight has been reutilized in the AMS-02 construction. A picture of the magnet can be appreciated in 2.2. It is composed by 64 sectors arranged in a cylindrical shape with inner radius of 115 cm, outer radius of 129.9 cm and a height of 80 cm. Each sector is assembled from 100 high grade Nd–Fe–B blocks glued together with epoxy. This arrangement results in a dipole magnetic field of 0.15 T in the magnet center, with a negligible dipole moment outside the magnet case ($\sim 10^{-2}$ T). Due to the almost uniform magnetic field inside

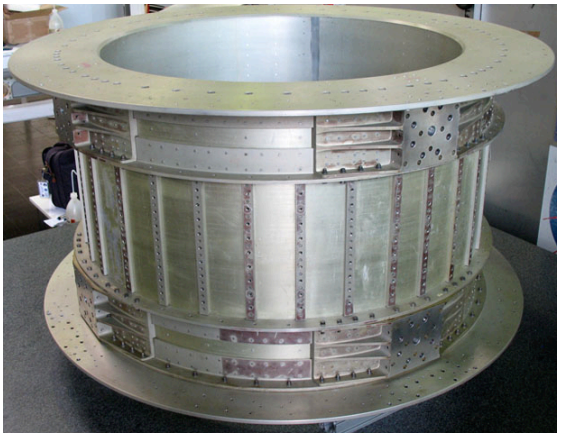

FIGURE 2.2: AMS permanent magnet, already employed for AMS-01 experiment on board of Space Shuttle Discovery [53].

the magnetic bore, the permanent magnet also defines the natural reference frame for AMS with its origin at the center of the magnet, as can be observed in Fig. 2.3. The Z axis runs along the cylinder's axis of symmetry, with positive values in the direction of the top of the instrument. The X axis is aligned to the magnetic field lines while the Y coordinate describes the bending direction. With this choice of reference, the bent trajectories of all charged particles traversing the magnet are contained in the Y–Z plane.

2.1.2 The Silicon Tracker

The Silicon Tracker is made of 2264 double-sided micro-strip silicon sensors distributed over 9 layers [57, 58] disposed on 6 planes three inside and three outside the magnet, for a total active area of $\sim 6.4\,\mathrm{m}^2$. As show in Figure 2.4, 3 of the 9 layers are located outside the magnetic field of the permanent magnet: one is located on top of the TRD, another one above the magnet, and the last one between

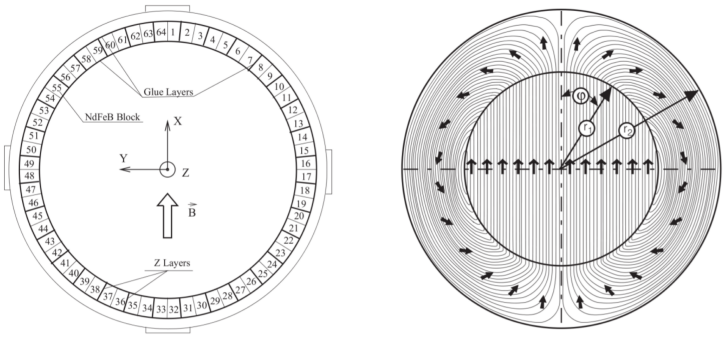

FIGURE 2.3: Left: AMS magnet configuration. 64 Nd-Fe-B blocks are distributed in the toroidal structure to provide an uniform dipole field in the magnet inner volume. Superimposed in the picture is the AMS coordinate reference frame. Right: Magnetization vector. Its flux is confined in the magnet volume, providing a negligible leaking field.

the RICH and the ECAL. The others 6 layers constitute the inner Tracker which is contained in the permanent magnet field volume.

Each planes located inside (outside) have a composite structure with two 220

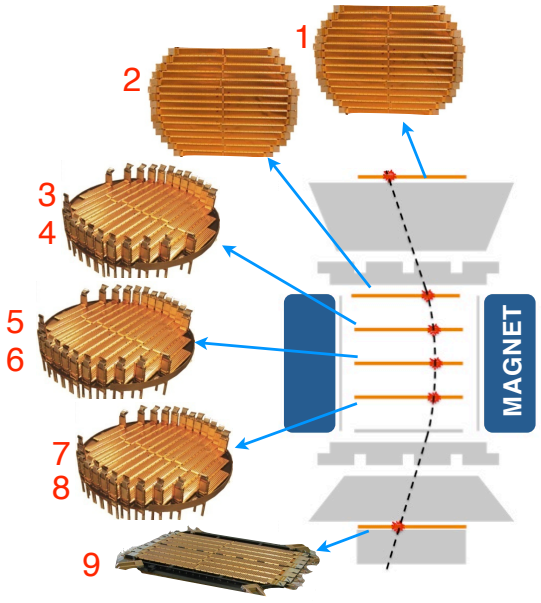

FIGURE 2.4: Disposition of the 9 Silicon Tracker layers: 3 are located outside the magnetic field. The others 6 layers constitute the inner Tracker which is contained in the permanent magnet field volume.

(700) μm thick layers of Carbon fiber surrounding a 12 (40) mm thick, low density Aluminum honeycomb interior of density $\rho = 16.02\ (32.0)\,\mathrm{Kg/m^3}$. The diameter of the interior (exterior) planes is 1.0 (1.4) m (upper photos of figure 2.5). A Carbon fiber cylindrical shell, supporting planes 3 to 5 located inside the magnet, and two Carbon fiber flanges, supporting the exterior planes 1,2 and 6 provide an high precision Silicon sensor positioning and the mandatory structure resistance for vibrations

due to the Shuttle launch (lower photo of figure 2.5). Layers 1-8 have a diameter

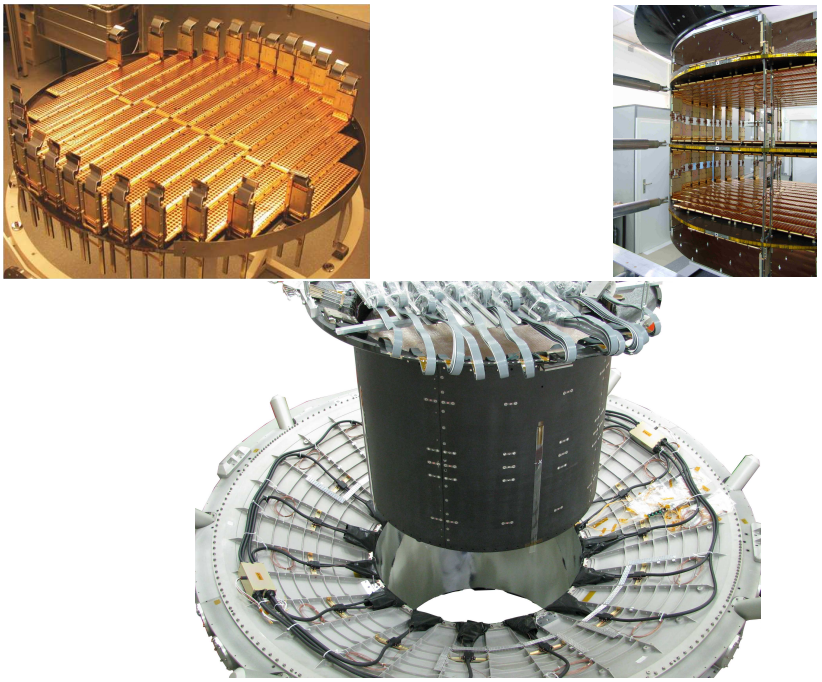

FIGURE 2.5: Some of the steps of the Tracker integration. Top left: an assembled layer. Top right: the assembling of the inner Tracker layers, note the 6 layers arranged on 3 supporting planes. Bottom: the pre-integration of the Silicon Tracker in the AMS vacuum case

of $\sim 1\,\mathrm{m}$ and contains approximately 24 ladders. Layer 9 is the smallest one and is constituted only by 16 ladders. Each ladder is composed by a variable number of double–sided silicon sensors (from 7 to 15) grouped along the x direction and coupled to a read out chain characterized by a low power consumption ($\sim 0.7\,\mathrm{mW}$ per channel), a low noise and a large dynamic range. The basic Tracker element, the double-sided Silicon sensor, has dimensions of $\sim 72.045 \times 41.360 \times 0.300\,\mathrm{mm}^3$. Biasing of n-type high resistivity $300\,\mu\mathrm{m}$ thick Si sensors is made with a dynamic resistive coupling, as punch-through and surface-through techniques. On the two surfaces p^+ strips with an implantation (readout) pitch of 27.5 (110) μm and n^+ strips, along the orthogonal direction, with implantation (readout) pitch of 104 (208) μm are placed. The finer pitch p-side strips is used to measure the bending, or y, coordinate while the orthogonal n-side strips measure x. When a ionizing particle crosses a silicon detector electron/hole pairs ($\sim 10^4$) are produced. Charges are rapidly drifted ($\tau \sim 10\,\mathrm{ns}$) by the sensor electric field, generated by the inverse bias regime, toward the segmented electrode strips. The obtained signal is proportional to the energy deposit and identifies the coordinate of the traversing particle. The

AMS tracker is able to detect the crossing points of particles with high accuracy ($\sim 10\,\mu$m in the bending direction and $\sim 30\,\mu$m along the non-bending one). From the crossing points it is possible to reconstruct the trajectory of the particle and the curvature of the trajectory provides the measurement of the particle Rigidity. It has a Maximum Detectable Rigidity, MDR, of $\sim$2 TeV for single charged particles as presented in Figure 2.6 reporting the rigidity resolution for proton particles estimated with a Monte Carlo simulation of the full detector and validated with beam test (red point in the figure) before launch. The accuracy of the rigidity measurement crucial to measure the momentum of all the non-electromagnetic particles as protons and nuclei, up to the TeV. Combining the information about the direction

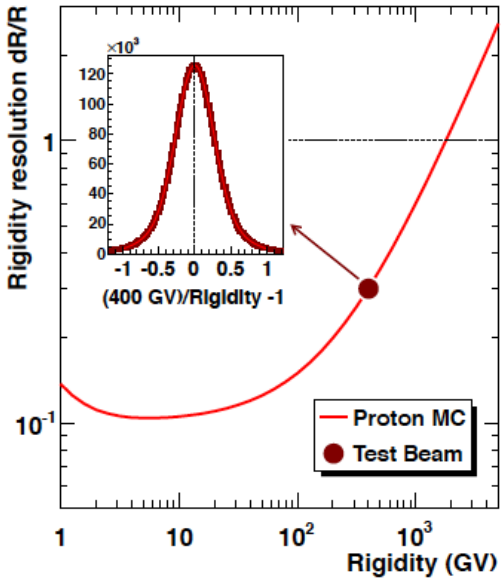

FIGURE 2.6: Rigidity resolution as estimated by Monte Carlo protons. The MDR is $\sim$2 TeV. The result from 450 GeV Test Beam protons is superimposed (full red circle) validating the simulation.

of the particle given by the ToF (down-going or up-going particle) with the sign of the rigidity is possible to reconstruct the sign of the charge. The Tracker system is completed by two sub-system: the Tracker Thermal Control System (TTCS), a two phases (liquid, gas) CO_2 heat exchanging system that chills the Tracker electronics minimizing the heat conduction toward the cryogenic magnet; and the Tracker laser Alignment System (TAS) providing optically generated signals in the 8 layers that mimic straight (infinite rigidity) tracks allowing the tracing of changes of the tracker geometry with a position accuracy of better than 5 μm. The Silicon Tracker performances in terms of calibration stability, spatial resolution and charge discrimination have been studied with several beam using electron, photon, protons and ions beam

lines. The measured spatial resolution of 10.7 (6.5) μm for protons (Helium) for the bending coordinate gives a Maximum Detectable Rigidity (MDR) of few TV.

2.1.3 Time Of Flight (ToF)

The AMS-02 ToF measures the particle velocity ($\beta = v/c$), flight direction and charge, and it provides the main trigger to the whole experiment (see section 2.1.9). It is composed by 4 planes of scintillation counters 2 above and 2 below the magnet (figures 2.1 and 2.7). The four planes contain, beginning from top, 8, 8, 10 and

FIGURE 2.7: The completed upper and lower ToF before the final shielding. The scintillator paddles, the bent light guides and the PMT are exposed.

8 scintillator paddles. The upper ToF and the lower ToF planes are alternatively positioned along the x and y coordinates providing a granularity of $12\times12\,\mathrm{cm}^2$ cells. The ToF single counter consists of 1 cm thick polyvinyltoluene scintillator of trapezoidal ($18.5–26.9\times117–134\,\mathrm{cm}^2$) or rectangular ($12\times117–134\,\mathrm{cm}^2$) shape, at both ends coupled, via plexiglass light guides, to 4 (rectangular) or 6 (trapezoidal) photo-multipliers (PMTs). A particular class of PMTs, the fine mesh, with a compact dynodes structure and high voltage ($\sim$1600 V) has been selected in order to reduce the dependence of the photo-induced multiplication by the stray magnetic field (of about $\sim 2\,\mathrm{kG}$). Tilted and bent light guides have been used to optimized the angle between PMT along the y-axis and the magnetic field (figure 2.5) [**?**]. The particle velocity $\beta = \frac{\Delta l}{c\Delta t}$ is measured using the time of flight Δt between Upper-Tof and Lower-Tof and the trajectory length Δs. The measured timing resolution on the time-of-flight is $\sim$160 ps for protons and $\sim$100 ps for particles with Z$\leqslant$2. The resulting resolution on velocity β is $\sigma/\beta \sim 3\%$ for protons and $\sigma/\beta \sim 1\%$ for ions.

The energy deposition in a single ToF counter gives also an evaluation of the particle charge exploiting the relation between the energy loss by ionization ($\propto Z^2$) and the produced scintillation light.

2.1.4 Anti-Coincidence Counter (ACC)

The highest analyzing power is reached for particles traversing the detector from top to bottom, with redundant measurement of the particle properties along the trajectory. For this reason is important identify and reject the particles entering the detector sideways. Such particles don't contribute to valuable information and can cause spurious triggers by interacting with the detector material. This is illustrated in Figure 2.8 where the type of events accepted and rejected based on the ACC information are shown. The ACC is made by 16 paddles arranged on a cylinder

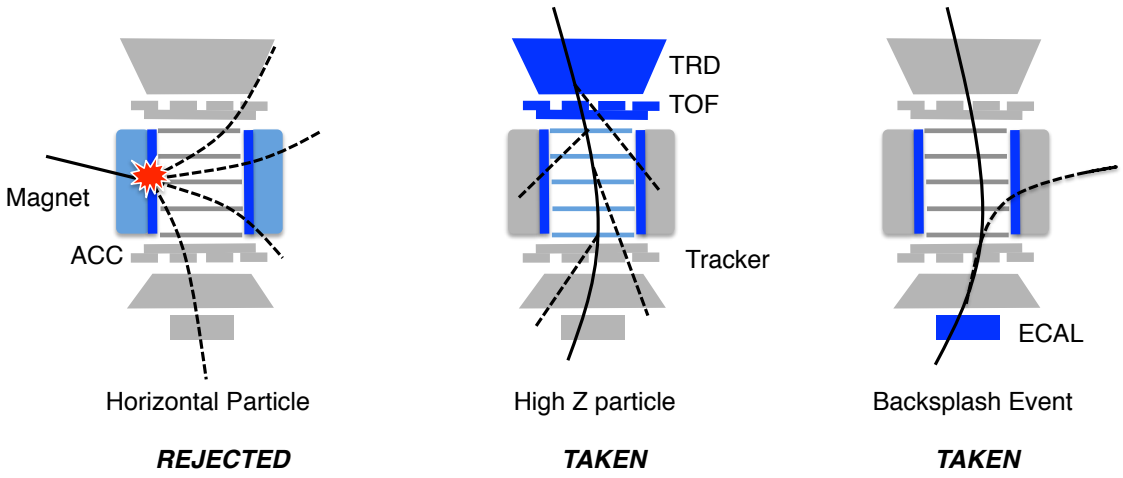

FIGURE 2.8: Some cases of how is used the ACC in the trigger of the event. *Left*: A particle entering the detector sideways may give a signal on ACC and not in ToF. This kind of events are rejected. *Center*: an incoming ion (high-Z particles): when an ion traverse matter it is accompanied by electron production, the so called δ–rays. These electrons can easily fire the ACC. In order to keep ion events the ACC veto is disabled. *Right*: an electron/positron converting on the ECAL: when an electon/positron passes through the ECAL backsplash particles are produced (rightmost case in the figure). These particles may exit from the calorimeter surface and hit the ACC. In this case the trigger condition should be ToF and not more than 4 ACC paddles fired.

that surrounds the permanent magnet (Figure 2.9). The light coming from the scintillation panels is collected in wavelength shifter fibers of 1 mm diameter, embedded in grooves milled into the scintillation panels. At both ends of the counters, the fibers are routed in 2 bunches of 37 fibers each to transition connectors located on the conical flanges of the magnet vacuum case. From these connectors the light is routed through clear fibers up to the 8 PMTs mounted on the rim of the vacuum

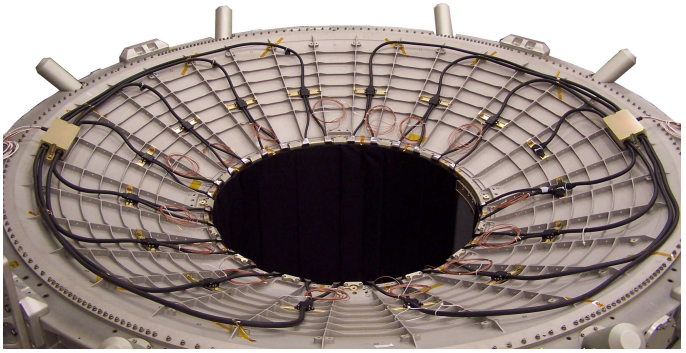

FIGURE 2.9: The ACC system mounted inside the vacuum tank. The signals from the 16 scintillation paddles, arranged on the inner cylinder of the vacuum case, are guided and coupled by wavelength shifter fibers to 8 PMTs on the border of the toroidal structure. A similar fiber/PMTs readout scheme is repeated on the other side of the vacuum case in order to provide redundancy of the veto system.

case. The ACC PMTs, similar to the ToF ones, are placed approximately 40 cm from the racetrack coils and are oriented with their axes parallel to the stray field. Thanks to the very high efficiency and a high degree of homogeneity of the scintillating fibers will ensure a reliable and fast ACC veto trigger signal (see section 2.1.9) for the high inclination particles with also some impact point determination capabilities [59].

2.1.5 Transition Radiation Detector (TRD)

The Transition Radiation Detector (TRD) is placed on top of AMS, just below the tracker plane 1 and above the upper ToF. The main purpose of the TRD is to identify electrons and positrons among the overwhelming flux of protons and nuclei traversing the detector. The identification principle is based on the electromagnetic transition radiation (TR) emitted when a charged particle traverses the boundary between two media with different dielectric constants, as the result of the particle's field reformation. The AMS-02 TRD (figure 2.10), is made by 328 modules. The modules are arranged in 20 layers supported by a conical octagon made of aluminum-honeycomb walls with carbon-fiber skins and bulkheads. To provide a 3D tracking, the lower and upper four layers are oriented parallel to the AMS-02 magnetic field while the middle 12 layers run perpendicular.
Each modules contains:

- 22 mm thick polypropylene/polyethylene fiber fleece radiators, corresponding to a density of 0:06 g=cm^3. A large number of interfaces increases the probability of TR X-rays production (up to 50% for 5 GeV electrons);
- 6 mm straw tubes filled with a Xe:CO_2 (90%:10%) gas mixture operating in full–avalanche mode (1500 V). The wall of the straw tubes, made of 72 mm thick double–layered kapton–aluminum foil, works as cathode. A 30 m thick fine gold plated wire in the center of the tube works as anode for the proportional chamber.

A 20 layer prototype built with final design components was tested on lepton/hadron beam test. Highly relativistic particles crossing the TRD may produce Transition

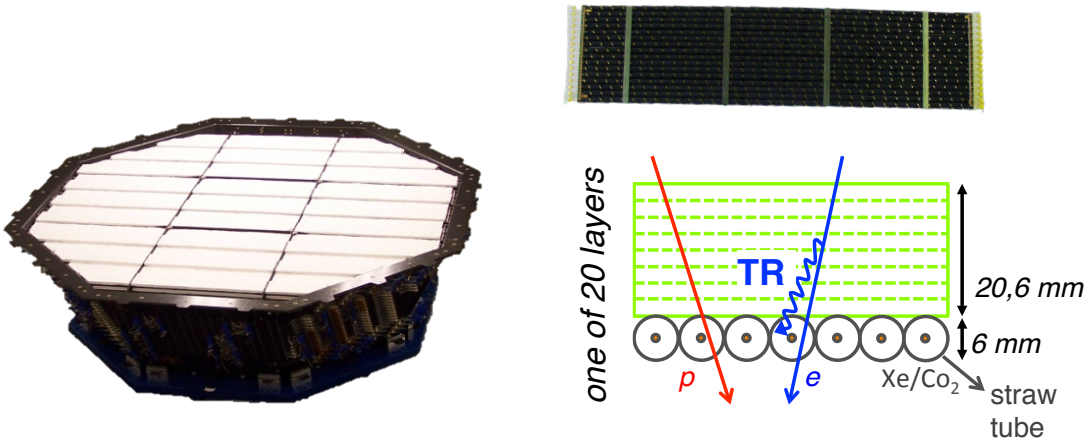

FIGURE 2.10: *Left*: a picture of the truncated octagonal pyramid AMS-02 TRD. *Right*: a picture of one of the 328 modules (top) and the principle of measurement of one TRD layer (bottom): the TR X-rays produced by electron in the fleece are efficiently absorbed in the straw tubes, producing a signal significantly larger respect to a proton.

radiation X-rays in the radiators. Such photons are efficiently absorbed and detected in the proportional chambers using Xe as absorber. The CO_2 works as quencher for charge multiplication. The combined measurement of the energy deposit in the 20 layers allows the TRD to discriminate $e^{\pm}$ from hadrons up to 1 TV, making it a fundamental tool for $e^{\pm}$ analyses. The electron/proton separation capabilities of the TRD are summarized in Figure 2.11. The energy deposit in each tube is read out and digitalized by a 12-bit ADC converter. The dynamic range of the read out has been set to resolve the low energy deposits for ionizing protons and to consequently maximize the electron/proton separation. The measurement of the direct ionization from nuclei $dE = dx/Z^2$ is used to infer the charge of the crossing particle up to

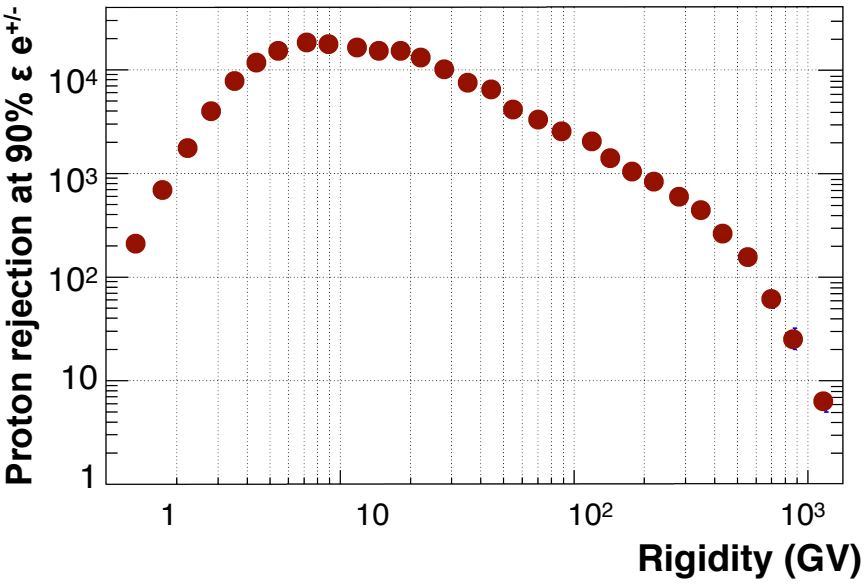

FIGURE 2.11: Electron/proton rejection measured with data collected by AMS. The e/p separation is achieved by combining the measurements of the energy deposit in the 20 layers of the TRD detector. The efficiency of the selection on e is 90%. The proton rejection is well above 10^3 up to 200 GV. At 400 GV, protons start to produce transition radiation and the TRD rejection capabilities drastically decrease.

carbon (Z = 6). Above this charge, the ADC saturates. Nevertheless, techniques based on γ–rays detection can be used to extend the identification up to iron (Z=26) [60]. In the vacuum of space, gas continuously is uses out of the straw tubes. Since CO^2 molecules are smaller than Xe molecules, they are the component leaking the most, with a total measured average leak rate of 4.5 mbar/day. In order to operate the detector at stable parameters, the TRD is coupled to a gas supplier system (see Figure 2.12). At the time of the launch, the TRD gas system was equipped with 49 Kg Xe and 5 Kg CO_2. It is composed of the two supply boxes, a mixing vessel and a circulation box. This latter is responsible to transfer the freshly mixed gas to the gas network system with the help of a pump. The complete proportional chamber gas volume amounts to 230 L. The TRD modules are connected in series in groups of 8 to form a gas circuit. The gas is circulated in a total of 41 gas circuits. After the first commissioning phase, monthly gas refills have been regularly performed since the start of the data acquisition in order to maintain an optimal gas composition for the detector performances. Moreover, daily HV adjustment are applied to correct the straw tubes gas gain change due to the continuously changing gas composition [61].

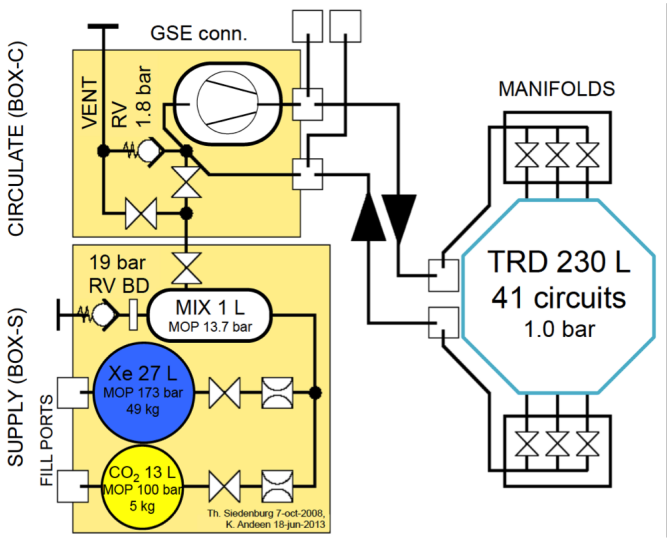

FIGURE 2.12: *Left*: TRD gas system schematic. The gas in the supply boxes is first mixed (BOX-S). A pump (BOX-C) helps the circulation of the gas through 41 gas circuits, feeding the whole TRD detection volume. Each gas circuit is composed of eight straw tubes connected in series. Ten separate manifolds with a shut-off valve control a variable number of gas circuits. Single gas groups can be isolated in case of a gas leak in a tube [61]. *Right*: a picture of the CO_2, Xe gas boxes.

2.1.6 Ring Imaging Detector (RICH)

The AMS-02 Ring Imaging Cherenkov detector (RICH) is placed below the lower ToF plane and provides a very precise measurements of β. The detection principle is based on the Cherenkov electromagnetic emission produced by a charged particle with velocity larger than the phase velocity of the electromagnetic field in the material. A cone of emission is created along the particle trajectory. The opening angle of this cone is related to the particle velocity through $\beta = 1/cos\theta(\omega)$ where $n(\omega)$ is the refraction index. Moreover, for a particle of charge Ze, the number of radiated photons per frequency unit and unit length is given by $dN^2/(d\omega dx) = \alpha Z^2 sin^2\theta$. The RICH measurement therefore also provides an independent measurement of the particle charge.

RICH consists of a radiator plane, a conical mirror and a photon detection plane. The radiator is composed by a dodecahedral polygon with a 118.5 cm internal tangent diameter. It consists of an array of 2.7 cm thick aerogel tiles with a refractive index between 1.03–1.05, which surrounds a central $35\times35\,cm^2$ region equipped with 5 mm thick sodium fluoride (NaF) radiator (nNaF = 1.335). This radiators combination optimizes the overall counter acceptance ($0.4\,m^2sr$) since the Cherenkov photons radiated by the NaF in large cones will fall within the detection area. In fact the detector plane has an empty $64\times64\,cm^2$ area in its center, matching the

active area of the electromagnetic calorimeter located below. Outside the "ECAL hole", 680 4×4-multi-anode PMTs (gain 106 at 800 V) are arranged to cover the circular 134 cm diameter surface at the basis of the conical mirror. The radiator and the detection plane are enclosed in the volume of a conical reflector multi-layer structure on a Carbon fiber reinforced composite substrate of height 47 cm. The mirror increases the RICH acceptance reflecting high inclination photons and provide the necessary photon drift ring expansion (figure 2.13). RICH provides the β measurement with a resolution $\sigma/\beta \sim 0.1\%$ for unitary charge particles, and $\sigma/\beta \sim 0.01\%$ for ions. It also provides a particle charge measurement with a charge confusion of the order of 10 %.

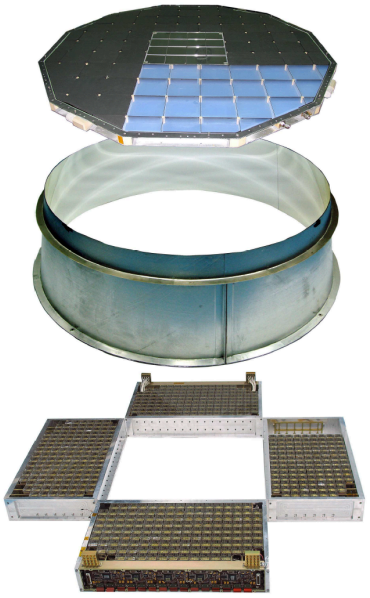

FIGURE 2.13: Exploded view of the RICH detector. It is composed by three parts: the radiators layer, the conical mirror and t he detection plane (the angular sectors of the detection plane are not shown).

2.1.7 Electromagnetic Calorimeter ECAL

The AMS ECAL is a lead-scintillating fiber sampling calorimeter [62]. Particles crossing the active volume release their energy and produce light collected by photomultipliers (PMTs) at the fiber end. The structure [63**?**] is developed to maximize the X_0/λ ratio (X_0 is the electromagnetic interaction length and λ the nuclear interaction length). It consists in a lead-fiber-glue volume ratio of 1:0.57:0.15, an average density of $\sim 6.8\,\mathrm{g/cm^3}$ and a radiation length X_0 of about 1 cm. The ECAL length corresponds to $\sim 17\,X_0$ and to only $\lambda \sim 0.6$. The active volume (*pancake*)

is built up by a pile of 9 *superlayers* (SL) consisting of 11 grooved 1 mm lead foils interleaved by 1 mm plastic scintillating fibers. The fibers are glued by means of optical cement and they run, in each superlayer, in one direction only (figure 2.14).

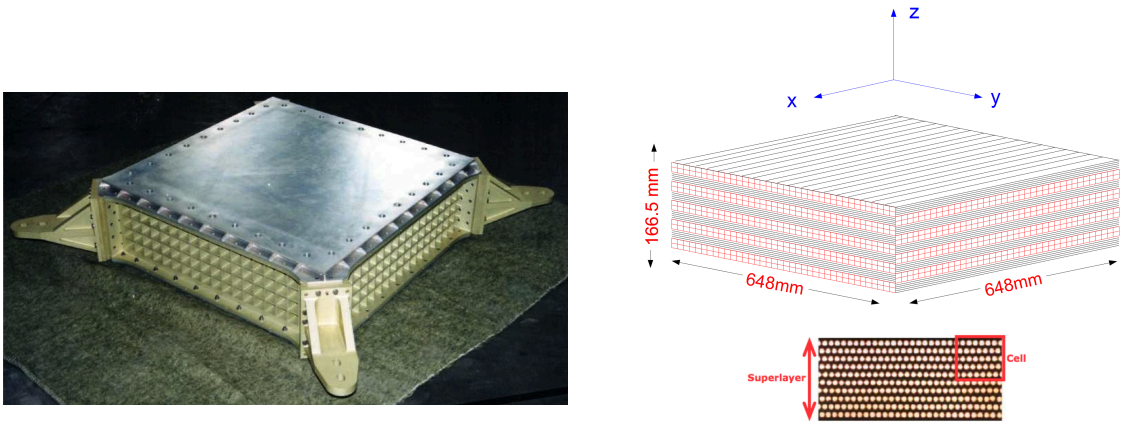

FIGURE 2.14: A picture of ECAL before the installation of PMTs (left). The scintillating fibers and lead foils structure of the 9 assembled super-layers (top right). Picture of one cell on a superlayers (bottom right.

Each superlayer is designed as a square parallelepiped with 68.5 cm side and 1.85 cm height, for a total active dimension of $68.5 \times 68.5 \times 16.7\,\mathrm{cm}^3$, corresponding to $\sim 17 X_0$ for perpendicular incident particles. The pancake has a weight of 496 Kg, for a total weight of the calorimeter of 638 Kg (including mechanical structures and readout cables). Each superlayer is read out on one end only by 36 PMTs, alternately arranged on the two opposite sides to avoid mechanical interference. The PMTs are shielded from magnetic field by a 1 mm thick soft iron square parallelepiped tube, which also acts as mechanical support for the light collection system. Each PMT accommodates four $8.9 \times 8.9\,\mathrm{mm}^2$ anodes. The anodes define the ECAL granularity, for a total of $18 \times 72 = 1296$ readout cells. The 3D imaging of shower development is achieved by alternating 5 SLs with fibers along the x axis and 4 SLs with fibers along the y axis. The ECAL Moliére radius, measured to be ~ 2 cm, corresponds approximately to 1 PMT width. In order to obtain the necessary sensitivity on minimum ionizing particles ($\sim$7 MeV/cell) and to measure energies up to 1 TeV ($\sim$60 GeV/cell) using standard 12-bit ADCs, the digitization is performed by the front-end readout system at two different gains, with a gain ratio of about 33. Besides the eight signal from anodes, each PMT's last dynode signal is also read out and its information used to have a redundant signal in case of anode breakdowns and also to build up the ECAL standalone trigger (see Section **??**). Each ECAL PMT

response is equalized by setting the PMT gain to a common value and correcting the residual response of each cell to hadronic MIP particles offline [64]. Electrons, positrons and photons reaching ECAL interact starting an electromagnetic shower. The mean longitudinal profile of the energy deposit by an electromagnetic shower is usually described by a gamma distribution [65]:

$$\langle \frac{1}{E}\frac{dE(t)}{dt} \rangle = \frac{(\beta t)^{\alpha-1} e^{-\beta t}}{\Gamma(\alpha)} \tag{2.1}$$

where $t = x/X_0$ is the shower depth in units of radiation length, $\beta \sim 0.5$ is the scaling parameter and α the shape parameter. The total thickness of the ECAL ($\sim 17\, X_0$) allows the containment of 75% of the shower energy deposit for 1 TeV $e^{\pm}$. The energy of the incoming particle is measured applying corrections for the rear and lateral energy leakage, and for the anode efficiency, to the deposited energy. These corrections ensure the energy linearity to be under control to better than 1% up to 300 GeV. The calorimeter energy resolution $\sigma(E) = E$ has been measured during the test beams [66] (see Figure 2.15) and can be parametrized as a function of the particle energy E by:

$$\frac{\sigma(E)}{E} = \frac{10.4 \pm 0.2}{\sqrt{E(GeV)}}\% \oplus (1.4 \pm 0.1)\% \tag{2.2}$$

The fine ECAL 3D readout granularity allows to reconstruct the shower axis and

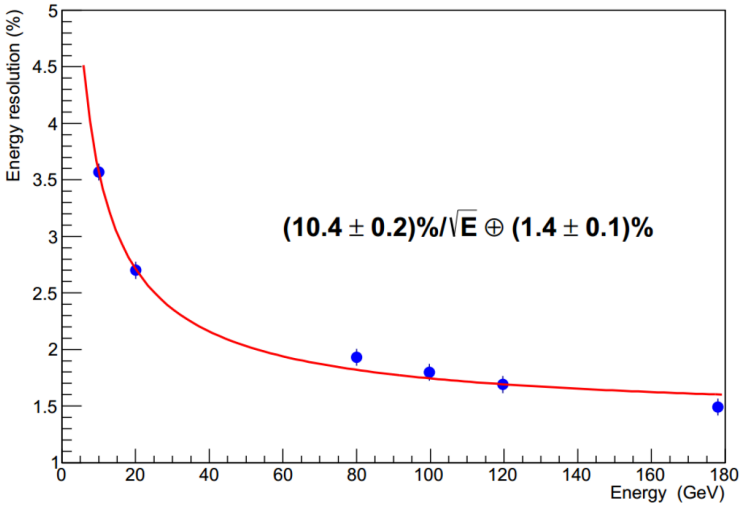

FIGURE 2.15: ECAL energy resolution measured using e^- test beams for perpendicularly incident particles [66].

direction with high precision. The ECAL pointing accuracy is an extremely important parameter for gamma ray astrophysics. The ECAL angular resolution has

been measured to be better than 1^o for energies above 50 GeV [67]. The ECAL standalone trigger, whose efficiency for non-interacting photons is better than 99% at energies above 5 GeV, allows to measure photons inside the AMS field of view and which did not interact before the calorimeter. Given the amount of radiation length X_0 in front of the calorimeter, more than 60% of photons crossing the detector from the top reach directly the calorimeter without interactions. Photons that interact in the material before the ECAL are instead measured by the detection of e^-, e^- pairs in the Silicon Tracker.

One of the main purposes of the ECAL is the identification of electrons and protons. The electromagnetic shower starting point, its shape and the matching between the deposited energy in the ECAL and the rigidity measured by the Tracker are used to identify $e^{\pm}$ while rejecting the hadronic background. The ECAL proton rejection capabilities, measured directly from data, are shown in Figure 2.16.

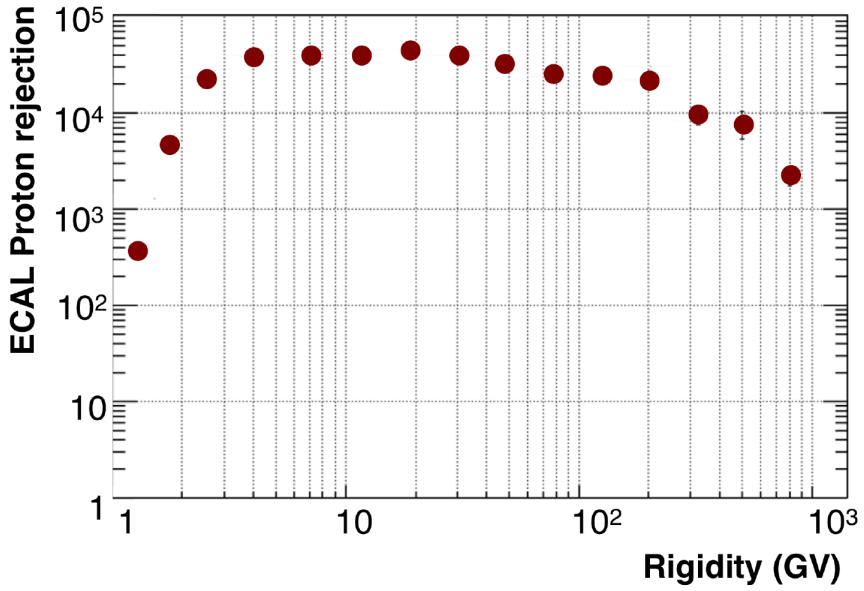

FIGURE 2.16: Electron/proton rejection measured from data collected in space using the ECAL shower topology analysis and the matching between the deposited energy in the ECAL and the rigidity measured by the Silicon Tracker. The efficiency of the selection for e^- is 90%. The proton rejection is above 10^4 in almost the whole energy range.

2.1.8 AMS electronics

The main challenge faced by the design of the AMS-02 electronics was to adapt well-known particle physics electronics to the requirements of space operations. A list of

the main challenges faced and the solutions adopted for the integration are listed in Table 2.1. The requirements for the AMS-02 electronics are more demanding than for usual space electronics due to the level of expectations in terms of performances, complexity and resource constraints such as total power consumption and total weight. One must also consider the fact the AMS-02 mission will operate in excess of 10 years with respect to the initial design of the experiment. The durability of the electronics over the years will therefore be of important concern.

	Challenges	Solutions
Static Loads	40 + 10 + 10g	Mechanical Design and Test
Vibration	6:3grms	Mechanical Design and Test
Depressurization	1 to 0 bar/2 min	Mechanical Design and Test
Zero G	Floaters	Conformal Coating
Vacuum	No Convection	Waste Heat Conduction
Thermal	- 40; $+80^o$ C -30; $+50^o$ C	Survival Parts Selection Operation Mechanical Design and Testing
Radiation	$\sim$ KRad/year	TID Testing
Heavy Ion	Latch Ups, Bit Flips	Beam Testing, Error D/C
Atomic O	Etching	Material Selection
Solar UV	Aging	Mechanical Shielding
EMC	Noise Requirements	Ground, Filter, Screen
Mag. Field	Up to $\sim$ 500 Gauss	Testing, Placement

TABLE 2.1: List of the various technical challenges faced by the design of space qualified electronics for AMS-02. Table adapted from [68].

For the best physics performances, the various sub-detectors must meet clear operational constraints : the gas gain of the TRD must be carefully controlled, the relative timing accuracy of the ToF must be of the order of 100 ps, signals as small as a few femtocoulombs must be detectable in the silicon tracker and single photons must be measurable in RICH and in the ECAL requiring a very wide operational dynamic range. All these requirements and many more add up to more than 300K electronic channels that generate about 3.7 MBit of data for each trigger.

2.1.9 The trigger logic

The main purpose of the AMS-02 trigger logic is to take a fast and efficient decision whether a particle crossing the detector has the potential to be well measured by the various sub-detectors or not. The decision is tuned to the particle properties, such as its type (photon, lepton, hadron), its charge, potentially its energy and, to some extent, it's trajectory through the detector (for example, if the particle is in

the acceptance of a specific tracker configuration or not). The AMS trigger uses the combined information coming from the ToF, ACC and ECAL sub-detectors, which are analyzed inside a dedicated electronics board, the JLV1 [69]. The processing of all the different signals takes about 200 μs which represents a significant contribution to the dead time of the experiment. This is the time while the detector is in a busy state and cannot detect new particles. In order to minimize this dead time, a complex decision tree architecture is adopted with three different stages : the *Fast*, *Level1* and *Level3* trigger logics. Only if the conditions of the previous stage are met can the next level be considered. At present, only the *Fast* and *Level 1* Trigger are used for the data acquisition. Following the lines of the presentation given in [70], we give below a brief description of the two trigger levels.

Fast Trigger

The Fast Trigger (FT) is used to make extremely fast decisions that do not contribute to any dead time and activate the Level-1 trigger logic or not. It is based on the signals received by ToF and ECAL. The ToF FT signals are constructed from combination of the digital signals received from the ToF paddles (six signals per plane) and correspond to three different categorical information about the particle:

- Charged Particle (CP) : signal constructed from a logical OR of all digital signals received from the ToF paddles. The CP is set if at least one paddle signal is above a High Threshold value (HT).
- Charged Particle in Tracker Acceptance (CT) : the signal uses only the signals from the paddles inside the Tracker acceptance.
- High Z Particle (BZ-TOF) : same as CP but the digital signals must be above a so called Super-High Threshold (SHT), which is normally associated to heavier particles (nuclei) traversing the detector.

ECAL produces only two signals based on signal detection in the x or y superlayers. The detection requires a minimum number of neighboring cells are found to have a signal above a given threshold value. The two signals are both logically OR and AND to produce two different patterns. The ToF and ECAL signals can then be combined in different logics to produce three different FT categories that can eventually be combined to produce a general FT signal :

- FTC: if any of the CP or CT conditions are set.

- FTZ: this a dedicated trigger for the detection of potential stangelets, particles expected to have a very high charge but to be very slow with respect to ions with the same charge and rigidity. The FTZ uses the combination of the top and bottom ToF planes in a extended decision time window.
- FTE: it is based on the activation of one of the two trigger patterns. If the FTE is alone (no FTC nor FTZ), the trigger is usually representative of a photon detected in the ECAL material only.

Level 1

Based on the existence of a FT, the JLV1 board enters the Level 1 (LVL1) logic evaluation, which takes exactly 1 μs. The following conditions are tested : - Charged Particles : the FT opens a 240 ns gate to latch the CP and CT charged particle signals. Both events with 3 out of 4 ToF planes and 4 out of 4 ToF planes inside the trigger are accepted. The first condition is used to construct the unbiased trigger sample.

- High Z Particles : builds the trigger for ions with looser conditions on the ACC than in the standard Charged Particle trigger.
- ACC : the signals coming from anti-coincidence counters are used to veto triggers associated with particles traversing horizontally the AMS detector. ACC signals are also associated with high activity in the detector, typical of heavy nuclei interactions with the detector material.
- ECAL-F signals : FTE signals are used to build the unbiased electromagnetic trigger.
- ECAL-A signals : used for non converting photons detected in the ECAL only.

These LVL1 triggers are added to FTE and FTZ signals to produce 8 different LVL1 sub-triggers. The 8 subtriggers can finally be OR to produce the general LVL1 trigger for the experiment. Among the various combinations offered by the trigger flexibility, 7 sub-triggers were carefully chosen for data taking on ISS :

- Unbiased charged : ToF 3/4 (HT) with a 100 pre-scaling factor.
- Single charged : ToF 4/4 (HT), NACC=0.

- Normal ions : ToF 4/4 (SHT), NACC<5.
- Slow ions : ToF 4/4 (SHT), extended gate to latch the signals to account for slow strangelet particle.
- Electrons : ToF 4/4 (SHT), both x and y ECAL super-layers.
- Photons : an ECAL shower.
- Unbiased EM : ECAL signal over threshold, pre-scaling factor of 1000.

The normal ion trigger was initially defined with no constraint on the number of ACC signals. In the first months of data taking on the ISS, the event size associated with nuclei detection showed to be higher than expected due to abundant interactions of nuclei within the detector material. In order to respect downlink and buffering capabilities onboard the instrument, it was decided to add a maximum number of ACC counts in the trigger definition.

Live-Time

The constraint of minimizing the experiments dead-time depends on several factors. As we have seen, the FT initiates a 1 μs time window for the LVL1 evaluation to take place. Based on a LVL1 trigger, the various sub-detectors start the digitization of the signals. Although carried out in parallel, a 200 μs additional dead-time is introduced. Finally, the compression of the collected signals can take up t0 300 μs. The associated dead-time is kept as low as possible by allowing the compression to take place in parallel to the digitization of the following event. This strategy is efficient as long as the buffer for the compression is not full, which usually depends on the data acquisition conditions, in particular the trigger rate. To evaluate precisely the live-time, a 20 ns scaler is used to sample continuously the status of the data acquisition, wether it is ready to accept a new event or is in a busy state.

2.1.10 The Data Acquisition System

When a charged particle crosses the top and bottom plane of the ToF instrument, or when a particle produces a shower in the ECAL, a trigger signal is initiated and sent to the various sub-detectors to record the potential associated detections. All sub-detectors in AMS-02 are equipped with dedicated Front-End electronics (FE) with a maximum readout time of 90 ns which represents, for a trigger rate of 2 kHz,

a 16% dead-time for the experiment. While the Data Acquisition System (DAQ) collects the signals from these 200 K analog channels, its main goal is to minimize the additional dead-time due to signal digitization. A schematic view of the DAQ architecture is represented in Figure 2.17. A dedicated simplified nomenclature has

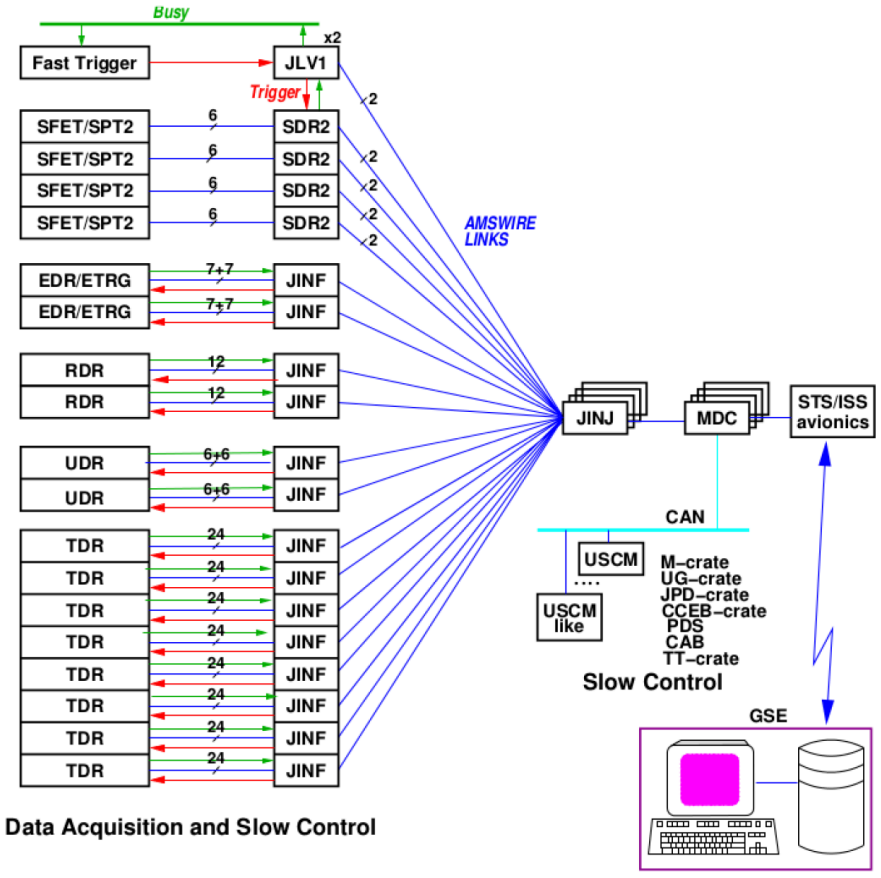

FIGURE 2.17: AMS data acquisition system. About 300,000 analog channels are processed by about 300 DSP computers in a Master-Slave based architecture. Due to the impossibility of any repair, the system has been designed allowing maximal redundancy of boards and cable connections: in case of any failure, the detector performance is not degraded [71].

been adopted to identify uniquely each sub-detector: U stands for the TRD, S for the ToF and Anti-Coincidence Counters, E for the electromagnetic calorimeter, T for the Tracker, R for the RICH, and $LV1$ for the Level-1 trigger module. The architecture adopts a tree-like structure with roughly 300 computational nodes : 264 xDR nodes (DR for Data Reduction and x specifying a sub-detector) that collect the signals from the detector Front-End electronics and perform a first packaging treatment of the data, 28 JINF nodes that collect the data from the $xDRs$; 8 SDR nodes that produce the trigger signal based on ToF and ACC information as well as 2 JLV1 nodes that collect both analog and digital information to produce the

LV1 trigger. Finally, 4 JINJ nodes collect the data from the JINF, SDR and JLV1 nodes [71].

All nodes are interconnected through serial wired links and a dedicated communication protocol is used, based on a master-and-slave hierarchy. Data is sent from a slave to its master only upon the master's request. The typical transmission speed is about 7.6 Mbytes/s. Upon a LV1 trigger signal generated by the JLV1 module based on ToF, ACC and ECAL systems, and delivered to the xDRs via the JINFs, each xDR node collects, processes and stores in a internal buffer all the information related to the event. The content of this buffer is further retrieved by the master node upon request. To minimize the dead-time, event buffering is performed at each level of the architecture. The 4 JMDCs are the main computers on-board the experiment. The JMDC provides the monitoring and the control of the entire AMS instrument. It also contains a large buffer (called JBUX) to store the data, avoiding any science loss when interruptions in the transmission between the ISS and the ground take place. All the data is sent to ground through dedicated NASA interfaces (see section 2.2) and one can interact with AMS from ground through the JMDC computer. New software and new operation procedures can thus be constantly uploaded to the experiment if needed, despite AMS being in space. This flexibility, added to the high transmission bandwidth provided by NASA for transferring the collected data to ground, makes the AMS mission a truly unique space experiment. The data acquisition is organized in 23 minutes run, such that 4 runs are taken by orbit. Each two runs are intervened by a full calibration of the various sub-detectors. Twice per orbit, a dedicated procedure is used to identify and correct single electronic upsets (bit flips) in all acquisition nodes.

2.2 AMS on ISS

On the 16th of May 2011, NASA's Space Shuttle Endeavour was launched from Cape Canaveral at the Kennedy Space Center (KFC). Few hours later, the first successful power-on of the AMS-02 electronics inside the shuttle was performed from the Johnson Space Center (JSC, Houston Texas) with a first monitoring on ground of various temperatures and electrical currents. On the 19th may, AMS-02 was powered off for installation on the International Space Station. At 4:46 a.m. the same day, AMS-02 was attached to its mission site and the first activation of the full detector in space took place less than an hour later, with the first science

data arriving to ground. No damage on any of the sub-detectors due to the shuttle launch was found and all the functions are proven to be as expected. Since then, AMS-02 has been collecting cosmic ray data at a rather steady rate of about 10^{10} particles per month, 90% of which correspond to completely ionized hydrogen. The operation of AMS-02 in space is extremely challenging due to the very harsh and constantly changing thermal conditions. Whether AMS-02 is directly facing the sun or deep space results in significant temperature variations, sometimes within a single ISS orbit. The ISS completes 15.7 orbits per day at an altitude ranging from 330 km to 410 km. The performance of the various sub-detectors strongly depends on the precise understanding and control of the effects caused by such important temperature excursions.

NASA provides 3 different electrical interfaces to AMS-02 on ISS. After AMS was physically attached to its mission site, all connectors were attached to the payload. The first interface provides the power to the AMS payload. The other two interfaces are data transmission links: the Low Rate Data Link (LRDL) and the High Rate Data Link (HRDL).

Power Interface

The power on the ISS is provided by the eight large solar array panels. The power is distributed to the AMS-02 payload through two feeds with a maximum power draw allocation of 2000 W. To meet the high constraints imposed by NASA in terms of isolation, grounding, inrush current, etc., a dedicated power distribution system (PDS) was developed to distribute the ISS power input to the various sub-detectors. It has been designed to minimize the number of units directly attached to the ISS feeds and to provide the best monitoring, control and protection of the power delivered to each sub-system.

Low Rate Data Link

The LRDL is a dual serial bus link (1553B) that is split to each of the four JMDCs. To avoid single point failures, there are two such splitters which can be selected by an astronaut by swapping a cable at the bottom of the experiment during an extra-vehicular activity (EVA). Data sent from JMDC to ground using the LRDL proceeds through various units of NASA and then via radio beam to Earth using Tracking and Data Relay Satellites (TDRS). Around 20 KBits/s of data bandwidth on the LRDL is allocated to AMS-02. The expected duty cycle is about 70%. In addition, ten highly summarized bytes per second of critical health data are transmitted with

near to 100% duty cycle. In nominal conditions, all commands to operate AMS-02 originate from the POCC and follow the inverse path. The maximum command rate is about 1 Kbit/second.

High Rate Data Link

A parallel path of data transmission is organized throughout the High Rate Data Link and represents the main path for the data out of AMS-02. The transmission is based on fiber optics communication. Transmission speeds up to 90 MBit/s can be reached on-board the ISS, and the radio down link supports up to 43 Mbit/s, with a duty cycle of about 70%. The high rate link is crucial for the proper operations of AMS-02 considering the high event acquisition rate of the experiment. The average trigger rate is about 600 Hz, but can reach up to 2kHz in regions of low Earth magnetic field. The resulting average event size is about 2kBytes which represents a substantial amount of data to be downlinked to ground. The needed downlink rate is on average 10 Mbits/s. AMS currently operates with a steady value of 13 Mbits/s which can be increased upon request depending on ISS activities.

2.2.1 Thermal environment and TTCS system

On board of the ISS, AMS orbits around the Earth with a period of ∼93 minutes and is subjected to extreme thermal variations due to day/night effect during its orbits and seasonal Sun exposure variation or due to changes of the attitude of the ISS, as in the case of berthing/unberthing of visiting vehicles [72]. Since each AMS sub-detector has its own warning, operational and no-operational temperature range, AMS requires constant alertness in order to avoid damage to its electronics. For this purpose, several sensors are placed on each sub-detector and the temperatures of AMS are constantly under monitoring.

In particular, the Tracker electronics, that produces almost the whole quantity of the AMS electronics heat, has its own temperature control system: the TTCS (Tracker Thermal Control System). The AMS-02 TTCS is a mechanically pumped two-phase CO_2 cooling loop. It is able to remove 140 W of heat by means of two dedicated radiators facing outer space located on the top of AMS-02. TTCS provides also stability with respect to the environmental temperature described above.

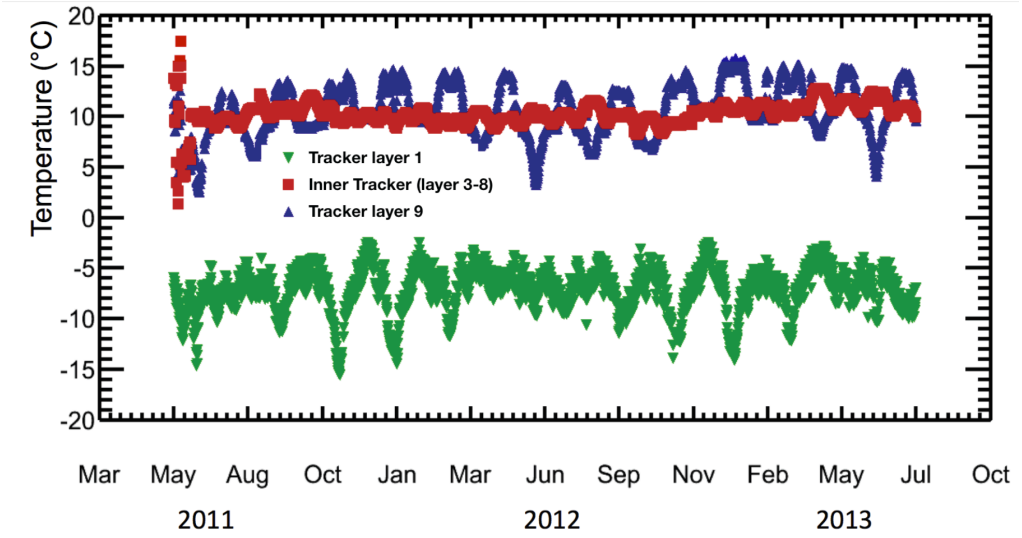

FIGURE 2.18: Time evolution of the temperature measured in different sensors thermally connected to the tracker front-end electronic of the Inner Tracker, layer 1 and layer 9.

In Figure 2.18 is shown the average temperature of the Tracker layer 1, Inner Tracker and tracker layer 9 during the first two years of operation. Since the inner tracker and layer 9 are cooled by the TTCS system, their temperature has a small variation with respect to the orbital thermal environment changes. The wide temperature variations that can be observed at the beginning of AMS-02 operations in 2011 were due to the commissioning of the TTCS system on orbit. Since the Tracker layer 1 is facing outer space, it has no need of a cooling system but a system of heaters has been installed on this layer to warm it up in the case of too low temperatures.

2.2.2 The Data Flow from ISS

Two categories of data are buffered into the main JMDC computer: science data (SCI), the data associated to the measurement by the various sub-detectors of a traversing particle, and housekeeping data (HS), consisting of various informations such as temperature readings, memory program checks (upsets and bit flips) related to the general health and status of the experiment. The latter information is crucial for fast reaction against potential damage of the payload in case of unexpected events. This is why the HS data, in parallel to being buffered in the JBUX, is also directly transferred to ground through the LRDL for real-time assessment of the payloads condition. The buffered SCI and HS data are transferred to ground through the HRDL based on the First In First Out logic (FIFO). This stream can

thus be few hours late due to low bandwidth availability or loss of satellite connexion. NASA delivers a schedule of available satellite connexions for each orbit of the ISS. This schedule is loaded inside the JMDC which automatically enables the playback from the buffer. Un-expected losses of transmission from the ISS are unavoidable contingencies of space operations. To avoid any loss of science data, a final copy of the data is sent to a laptop computer on-board the ISS through a wired link. The laptop has a 500 GB hard memory capacity, which allows to buffer approximately one continuous week of data if needed. The data from the laptop are downloaded weekly. The system is flexible enough such that the buffering in JMDC can be by-passed if real-time data is needed on ground. The data are received on ground by high rate radio frequency antennas and directed to the Marshall Space Flight Center (MSFC). A full copy of the data remains in the legal possession of NASA. The data is then copied to CERN and a copy of the housekeeping data is sent to the Taiwan control center. Data from the AMS-02 sub-detectors are collected by the JMDC in blocks of information. These blocks are separated into frames for transmission to ground. One frame corresponds to approximately 4kbytes of information. At ground, the frames are merged into packets before being copied to the CERN location. A dedicated de-framing program then recovers the original block files. These are fed to the event reconstruction software that produces the standard Root [73] files for the analysis. The reconstruction is a time consuming process and new arriving data is queued to already running processes on available computing resources at CERN. In parallel to this standard production, a special reconstruction is immediately started on dedicated machines to provide fast reconstruction of high-level event variables for a close to real-time monitoring of the detectors.

2.2.3 AMS Payload Operation Control Center

The Payload Operation Control Center, the POCC, is located on the French border side of CERN, in Prevessin. It is a single building fully dedicated to the control of AMS-02 operations on-board the ISS. The control center was certified by NASA authorities prior to starting operations. The POCC is occupied every single day of the year, day and night, by a team of experts that monitor the health and status of the payload in successive shifts of 8 hours. A picture of the CERN POCC is shown in Figure 2.19. Five positions are occupied:

FIGURE 2.19: Picture of the AMS POCC at Cern Prevessin. A big central screen displays the position of the ISS at any moment in time.

- **LEAD**: is the main responsible for the operations inside the POCC. LEAD deals with direct communication with NASA collaborators responsible for ISS activities management (Debris Avoidance Maneuver, astronaut crew activity, etc.). LEAD is the only authority in the POCC to allow commanding actions to the payload.

- **DATA**: the DATA shifter controls the flow of data from the ISS to ground and to the various locations on earth, primarily the CERN POCC.

- **THERMAL**: monitors the hundreds of temperature readings provided by sensors placed in various places in the detector. It continuously assesses potential risks due to up-coming events associated with unexpected temperature excursions.

- **PM**: controls the proper functioning of the RICH, the ECAL and the ToF subdetectors.

- **TEE**: controls the proper functioning of the TRD and the Silicon Tracker.

Two years after the beginning of the science activities on the ISS, a second POCC center was opened in CIU, Taiwan. Profiting from the different time zones, PM and

TEE shifters are substituted by people in Taiwan during night time in Europe. The LEAD and THERMAL positions remain at all time occupied at CERN, only location allowed to communicate with NASA teams through the official International Voice Loop System (Ivods).

2.2.4 Data Processing and Event Reconstruction on Ground

In the first level of the reconstruction, all sub-detectors are treated separately as standalone systems. The raw data registered by the nodes is fed to pattern recognition algorithms that reconstruct low level information such as groups of channels above a given threshold (later called clusters), the corresponding total integrated signal, etc. This information is used to reconstruct higher level information such as particle trajectory finding and association with other detectors. One usually ends up with a high-level object like a particle, for which the minimum requirement is to have a reconstructed tracker track and a velocity measurement by the ToF. The format used to save the results of the reconstruction is a Tree like data structure using the Root framework [73].

Chapter 3

Definition

In this chapter, the definition of flux is introduce. All the ingredients for its measurement will be discussed and the AMS data and Monte Carlo simulation used in this analysis will be presented.

3.1 Flux definition

The flux of a cosmic ray specie i^{th} (Φ_i), is defined as the number of particles of the i^{th} specie in a certain point of space per time, area, energy and solid angle unit. It is measured in units of $(\mathrm{GeV\,m^2\,s\,sr})^{-1}$ and in general (Φ_i) depends on energy E, solid angle Ω, time t and spatial coordinate $\overrightarrow{r}$ and, according to its definition, can be written as:

$$\Phi(E,t,\Omega,\overrightarrow{r}) = \frac{\mathrm{d}N_i(E,t,\Omega,\overrightarrow{r})}{\mathrm{d}t\,\mathrm{d}E\,\mathrm{d}S\,\mathrm{d}\omega} \quad (GeV^{-1}\,m^{-2}\,sr^{-1}\,s^{-1}) \tag{3.1}$$

where $N_i(E,t,\Omega,\overrightarrow{r})$ is the number of the particles for the specie i^{th} at the distance $\overrightarrow{r}$ with energy E, at time t, in the solid angle Ω and traversing an area S.

The direct measurement of the flux intensity for the specie i^{th} is reached by collecting the number $N_i(E,t,\Omega,\overrightarrow{r})$ of particles of the i^{th} specie. However it is impossible to perform a continuous measurement with a real detector, but N_i will be collected in a finite size interval of E, t, and Ω. Moreover, the measured flux intensity is a physical quantity that depends on the detector and its properties. In order to have the value of the flux at the top of the instrument, the measured intensity should be corrected with a factor $F(E,\Omega,t)$ that takes into account the detector properties.

Assuming no dependence from $\overrightarrow{r}$, as originally discussed in [**?**] the number of events N_i collected by a detector of area S, in a energy interval ΔE, time interval Δt and in a solid angle $\Delta\Omega$ is related to the flux (Φ_i) by the relation:

$$N_i(\Delta E, \Delta\Omega, \Delta t) = \int_0^S \int_0^{\Delta E} \int_0^{\Delta t} \int_0^{\Delta\Omega} \Phi_i(E', \Omega', t')\ F_i(E', \Omega', t')\ \hat{r'} \cdot \mathrm{d}\overrightarrow{S'}\ \mathrm{dE'}\ \mathrm{dt'}\ \mathrm{d}\Omega' \tag{3.2}$$

where $\hat{r'} \cdot \mathrm{d}\overrightarrow{S'}$ is the differential area of the detector crossed by the particle in the direction of $\mathrm{d}\Omega'$, which is integrated over the full detector area S. The factor $F(E', \Omega', t')$ that takes into account the detector properties, can be factorized as follow:

$$F_i(E', \Omega', t') = L(t')\epsilon_{\mathrm{cutoff}}(E', \Omega', t')\epsilon_i(E', \Omega', t') \tag{3.3}$$

where:

- $L(t')$ is the livetime of the detector, defined as the fraction of time during which the instrument is able to detect and record an event. It depends only by time;
- $\epsilon_{\mathrm{cutoff}}(E', \Omega', t')$ takes into account the *cutoff* effect (see section 4.1.4);
- $\epsilon_i(E', \Omega', t')$ is the efficiency of the instrument detection for the specie i^{th}.

Assuming that inside the time interval Δt the detector response doesn't change, it is possible to regroup the all time dependent effects into a factor $\tau(E', \Omega', t')$ and write $F(E', \Omega', t')$ as follow:

$$F_i(E', \Omega', t') = \tau(E', \Omega', t')\epsilon(E', \Omega') \tag{3.4}$$

And equation 3.2 becomes:

$$N_i(\Delta E, \Delta\Omega, \Delta t) = \int_0^S \int_0^{\Delta E} \int_0^{\Delta t} \int_0^{\Delta\Omega} \Phi_i(E', \Omega', t')\ \tau(E', \Omega', t')\epsilon(E', \Omega')\ \hat{r'} \cdot \mathrm{d}\overrightarrow{S'}\ \mathrm{dE'}\ \mathrm{dt'}\ \mathrm{d}\Omega' \tag{3.5}$$

Assuming that in the time interval Δt, Φ doesn't change in time and defining the *exposure time*, i.e. the total time the instrument was "ready" for the data acquisition, as $\Delta T_{exp}(\Delta E, \Delta\Omega, \Delta t) = \int_0^{\Delta t} \tau(E', \Omega', t')\ \mathrm{dt'}$:

$$N_i(\Delta E, \Delta\Omega, \Delta t) = \Delta T_{exp}(\Delta E, \Delta\Omega, \Delta t) \int_0^S \int_0^{\Delta E} \int_0^{\Delta\Omega} \Phi_i(E', \Omega', \Delta t)\epsilon(E, \Omega)\ \hat{r'} \cdot \mathrm{d}\overrightarrow{S'}\ \mathrm{dE'}\ \mathrm{d}\Omega' \tag{3.6}$$

here it is assumed that ΔT_{exp} doesn't depend on time, energy and Ω at least in the considered intervals ΔE, Δt, $\Delta\Omega$.

Defining the *effective acceptance* of the detector as:

$$A_{eff}(\Delta E, \Delta\Omega, \Delta t) = \int_0^S \int_0^{\Delta\Omega} \epsilon(E', \Omega')\ \hat{r'} \cdot \mathrm{d}\overrightarrow{S'}\ \mathrm{d}\Omega' \tag{3.7}$$

the equation 3.6 becomes:

$$N_i(\Delta E, \Delta t, \Delta\Omega) = \Delta T_{exp}(\Delta E, \Delta t, \Delta\Omega) \int_0^{\Delta\Omega} \int_0^{\Delta E} \Phi_i(E', t', \Omega')\ A_{eff}(E', t', \Omega')\ \mathrm{dE}'\ \mathrm{d}\Omega' \tag{3.8}$$

from which it is possible to obtain the formula for the *differential flux*:

$$\frac{\mathrm{d}\Phi(\Delta\mathrm{E}, \Delta\mathrm{t}, \Omega)}{\mathrm{d}\Omega} = \frac{\Delta N_i(\Delta E, \Delta t, \Delta\Omega)}{\Delta T_{exp}(\Delta E, \Delta t, \Delta\Omega)\ A_{eff}(\Delta E, \Delta t, \Delta\Omega)\ \Delta E} \tag{3.9}$$

The measurement of the *differential flux* is of particular interest for directional analysis, like the search for anisotropy signals in the antimatter fluxes. The knowledge of the differential response of the detector is a major prerequisite for such purpose.

However in this work only the absolute flux measurement will be taken into account and the formula which has been used, is obtained from 3.9 integrated over the full solid angle:

$$\Phi(\Delta E, \Delta t) = \frac{\Delta N_i(\Delta E, \Delta t)}{\Delta T_{exp}(\Delta E, \Delta t)\ A_{eff}(\Delta E, \Delta t)\ \Delta E} \tag{3.10}$$

The effective acceptance of the detector can be written as follow:

$$A_{eff} = \epsilon_{trigg}(\Delta E, \Delta t) A_{MC}(\Delta E) K(\Delta E, \Delta t) \tag{3.11}$$

where:

- $\epsilon_{trigg}(\Delta E, \Delta t)$ is the *trigger efficiency* of the detector;
- $A_{MC}(\Delta E)$ is the *Acceptance* of the detector, that include both the geometrical and selection efficiencies and is evaluated from Monte Carlo data;
- $K(\Delta E, \Delta t)$ is a *correction factor* for $A_{MC}(\Delta E)$ that taken into account the DATA/MC differences.

Finally, the formula that has to been used to the measurement of electrons or positrons flux ($i = e^{\pm}$) is:

$$\Phi_{e^{\pm}}(\Delta E, \Delta t) = \frac{\Delta N_{e^{\pm}}(\Delta E, \Delta t)}{\Delta T_{exp}(\Delta E, \Delta t)\ \epsilon_{trigg}(\Delta E, \Delta t) A_{MC}(\Delta E) K(\Delta E, \Delta t)\ \Delta E} \quad (3.12)$$

According to equation 3.12, in order to measure the electrons and positrons fluxes, the ingredients are:

- $N_{e^{\pm}}(\Delta E, \Delta t)$: **Number of recorded electrons or positrons** collected in the time interval Δt and energy interval ΔE;
- $\Delta T_{exp}(\Delta E, \Delta t)$: **exposure time** in the time interval Δt and energy interval ΔE;
- $\epsilon_{trigg}(\Delta E, \Delta t)$: **trigger efficiency** evaluated in each time interval Δt and energy interval ΔE;
- $A_{MC}(\Delta E)$: **Acceptance** of the detector, calculated by mean of MC electrons;
- $K(\Delta E, \Delta t)$: **Acceptance correction** that take into account the difference between DATA and MonteCarlo.

In this chapter will be discussed the method applied for the calculation of ΔT_{exp}, ϵ_{trigg}, $A_{MC}(\Delta E)$, $K(\Delta E, \Delta t)$. In chapter 4, will be discussed in detail the extraction of the signal of $N_{e^{\pm}}$ and in chapter 5 will be discussed the study as a function of time of the efficiencies used for the calculation of ϵ_{trigg}, $A_{MC}(\Delta E)$ and $K(\Delta E, \Delta t)$.

3.2 Data analyzed

For this work, both flight data collected by AMS and simulated MonteCarlo data have been used.

DATA

In this work the term "DATA" will refer to the data collected by AMS. The DATA that have been used for this analysis correspond to the events that have been collected in the first 30 months of AMS data-taking (May 20, 2011 – Nov 29 2013). A total of 41×10^9 events have been analyzed.

MC

The term "MC" will refer to simulated events with the Monte Carlo method. Both electrons and protons MC have been used.

The electrons MC sample has been used for the calculation of the *Acceptance* A_{MC} (more details in section **??**. For this purpose three dataset of electrons, generated in three different energy range, have been used for a total of 4.96×10^{10} events:

- 37.0×10^9 simulated events in the energy range 0.25–5 GeV;
- 11.8×10^9 simulated events in the energy range 5.–100. GeV;
- 0.07×10^9 simulated events in the energy range 100.–2000. GeV;

The simulated electrons are generated from the first plane of a cube of side 3.9 m that surrounds AMS-02 as show in figure 3.1.

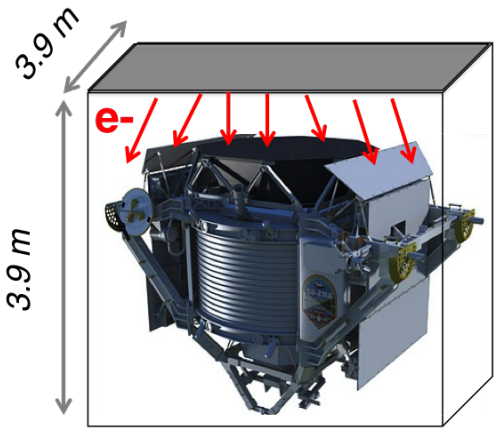

FIGURE 3.1: Plane of generation of the simulated electrons used for the calculation of the acceptance.

A protons MC sample has been used for the study of the irreducible background, constituted by interacting protons with the AMS material that produce secondary electrons that are detected as primary (see section 4.1.3). For this purpose three dataset of protons, generated in three different energy range, have been used for a total of 1.2×10^{11} events:

- 0.1×10^9 simulated events in the energy range 0.5–10 GeV;
- 0.15×10^9 simulated events in the energy range 10.–200. GeV;
- 122.0×10^9 simulated events in the energy range 200.–4000. GeV;

The simulated protons are generated from the first plane of a cube of side 3.9 m that surrounds AMS-02 as show in figure 3.1.

3.2.1 Reweight of MC

The generated MC energy spectrum, $\left(\frac{dN}{dE}\right)_{MC}$, doesn't follow a power law as a function of energy as the real DATA spectrum, $\left(\frac{dN}{dE}\right)_{DATA}$. Moreover the statistic between the generated intervals is different and this feature causes discontinuities in $\left(\frac{dN}{dE}\right)_{MC}$. This behaviors can be clearly see in figure 3.2 in which the energy spectrum for an electrons MC sample and an electrons DATA sample as a function of the generated energy (for MC) and reconstructed energy (for DATA) are compared.

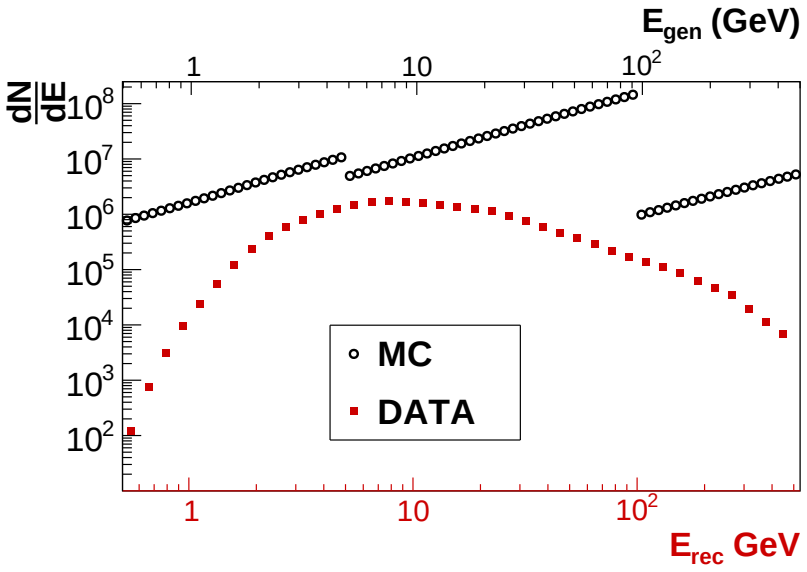

FIGURE 3.2: Energy spectrum of electrons DATA (red point) as a function of the reconstructed energy and of electrons MC (black point) as a function of generated energy.

This features don't represent a problem in the calculation of the acceptance A_{MC} due to the method applied for its evaluation (see section **??**). However, for the evaluation of the efficiencies used in the calculation of $K(\Delta E, \Delta t)$ and for the estimation of the *irreducible background* from protons, the energy spectrum of generated MC events should be:

1. reweighed, in order to have the same trend of as a function of energy observed on DATA;
2. normalized, in order to have a continuos shape as a function of energy (no "jump" between two different intervals of generation).
3. normalized, in order to have the same statistic of DATA.

The first two items are mandatory to have a correct simulation of the DATA trends as a function of reconstructed variables. The third item is needed if, in addition to the trends, a correct simulation of the DATA statistic as a function of reconstructed variables is requested[1].

The MC events are generated in an energy interval ΔE_{gen}=$[E_{min}, E_{max}]$ following a flat distribution as a function of logarithm of energy as shown in figure 3.3. This means that:

$$\left(\frac{dN}{d(lnE)}\right)_{\text{MC}} = \left(\frac{dN}{\frac{1}{E}d(E)}\right)_{\text{MC}} = k = costant$$

$$\rightarrow \quad \int_0^{N_{gen}^{[E_{min},E_{max}]}} dN = \int_{E_{min}}^{E_{max}} k\frac{1}{E}dE \tag{3.13}$$

$$\rightarrow \quad N_{gen}^{[E_{min},E_{max}]} = k(lnE_{max} - lnE_{min})$$

Equation 3.15 brings to a value of the constant k of:

$$k = \frac{N_{gen}^{[E_{min},E_{max}]}}{lnE_{max} - lnE_{min}} \tag{3.14}$$

and to a generated spectrum of:

$$\left(\frac{dN}{dE}\right)_{\text{MC}} = \frac{N_{gen}^{[E_{min},E_{max}]}}{lnE_{max} - lnE_{min}} \tag{3.15}$$

Since computationally all the quantities are evaluated in finite size intervals, equation 3.15 becomes:

$$\left(\frac{\Delta N}{\Delta E}\right)_{\text{MC}} = \frac{N_{gen}^{[E_{min},E_{max}]}}{lnE_{max} - lnE_{min}} \tag{3.16}$$

In order to have the correct shape and statistic of the spectrum, a weight factor w should be applied so that:

$$w \times \Phi_{\text{MC}} = \Phi_{\text{DATA}} \quad \rightarrow \quad w = \frac{\Phi_{\text{DATA}}}{\Phi_{\text{MC}}} \tag{3.17}$$

where, according to the equation 3.10:

$$\Phi_{\text{MC}} = \left(\frac{\Delta N}{\Delta E}\right)_{\text{MC}} \frac{1}{A_{\text{eff}}\Delta T_{\text{exp}}} \tag{3.18}$$

[1]This is the case for the study of the *irreducible background*

In the case of generated flux, the acceptance is given only by a geometrical factor that depends on the surface used for the generation (see section **??**). The MC events used in this work, have been generated from a single surface of a cube of side l, this means:

$$A_{\text{eff}} = G = \pi l^2 \tag{3.19}$$

The exposure time, correspond to the one in which the Φ_{DATA} is measured. In this way the MC flux is normalized to the same statistic of DATA.

Combining equations **??** the obtained value of w is:

$$w = \frac{\Phi_{\text{DATA}}}{\left(\frac{\Delta N}{\Delta E}\right)_{\text{MC}}} A_{\text{eff}} \Delta T_{\text{exp}} \tag{3.20}$$

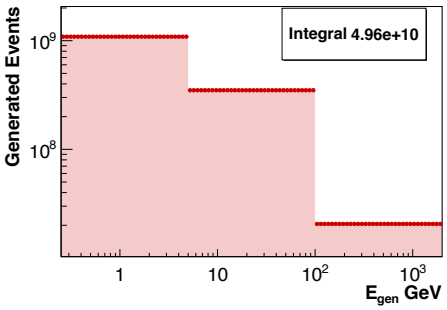

FIGURE 3.3: Number of generated events for MC electrons samples as a function of the generated energy (E_{gen}).

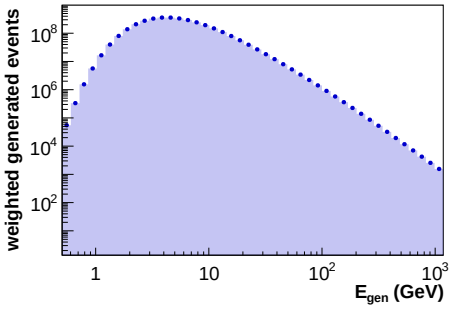

FIGURE 3.4: Reweighed number of generated events in MC electrons samples as a function of the generated energy (E_{gen}).

w has been evaluated and applied as a function of energy. The resulting reweighed generated spectrum in the case of electrons MC is shown in figure **??**. The same argument can be assessed in case of MC protons.

The results obtained from a fit to the published electrons[46] and protons fluxes [74], have been used for the evaluation of Φ_{DATA} in equation 3.20. The parametrization of the fluxes obtained from the fit are shown in figures3.5 and 3.6 respectively for electrons and protons flux.

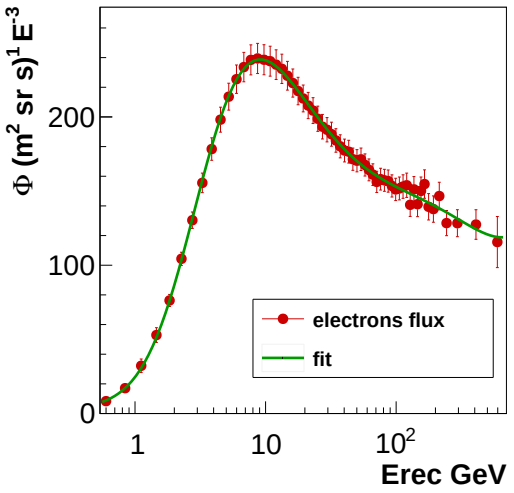

FIGURE 3.5: Fit on the published electrons flux [46]. The result from the fit is used in the formula 3.20 to evaluate the weight factor w for MC electrons.

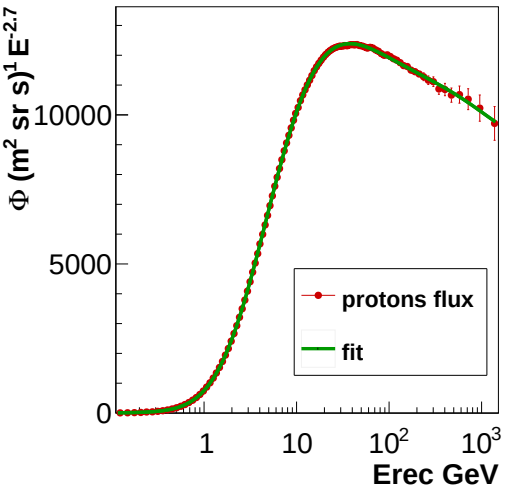

FIGURE 3.6: Fit on the published protons flux [74]. The result from the fit is used in the formula 3.20 to evaluate the weight factor w for MC protons.

3.3 Acceptance, A_{MC}

The *acceptance* in a given energy interval ΔE for a sample obtained applying a sequence of cuts, can be written as:

$$A_{\mathrm{MC}}(\Delta E) = \frac{N_{\mathrm{sel}}(\Delta E)}{N_{TOT}(\Delta E)} \cdot G \tag{3.21}$$

where:

- $N_{\mathrm{sel}}(\Delta E)$ are the number of events after the selection with energy within the interval ΔE;
- $N_{TOT}(\Delta E)$ are the total number of events with energy within the interval ΔE that reach the detector;
- G is the *Acceptance of generation* and it is constant as a function of energy. As explained in [**?**], G is a geometrical factor that depends on the shape of the generation plane and its unit of measurement is $m^2\,sr$. For the MC used in this analysis, the generation plane is a square of side $l = 3.9\,m$ and in this case (see [**?**]):

$$G = \pi l^2 = 47.78\,m^2\,sr \tag{3.22}$$

Using only DATA, it is impossible to know the total number $N_{TOT}(\Delta E)$ of events that reach the detector because only the events that are triggered are recorded. For this reason, the *Acceptance* used for the measurement of electrons and positrons fluxes has been evaluated on MC electrons. The total number of generated events in one energy bin of generation ($N_{gen}(\Delta E)$), corresponds to the total number of events that reach the detector (in the same energy bin ΔE:

$$N_{TOT}(\Delta E) = N_{gen}(\Delta E)$$

In order to calculate A_{MC}, $N_{\rm sel}(\Delta E)$ and $N_{gen}(\Delta E)$ have been evaluated as a function of the generated energy. Note that in this case, the result is not affected by the shape of the generated spectrum and for this reason, A_{MC} has been evaluated on a un-reweighed MC electrons sample.

A_{MC} as a function of E_{gen} is obtained dividing the distribution of $N_{\rm sel}(\Delta E)$ by $N_{gen}(\Delta E)$ and multiplying the result by the factor G. The procedure, that will be described in detail in the next subsection, is schematically shown in figure 3.7.

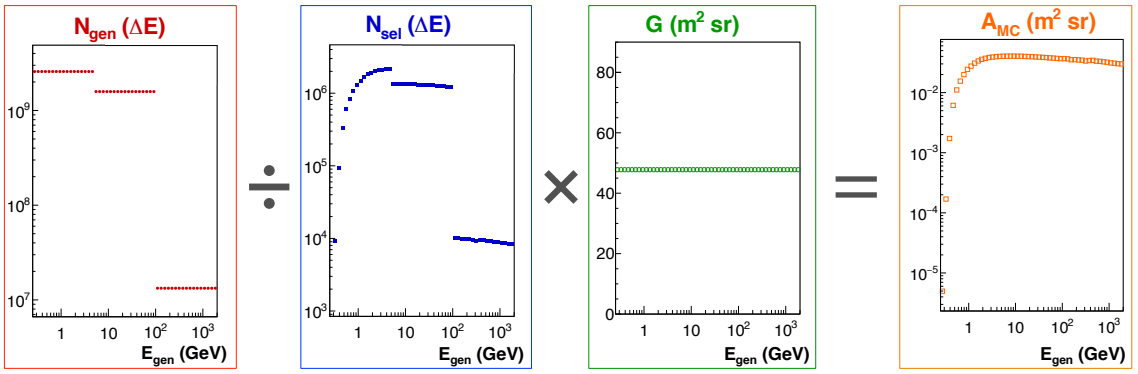

FIGURE 3.7: Schematically review of the procedure applied for the acceptance calculation.

3.3.1 The binning for A_{MC} histogram

A correct choice of the binning for the histogram of the $N_{\rm sel}$, $N_{\rm ten}$, G and consequently A_{MC}, is fundamental in order to avoid problems between two different energy intervals of generation.

MC electrons are generated in 3 different *nominal* energy intervals, $\Delta E_{\rm gen}^{NOM}$.

Each $\Delta E_{\rm gen}^{\rm NOM}$ is delimited by a *nominal* minimum value of energy, $E_{\rm NOM}^{\rm min}$, and *nominal* maximum value of energy, $E_{\rm NOM}^{\rm max}$. The 3 different intervals of generation are:

- $(\Delta E_{\rm gen}^{\rm NOM})_1 = [E_{\rm NOM})^{\rm min} - E_{\rm NOM}^{\rm max}]_1$=[0.25–5.] GeV;
- $(\Delta E_{\rm gen}^{\rm NOM})_2 = [E_{\rm NOM}^{\rm min} - E_{\rm NOM}^{\rm max}]_2$=[5.–100.] GeV;
- $(\Delta E_{\rm gen}^{\rm NOM})_3 = [E_{\rm NOM}^{\rm min} - E_{\rm NOM}^{\rm max}]_3$=[100.–2000.] GeV;

However, in each energy $\Delta E_{\rm gen}^{\rm NOM}$, the events are generated with energies between a *real* energy interval, $\Delta E_{\rm gen}^{\rm REAL}$, that is a little bigger respect to the *nominal* one. An example of this feature, is reported in table 3.1 for two different `job`[2] used for the generation of MC electrons in the $\Delta E_{\rm gen}^{\rm NOM}$=5.–100. GeV.

TABLE 3.1

	$E_{\rm NOM}^{\rm min}$	$E_{\rm NOM}^{\rm min}$	$N_{\rm gen}^{\rm NOM}$	$E_{\rm REAL}^{\rm min}$	$E_{\rm REAL}^{\rm min}$	$N_{\rm gen}^{\rm REAL}$
I `job`	5 GeV	100 GeV	425012	4.963 GeV	100.703 GeV	422974
II `job`	5 GeV	100 GeV	451521	4.921 GeV	100.593 GeV	448253

The binning for E_{gen} has been choosen in order to have, for each $\Delta E_{\rm gen}^{\rm NOM}$, one bin which low edge correspond to $E_{\rm NOM}^{\rm min}$ and one bin which up edge correspond to $E_{\rm NOM}^{\rm max}$.

Moreover, for the analysis only the MC events which generated energy is within the *nominal* value, have been taken into account.

3.3.2 The number of selected events, $N_{\rm sel}(\Delta E)$

The distribution of $N_{\rm sel}(\Delta E)$ as a function of E_{gen} has been obtained applying on MC electrons the same selection applied on DATA, described in section 4.1. The only cut that has not been applied is the request on the physics trigger since the efficiency of this cut, as will be explained in section 3.6, is evaluated directly form DATA as *last cut*. This means that it should be not include in the calculation of acceptance.

[2] for each $(\Delta E_{\rm gen}^{\rm NOM})$ several `job` are used for the MC electrons generation. Each `job` has its different $(\Delta E_{\rm gen}^{\rm REAL})$ and its different number of generated events.

3.3.3 The number of generated events, $N_{\text{sel}}(\Delta E)$

For the calculation of A_{MC} only the number of generated events inside the *nominal* interval ($N_{\text{gen}}^{\text{NOM}}$) should be taken into account.

Unfortunately, as shown in table 3.1, several job are used for one $\Delta E_{\text{gen}}^{\text{NOM}}$, each with its own $\Delta E_{\text{gen}}^{\text{REAL}}$. For each job is known the *real* energy interval of generation, and the number of events that are generated inside this interval ($N_{\text{gen}}^{\text{REAL}}$) that doesn't correspond to $N_{\text{gen}}^{\text{NOM}}$. However, exploiting the fact that the number of events in MC are generated flat as a function of the energy logarithm (see section 3.2.1), the number of generated events in the *nominal* interval can be obtained from the following formula:

$$\frac{N_{\text{gen}}^{\text{NOM}}}{\Delta E_{\text{gen}}^{\text{NOM}}} = \frac{N_{\text{gen}}^{\text{REAL}}}{\Delta E_{\text{gen}}^{\text{REAL}}} \quad \rightarrow \quad N_{\text{gen}}^{\text{NOM}} = \Delta E_{\text{gen}}^{\text{NOM}} \frac{N_{\text{gen}}^{\text{REAL}}}{\Delta E_{\text{gen}}^{\text{REAL}}} \tag{3.23}$$

3.3.4 A_{MC} result

The result for A_{MC} obtained with the procedure described above, is shown in figure 3.8.

The deviation from an expected constant behavior at high energies is to be at-

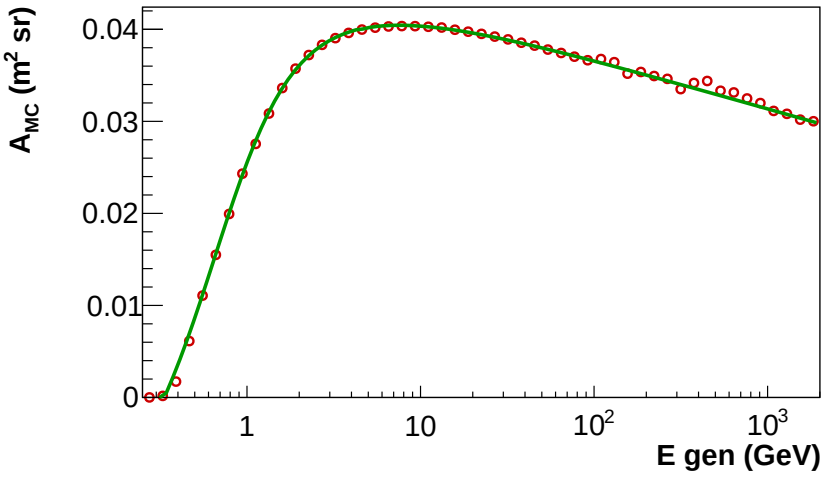

FIGURE 3.8: The obtained result for A_{MC} as a function of generated energy red point and its parametrization (green line).

tributed to the request on Z_{TRK} which at high energies has a lower efficiency on electrons. At low energies, the multiple scattering undergone by the particle in the detector material decreases the efficiency of the majority of selections, resulting in a

unavoidable suppression of the acceptance for energies below 0.5 GeV. An analytical fit has been performed on A_{MC} distribution and the value obtained from the fit is used for the evaluation of electrons and positrons fluxes, according to the equation 3.12.

The calculated acceptance relies completely on the MC simulation. This is indeed the only possible method to asses to absolute normalization of the detector acceptance. The MC simulation can, however, not be fully representative of the detector response. Therefore, a detailed comparison of data and MC is needed in order to asses the correctness of the MC simulation and, in case, correct for discrepancies. This problem will be described in detail in the in section **??**.

3.4 Acceptance correction, $K(\Delta E, \Delta t)$

The detector acceptance A_{MC}, evaluated as described in section **??**, is completely based on MC informations. Only MC, in fact, can be used to asses the absolute acceptance normalization.

The cuts contained in the preselection (see section 4.1) except the request of physic triggers, enter as a multiplicative factors with efficiency $\epsilon < 1$ in the definition of the acceptance $A_{MC}(\Delta E)$. However some details of the data, for example the interactions with the material of AMS or the geometry of the detector, may not be properly described by the MC simulation. In order to consider this problem, the $A_{MC}(\Delta E)$ is corrected by a factor that take into account the differences between data e MC.

Since some cuts efficiencies, as will be deeply discuss in chapter **??**, are both energy and time dependent also the acceptance correction factor should be dependent both from energy and time ($K(\Delta E, \Delta t)$).

The method for the calculation of the *correction factor* has been already studied and applied for the all electrons flux measurement [47]. The procedure that has been used in this work is the same, with the only exception that the $K(\Delta E)$ has been evaluated in each time interval.

In this section, the strategy used to evaluate the *correction factor* and the systematic associated to it will be reviewed.

sdsrtIn principle, the correct procedure to calculate K should be the comparison of the efficiencies between an electrons sample from DATA and an electrons sample from MC, for each cut used in the evaluation of A_{MC}. This imply an high purity of the electrons DATA sample.

However, the electrons are a rare species in the cosmic radiation. Therefore, a stronger selection than that applied during the analysis is needed to select a pure sample of electrons. On the other hand, MC simulation has been run on the electron hypothesis only. This mainly introduces some problems. First, any unavoidable proton background will contaminate the data electron sample, and could potentially induce a bias when comparing MC and data detector response. Moreover, any additional electron selection could introduce unwanted biases in the selected data or MC sample and it may hide some different features between data and MC. The selection applied for the calculation of each efficiency will be discuss in chapter **??**.

In this analysis the efficiencies in each ΔE and Δt on electrons data ($\epsilon^i_{DATA}(\Delta E, \Delta t)$) and in each ΔE on MC electrons ($\epsilon^i_{MC}(\Delta E)$) have been evaluated for each cut used in the A_{MC} calculation. The correction coming from the cut $i-th$, that has to been applied to the acceptance for the time interval Δt and energy interval ΔE ($K(\Delta E, \Delta t)^i$), is calculated as the ratio between the DATA and MC efficiencies of the cut $i-th$:

$$K(\Delta E, \Delta t)^i = \frac{\epsilon^i_{DATA}(\Delta E, \Delta t)}{\epsilon^i_{MC}(\Delta E, \Delta t)} \tag{3.24}$$

The total correction being therefore:

$$\kappa(\Delta E, \Delta t) = \prod_i K(\Delta E, \Delta t)^i \tag{3.25}$$

Figures 3.9 and 3.10 show, as a function of the reconstructed energy and for one time intervals of 27 days, respectively all the single corrections $K(\Delta E, \Delta t)^i$ for each cut applied in the A_{MC} calculation, and the obtained result for $\kappa(\Delta E, \Delta t)$.

In order to smooth out statistical fluctuations, $\kappa(\Delta E, \Delta t)$ has been parametrized using a log linear fit for energies above 2 GeV. Under 2 GeV, the correction is evaluated point by point to follow the shape.

At low energies, the discrepancies between DATA and MC correction reach 30–40% at 0.5 GeV. In the analysis, however, only half correction is applied, since there is no particular reason to privilege MC over data, or viceversa. The arbitrariness of

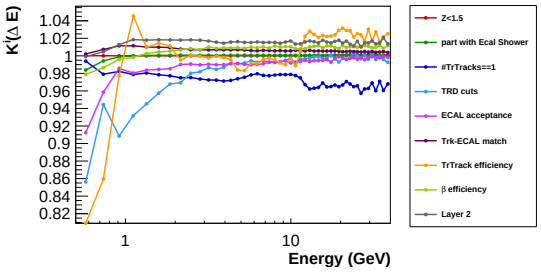

FIGURE 3.9: Single corrections $K(\Delta E, \Delta t)^i$ coming from all the cuts used in the A_{MC} calculation as a function of reconstructed energy, in one time interval of 27 days.

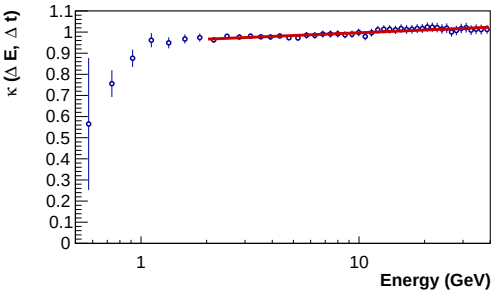

FIGURE 3.10: Total correction (κ) as a function of reconstructed energy obtained from the product of the single corrections show in figure 3.9 according to the formula 3.24, in one time interval of 27 days.

this choice is however covered by the systematic uncertainty given by the data/MC discrepancy that will be discuss in the next section. The resulting *Acceptance correction* $K(\Delta E, \Delta t)$ applied, is shown in figure 3.15.

3.4.1 Uncertainties on $K(\Delta E, \Delta t)$

Four kinds of errors have been taken into account for the uncertainties evaluation of $K(\Delta E, \Delta t)$ (σ_K).

- σ_K^{abs}: error that takes into account the deviation of $K(\Delta E)$ from 1;
- σ_K^{stab}: error that takes into account the stability in time of K;
- σ_K^{par}: error that takes into account the errors on parameter resulting from the fit performed above 2 GeV on $K(\Delta E, \Delta t)$;
- σ_K^{res}: gives the goodness of the fit performed above 2 GeV on $K(\Delta E, \Delta t)$.

The four errors have been evaluated as a function of energy and combined according to the following formula:

$$\sigma_K = \sigma_K^{abs} \bigoplus \sigma_K^{stab} \bigoplus \sigma_K^{par} \bigoplus \sigma_K^{res} \tag{3.26}$$

Absolute systematic, σ_K^{abs}

Figure 3.11 shows the deviation from 1(δ) as a function of energy for all K_i time integrated.

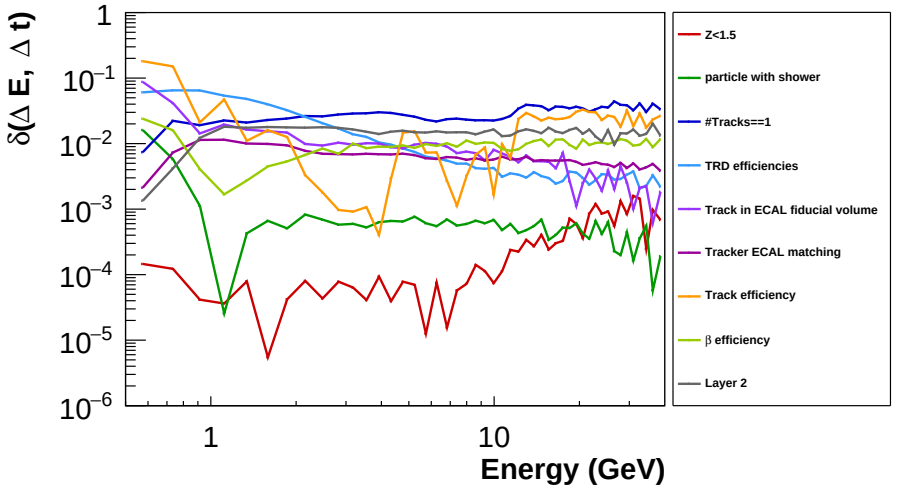

FIGURE 3.11: Deviation from 1(δ) as a function of energy for all K_i time integrated.

Some checks show a negligible or even null deviation from 1 with negligible error bars, pointing to a optimal agreement between DATA and MC. Other checks, instead, show an appreciable deviation from 1. This deviation has to be reflected from uncertainty on the knowledge of the acceptance, and it is described in this analysis by the **absolute systematic** σ_K^{abs}. For each check, the half difference of the point from the unity, $\delta_{1/2}^i$, is used as estimation of such uncertainty and the quadratic sum of every contribution defines the yield of the absolute systematic:

$$\sigma_K^{abs} = \left[\sum_i (\delta_{1/2}^i)^2\right]^{1/2} \tag{3.27}$$

σ^{abs} has been evaluated in each energy interval and time integrated, since it depends on the uncertainties of the knowledge of A_{MC}, i.e. of the knowledge of MC sample that doesn't depend on time.

As shown in figure **??**, σ^{abs} gives the major contribution to the total error σ_K.

K stabiliti in time systematic, σ_K^{stab}

The value of *acceptance correction factor* evaluated in each δt ($K^{\Delta t}$) can be different from the one evaluated over all the time ($K^{t_{TOT}}$), not only because the DATA efficiencies change in time, but it can be also due to the statistical fluctuations. This effect is included with the error σ_K^{stab}.

For each energy interval, the differences between the acceptance correction evaluated in a time interval $K^{\Delta t}$ and its mean value in the same time interval $< K^{\Delta t} >$ has been evaluated. The distribution of all the differences obtained in one energy bin is shown in figure **??** and its RMS has been taken as σ_K^{stab} for that energy bin.

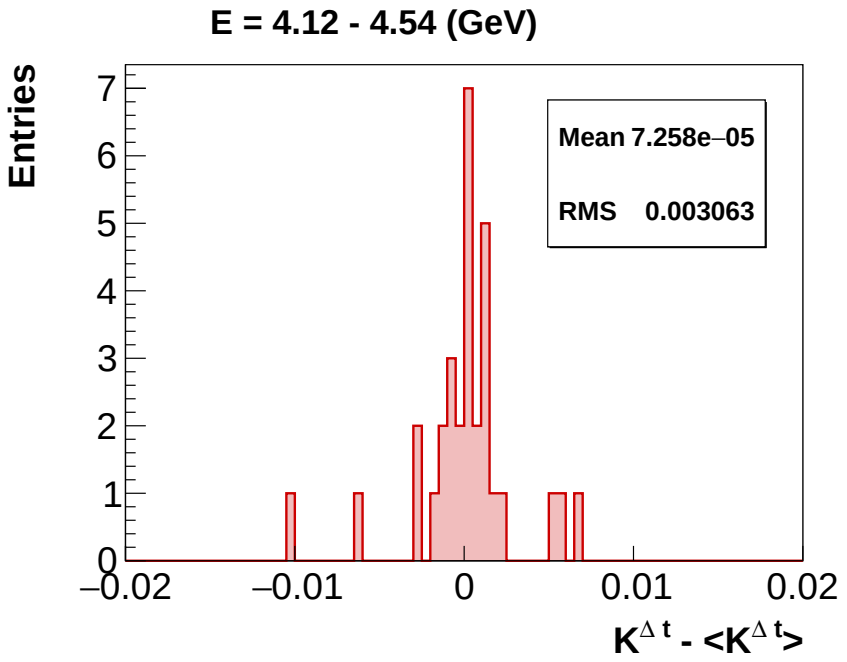

FIGURE 3.12: Distribution of difference between K and its mean value in one energy bin evaluated for all the time intervals Δt.

Particular care should be paid to the mean value of K. In order to have only the effect due to the statistical fluctuations, the mean value should be evaluated after the subtraction of the time dependencies effect of efficiencies. As will be show in chapter **??**, not all the efficiencies used for the acceptance correction are time dependent. To the time dependence of K contribute:

- The **TRD efficiency** that has a time dependence with different behaviors in each energy bin;
- The **Tracker** related efficiencies (track efficiency, single track and layer 2 efficiency) that have a time dependencies with the same effect over all energies.

An example of contribution to K from TRD efficiency in one energy bin is reported in figure 3.13. The TRD behavior as a function of time can be described by a polynomial with grade one that will be different in each energy bin. In fact, for this efficiency, as will be show in section 5.3, the time and energy dependences are correlated.

In figure 3.13 is shown the contribution to K given by the track related efficiencies. The trend as a function of time shows some step that, as will be shown in section 5.3, have the same effect over all the energies. For this reason the the contribution shown has been evaluated over all the energies. The origin of the steps is well know (see **??**).

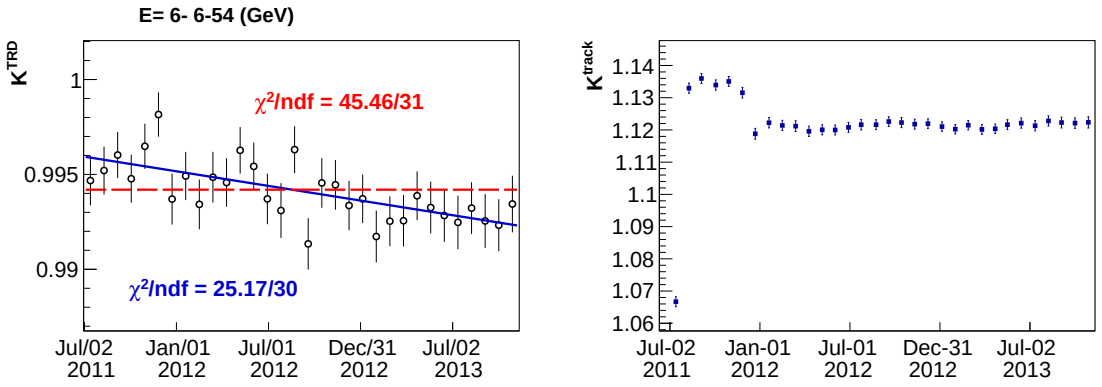

FIGURE 3.13: Contribution to K as a function of time given by the TRD efficiency (left) and Tracker (track + layer 2 + single track) efficiencies (right).

The mean value of K has been evaluated performing a fit on a *corrected* K as a function of time obtained form K after removing the jump due to the tracker as shown in figure 3.14. In this way the dependences given from the tracker efficiencies is removing. The fit has been performed using a polynomial function of grade one in order to subtract the time dependent effect given by TRD. An example of the fit is reported in figure 3.14.

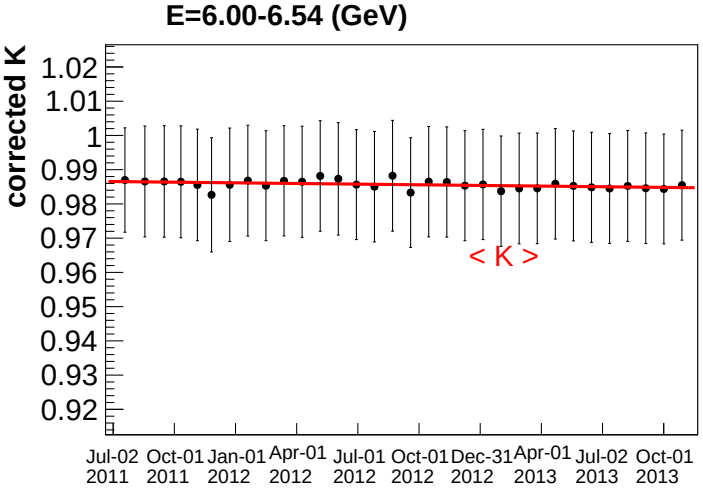

FIGURE 3.14: Fit performed on the corrected K as a function of time in order to find the mean value of K that doesn't contains any time dependences.

The obtained result is very conservative and represents a upper limit on the K stability in time uncertainty. The parametrization used to find the mean value of K, remove the main time trend but it cannot be excluded that ¡K¿ still contains trends time dependent. However, as shown in figure **??** the σ_K^{abs} contribution is very low so the fact that it represents an upper limit doesn't represent a problem.

Parametrization systematic, σ^{par}

Also the error coming from the fit performed on K should be taken into account since the parametrization can introduce some additional systematic. The error on the value of the parametrization f_K (σ^{par}) for a certain value of energy E has been found through the propagation of uncertainties of the parameters p_0 and p_1 coming from the fit

$$f_K = p_0 + p_1 log_{10} E \quad \rightarrow \quad \sigma^{par} = \sqrt{\left(\frac{\partial f_K}{\partial p_0}\right)^2 \delta p_0^2 + \left(\frac{\partial f_K}{\partial p_1}\right)^2 \delta p_1^2 + 2\left(\frac{\partial f_K}{\partial p_0}\right)\left(\frac{\partial f_K}{\partial p_1}\right)\sigma_{01}} = \sqrt{\delta p_0^2 - } \tag{3.28}$$

where σ_{01} is the $0,1$ covariance matrix element.

Residual systematic, σ^{res}

In the total error on K, the *goodness* of the fit has been taken into account considering the distance of the single fitted point respect to the value obtained from the fit:

$$\sigma^{res} = |\kappa(E) - \kappa_{FIT}(E)| \tag{3.29}$$

The obtained result has been fitted as shown in figure **??** and the result of the fit is used as value for σ^{res}.

Figure 3.15 show as a function of energy the *acceptance correction factor* K and its total relative error (σ^K/K) with the single contributions coming from the absolute, K differences, parametrization and residual systematic. This is the result obtained in one time interval of 27 days.

Since the parametrization of K as a function of energy starting from 2 GeV, there are no values for σ_K^{par} and σ_K^{res} below this energy. However, this doesn't represent a problem since the major contribution to (σ^K) is given by the absolute systematic σ^{abs} at all energies.

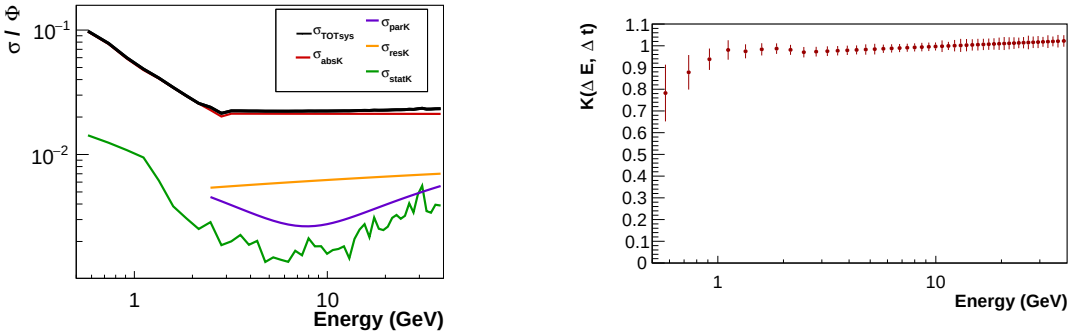

FIGURE 3.15: *Acceptance correction factor* K evaluated in a time interval of 27 days and as a function of energy (left). Total relative error (σ^K/K) with the single contributions coming from the absolute, K differences, parametrization and residual systematic for the *acceptance correction factor* K evaluated in a time interval of 27 days and as a function of energy (right).

3.5 Exposure Time

The exposure time for a given sample of taken data, does not coincide with real time interval during which the sample has been acquired.

The *exposure time* (ΔT_{exp}) for data taken in a time interval Δt has been calculated removing from Δt the time during which the experiment was busy with the electronics readout and was not ready to start the DAQ for cosmic rays that triggered the experiment. Also the seconds of not nominal data taking that are removed from the analysis sample (see section 4.1.1 are also removed from Δt.

For each Δt of data taking in which the analysis has been performed, livetime (Λ) weighted seconds passing the selection described in Section 4.1.1 have been summed up. The livetime factor takes into account the fraction of time in which the detector was not busy and consequently ready to start the DAQ. Moreover, at a certain geomagnetic coordinate, only the flux of particles with rigidities above a certain threshold is not contaminated with secondaries trapped in the geomagnetic field. Seconds of data taking are integrated to the total exposure time only in the energy bins fulfilling the selection on the geomagnetic rigidity cutoff.
The selection applied to remove secondaries trapped in the geomagnetic field, described in Section 4.1.4, introduces consequently an energy dependence in the exposure time.

Since the measurements of the $e\pm$ fluxes are binned, the exposure time has been set constant in each energy bin. For each second of DAQ the requirement on $R^{40^o}_{max}$ has been tested using the lower energy border of the bin. In the analysis, therefore,

self-consistency has been achieved by selecting particles above $R_{max}^{40^o}$ not according to their rigidity, but according to the lower energy border of the bin they belong. The formula for the calculation of the exposure time $\Delta T_{exp}(E_{min}, E_{max})$ for the energy E belonging to the bin $[E_{min}, E_{max}]$ and for data taken in the time interval $\Delta t = t_{max} - t_{min}$ reads therefore:

$$\Delta T_{exp}(E \in [E_{min}, E_{max}]) = \sum_{t=t_{min}}^{t=t_{max}} \Lambda(t)\theta(t, E_{min}) \tag{3.30}$$

where the sum runs over all the seconds of data taking and $\theta(t, E_{min})$ is a time dependent function that takes the value 1 if E_{min} is above the geomagnetic cutoff according to the procedure described before and takes the value 0 otherwise. The result of the typical exposure time obtained for a $\Delta t = 27$ days is shown in figure 3.16.

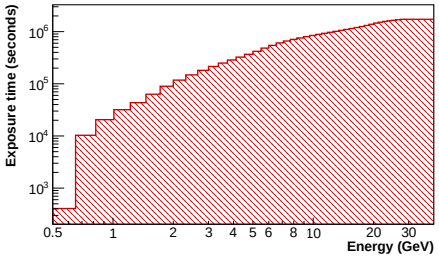

FIGURE 3.16: Typical exposure time obtained for a $\Delta t = 27$ days as a function of energy.

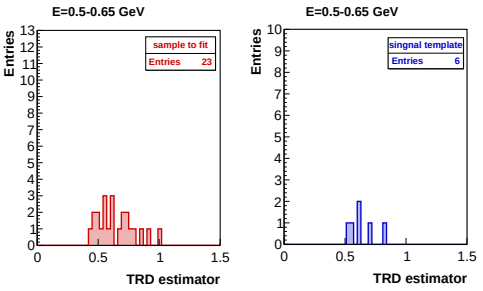

FIGURE 3.17: Sample to fit to extract an electrons signal (left) and the template for the signal (right) in the first energy bin (0.5–0.65 GeV) obtained calculating the exposure time with the same method used in [47].

However this method, that has been used for the all electrons flux analysis [47] where the analysis has been performed over a δt=30 months of data taking, presents some statistic problems in the first energy bin when are analyzed only data taken in Δt=27 days (or less). As shown in figure 3.17 the sample to fit to extract an electrons signal and the template for the signal (see **??**) contain very few events making difficult the fitting procedure.

In order to have more statistic, the first bin has been splitted in 8 energy intervals[3]. The request over the cutoff has been applied using this fine binning.

[3]The first energy bin is [0.5–0.65] GeV and it has been splitter into 8 energy sub-intervals: [0.50–0.52],[0.52–0.54],[0.54–0.56],[0.56–0.58],[0.58–0.6],[0.6–0.62],[0.62–0.64],[0.64–0.65]

In this way in the energy bin 0.5–0.65 GeV will be obtained 8 (one for each sub-interval) different numbers of events and 8 different values of exposure time.

The sample used to perform the analysis in the energy bin 0.5–0.65 GeV has been obtained summing all the events that are contained in the 8 sub-intervals. Due to the different cutoff selection, the statistic increases of a factor ~ 15 respect to the previous method as shown in figure 3.18.
Also for the exposure time should be defined one unique value for the energy interval 0.5–0.65 GeV. This value is obtained calculating the mean value of the integral[4] on the exposure time between 0.5 and 0.65 GeV (see figure 3.19). 3.16.

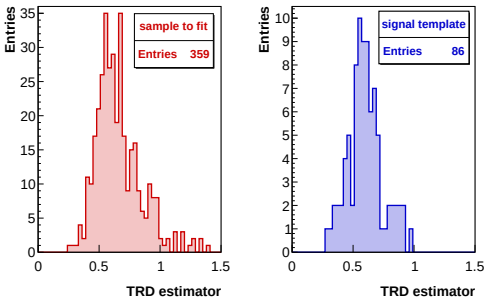

FIGURE 3.18: Sample to fit to extract an electrons signal (left) and the template for the signal (right) in the first energy bin (0.5–0.65 GeV) obtained calculating the exposure time with the *fine binning* method explained in this section.

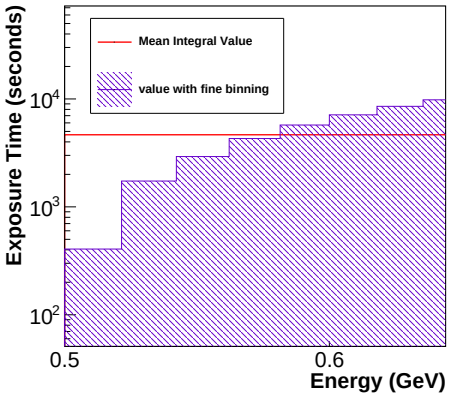

FIGURE 3.19: Comparison of exposure time obtained with different methods.

The typical value of ΔT_{exp} as a function of energy obtained for 27 days and used in the analysis is shown in figure 3.20. The mean *plateau* value of the exposure time above $\sim$30 GeV, where the effect of the geomagnetic field starts to be negligible, corresponds to an overall detector time efficiency of $\sim 80\%$.

3.6 Trigger efficiency

As has been explained in section 2.1.9 the AMS-02 trigger is based on *fast trigger* and *level 1 trigger signals (LV1)*.

The LVL1 triggers are seven:

[4] According to the *Mean Value Theorem for Integrals*

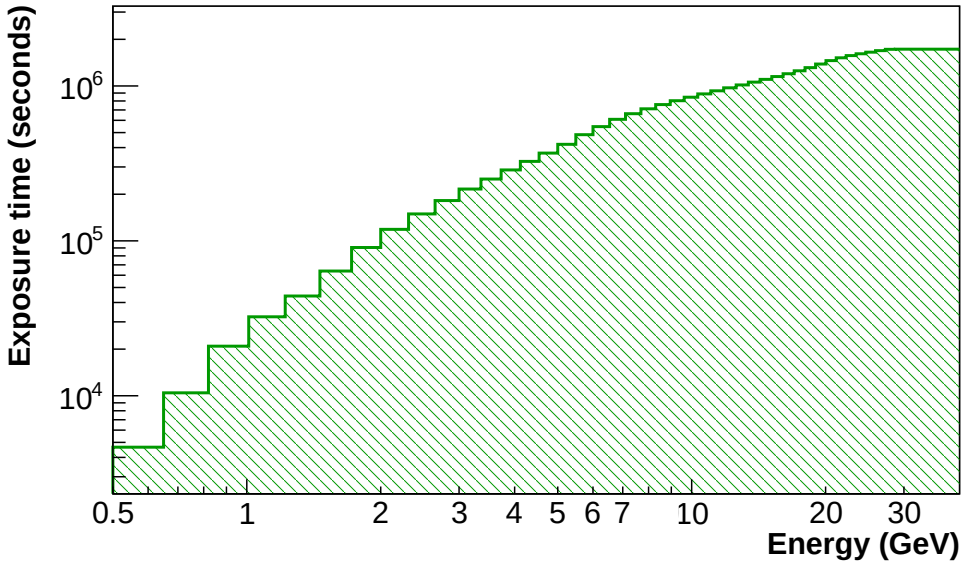

FIGURE 3.20: Typical exposure time obtained for a $\Delta t = 27$ days as a function of energy, obtained with the *fine binning* method explained in this section.

LV1-0: *Unbiased charged* (FTC) presc.factor ∼100
= 3/4 TOF HT, gate 240 ns

LV1-1: *Single charged* (FTC + ANTI)
= 4/4 TOF HT, Nacc=0, gate 240 ns

LV1-2: *Normal Ions* (FTC + Z>1)
= 4/4 TOF SHT, Nacc<5, gate 240 ns

LV1-3: *Slow Ions* (FTZ)
= 4/4 TOF SHT, gate 640 ns

LV1-4: *Electrons* (FTC & FTE)
= 4/4 TOF HT, ECALF&, gate 240 ns

LV1-5: *Photons* (FTE & ECLVL1)
= ECALA&, gate 640 ns

LV1-6: *Unbiased EM* (FTE) presc.factor ∼1000
= ECALF||, gate 240 ns

The five triggers from LV1-1 to LV1-5, are the so called "*Physics triggers* ", while the other two, LV1-0 and LV1-6, are addressed to as "*Unbiased triggers* ". This last category has been meant to be used for trigger efficiency calculation from data. For this reason, they are determined with much more loose requests respect to the

Physics triggers. Therefore, a fixed prescale factor is applied on board in order reduce the data size. The applied prescale factor is 1/100 for unbiased charge and 1/1000 for unbiased EM. This pre-scaling is not simulated on MC data.

For the calculation of Trigger efficiency, the additional category "*Not Physics Triggers*", defined by events triggered by at least one of unbiased trigger and by no Physics triggers, has been introduced. Using this category, the trigger efficiency is defined as follows:

$$\epsilon_{trigger} = \frac{\text{(Physical Triggers)}}{\text{(not Physical Trigger)} + \text{(Physical Trigger)}} \tag{3.31}$$

3.6.1 Trigger Efficiency on electrons

The formula 3.31 can be explicated in the term of LV1:

$$\epsilon_{trigger} = \frac{\text{LV1-(1 ||...|| 5)}}{[\text{w}_0*(\text{LV1-0})+\text{w}_6*(\text{LV1-6})+\text{w}_{06}*(\text{LV1-(0\&6)}]_{notPhys} + [\text{LV1-(1 ||...|| 5)}]} \tag{3.32}$$

The factors w_0, w_6 and w_{06} are the factors that should be know in order to take into account the pre-scaling of the unbiased triggers. On DATA data sample, these factors have been chosen according to the following argument.
There are three different categories of *not physics triggers*:

1) events triggered only by *unbiased charge* ($[\text{LV1-0}]_{notPhys}$)
   this category is pre-scaled on DATA data by a factor 1/100, so w_0^{DATA}=100;

2) events triggered only by unbiased ecal ($[\text{LV1-6}]_{notPhys}$)
   this category is pre-scaled on DATA data by a factor 1/1000, so w_6^{DATA}=1000;

3) events triggered only by *unbiased charge* & *unbiased ecal* ([LV1-0 & LV1-6]$_{notPhys}$).
   For this category, the chose of multiplicative factor is a little bit complicate. In principle should be:

$$w_{06} = 100 * (\text{LV1-0})_{\%} + 1000 * (\text{LV1-6})_{\%}$$

where $(\text{LV1-0})_{\%}$ are the percentages of di events triggered by unb charge and $(\text{LV1-6})_{\%}$ by unb ecal. However, due to a known malfunctioning of the trigger box on DATA data, it cannot be distinguished if an event was triggered because it was an *unbiased ecal* or an *unbiased charged*.

Otherwise, on MC data it's exactly known if an event was selected as an unbiased charged or as an unbiased ecal, or by both unbiased triggers. What has been done, it is simulating the pre-scaling also on MC data in order to estimating $(\text{LV1-0})_{\%}$ and $(\text{LV1-6})_{\%}$. In the figure 3.21 there are the distributions of the three category of *not Physics triggers* as a function of reconstructed energy, for the electrons MC sample, before the pre-scaling and in table 3.2 are reported the percentages of the three categories of unbiased over all not Physics triggers, in different low energy range.

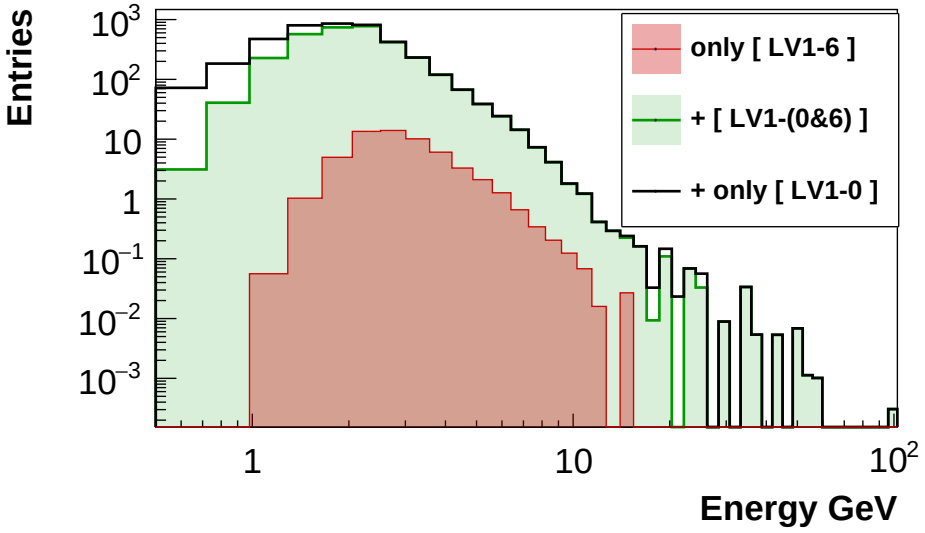

FIGURE 3.21: MC electrons: distributions of the three category of not Physics triggers as a function of reconstructed energy, before the pre scaling.

		Energy (GeV)					
		0.5-1.	1.-1.7	1.7-2.5	2.5-3.6	3.6-4.9	4.9-6.4
Not Phys %	LV1-0	82.87	37.41	9.34	0.81	0.27	5.45
	LV1-6	0	8.51	1.10	3.68	5.00	5.34
	LV1-(0&6)	17.13	62.50	89.56	95.51	94.72	94.11

TABLE 3.2: percentages of the three categories of unbiased over all not Physics triggers, in different low energy range, for MC electrons (before pre scaling).

The distributions of the three categories obtained after the application of the pre-scaling on MC data, are shown in Fig:3.22. It is possible to compare them with the same distributions obtained from DATA electrons 3.23. The percentages of the three categories of unbiased over all *not Physics triggers*, in different low energy range, both for DATA and MC electrons (after pre-scaling), are reported in tab 3.3.

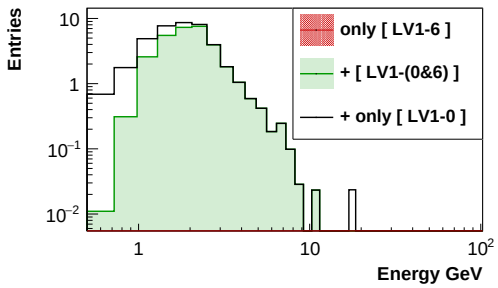

FIGURE 3.22: MC electrons: distributions of the three category of not Physics triggers as a function of reconstructed energy, after the pre scaling.

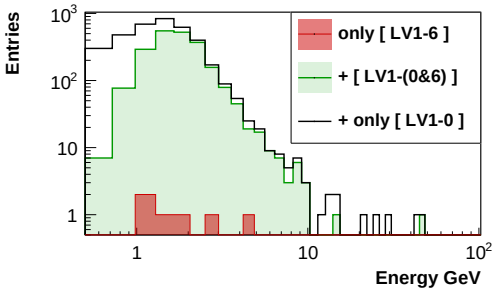

FIGURE 3.23: DATA electrons: distributions of the three category of not Physics triggers as a function of reconstructed energy.

			Energy					
			0.5-1.	1.-1.7	1.7-2.5	2.5-3.6	3.6-4.9	4.9-6.4
Not Phys (%)	LV1-0	MC	86.9	35.9	11.0	0.4	0.	0.
		DATA	84.1	40.9	12.5	3.2	6.8	0.
	LV1-6	MC	0	0	0	0	0	0
		DATA	0	0	0	0	0	0
	LV1-(0&6)	MC	13.1	64.1	88.9	99.7	1.0	1.0
		DATA	15.9	59.1	87.5	96.8	93.2	1.0

TABLE 3.3: Percentages of the three categories of unbiased over all not Physics triggers, in different low energy range, both for DATA and MC electrons (after pre scaling).

What was observed is that, after applying the pre-scaling, all the not physics triggers events on MC electrons that have both unb charge and unb ecal, are triggered because they were an *unbiased charged*, so $(\text{LV1-0})_{\%}$=100. and $(\text{LV1-6})_{\%}$=0. According to that, w_{06} as been set =100.

Figure 3.24 shows the trigger efficiency evaluated over a sample of electrons MC and electrons DATA. The cuts that have been applied on DATA in order to select an electrons sample, have been also applied on electrons MC with the purpose of remove any bias that can spoil the trigger efficiency distribution. Above 4 GeV the trigger efficiency is $\sim$ 100% both on DATA and MC. At lower energies, the value is

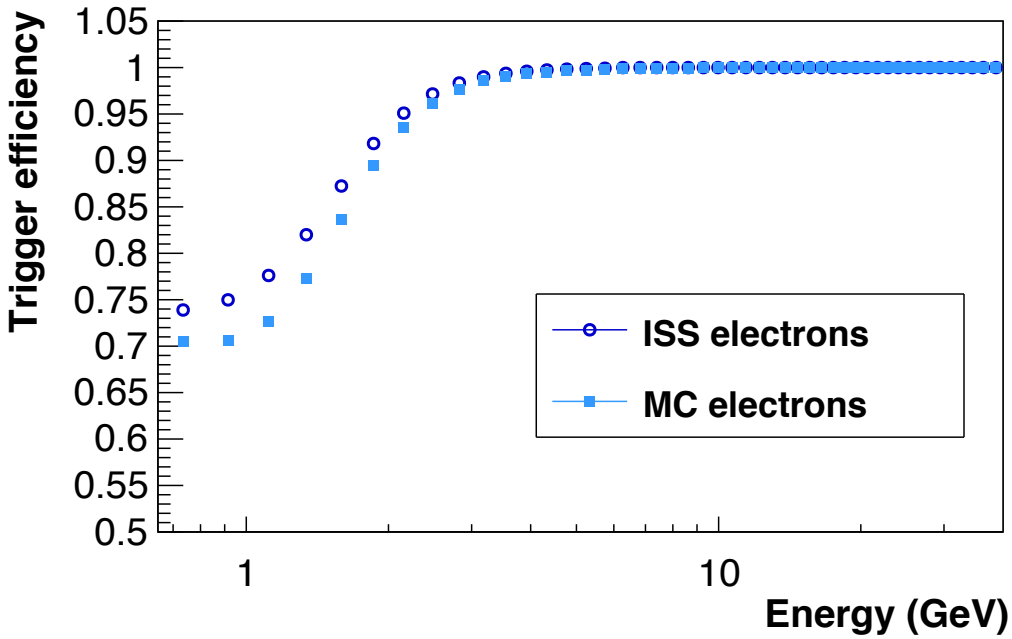

FIGURE 3.24: Trigger efficiency as a function of reconstructed energy, for MC electrons (red filled point) and DATA electrons (black empty point).

$< 100\%$ and moreover there is a big discrepancy between DATA and MC samples ($\sim 5\%$ at $\sim$1 GeV).

In order to avoid DATA/MC correction for this efficiency that would be introduce a big systematic (see section 3.4), the trigger efficiency has been evaluated directly from DATA as *last cut* according to the formula 3.32. The number of electrons with *physics trigger* and the number of electrons with *no physics triggers* has been evaluated through the fitting procedure explained in chapter **??** over a sample that satisfied the preselection 4.1[5].

All the 30 months data have been used since it was observed that trigger efficiency doesn't depend on time (see chapter **??**). The obtained result is shown in figure 3.25. In order to avoid statistic fluctuations, a fit has been performed on the distribution and the value obtained from the fit is used in the calculation of the flux.

[5]for the *no physics trigger* the request to have *physics triggers* contained in the preselection 4.1 has been changed in the request to have *no physics triggers*

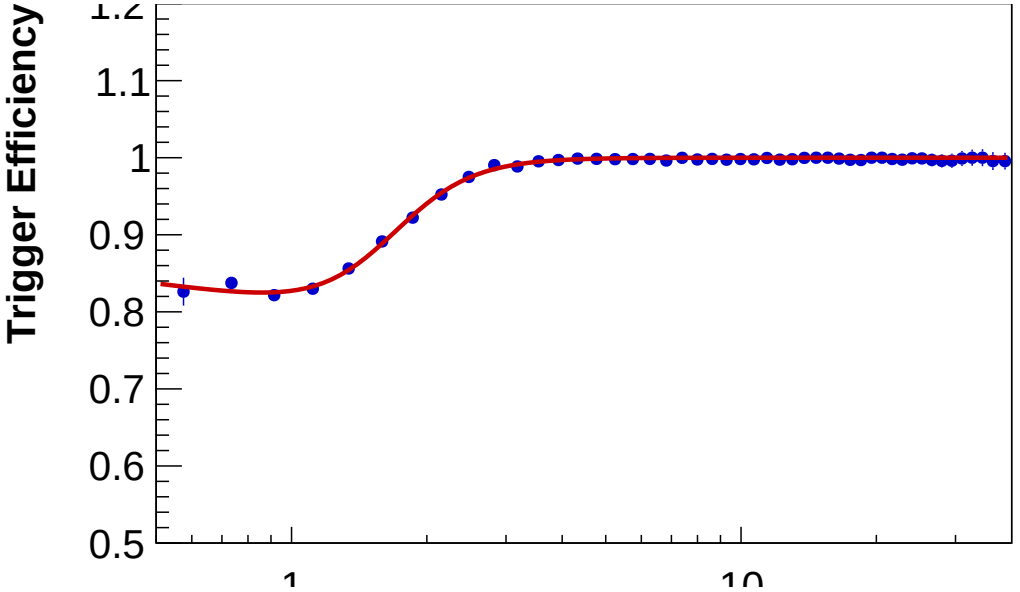

FIGURE 3.25: Trigger efficiency as a function of energy evaluated from DATA as *last cut*.

Chapter 4

Electron and positron identification with AMS

The identification of electrons and positrons in the primary cosmic rays flux is very challenging. The signal should be extracted from a huge background constituted mainly by protons ($\sim 90\%$ of background) and nuclei. In this chapter, the technique applied to obtained the number of $e^{\pm}$ with the AMS detector will be discussed.

The key AMS sub-detectors used in the $e^{\pm}$ analysis are the electromagnetic calorimeter and the TRD. Both give an high e/p separation power and the calorimeter perform the measurement of the $e^{\pm}$ energy with very high accuracy. Also the informations coming from the other sub-detector are combined with the signal from ECAL and TRD in order to completely identify the particles. For example, the sign of the rigidity measured by the tracker is used to distinguish between e^{+} and e^{-} and the direction of the particle given by the ToF is used to distinguish between up-going and down-going particles.

4.1 Sample definition

The first $\sim$30 months of data taken by the AMS on ISS (19 May 2011 - 30 Nov 2013) have been analyzed. First of all, a preselection has been applied in order to reject the events that are not useful for a $e^{\pm}$ analysis and in order to defined a clean sample of unitary charge from which extract the signal. At the end of this preselection, the sample will contain mainly protons and a low fraction of $e^{\pm}$ (e/p$\sim$1%–10%

depends on energy). From the preselected sample, the signal has been statistically separated from proton background through a template fit on TRD distribution. For the definition of the electrons and proton template, the variables reconstructed by the ECAL have been used.

The amount of events taken during the period in which the analysis has been performed, is 4×10^{10}. Due to some problems related to the acquisition of data or some problems that can derive from the geometrical acceptance of the detector, not all the events are good for the analysis. For this reason before the rejection of the background through the template fit method, a preselection has been applied over the all taken events. This preselection contains a minimal set of cuts with high efficiency over the $e^{\pm}$ and which purpose is to select a clean sample of unitary charge down-going relativistic particle.

The preselection cuts, can be divided into four categories, according to the criteria with which were applied:

a Good data taking: First of all, it should be assured that the events used for the analysis are without any problems during the DAQ and that they have been taken in a nominal conditions.

b Geometric selection and clean event reconstruction: It is not possible to have for each event coherent informations coming from the various sub–detectors. This is mainly due to a geometric acceptance problem and to interactions of the events with the material of AMS. Only events that satisfy some geometrical requests and for whom it is possible to have some fundamental and mutually consistent informations coming from the various detectors have been taken into account.

c Unitary charge particle Since the signal in this analysis is constituted by $e^{\pm}$, the events with a reconstructed charge greater than one are rejected.

d Above cut-off in order to take only primary cosmic rays and not take into account the secondary particles trapped in the geomagnetic field, the events under cut-off have been not taken into account.

4.1.1 Good data taking

Since AMS is installed on ISS, it is not a free orbiting satellite. The orbit parameters cannot be decided and moreover the AMS field of view can be affected by the ISS operations. This first part of preselection regards only parameters related to the data acquisition and to the position of AMS. It doesn't take into account problems coming from the reconstruction of the events informations that cross the detector. All the informations regarding the orbit and DAQ parameter are stored every second in the RTI (Real Time Information). This tool has been used for the selection of events taken in a good conditions.

First of all, if some errors have occurred in the hardware or if DAQ failures have arisen, the events are rejected. Also the events in which raw data block are missing because of an unexpected loss of signal from ISS to ground, have been removed. Figure 4.1 shows the total time of AMS in orbit compared with the time during which the DAQ has acquired and the time during which the DAQ has acquired without any problems.

For the rate is requested to not exceed a maximum value ($1800\,Hz$) in order to have an efficient DAQ, and only events with *livetime*> 0.4 have been selected. As

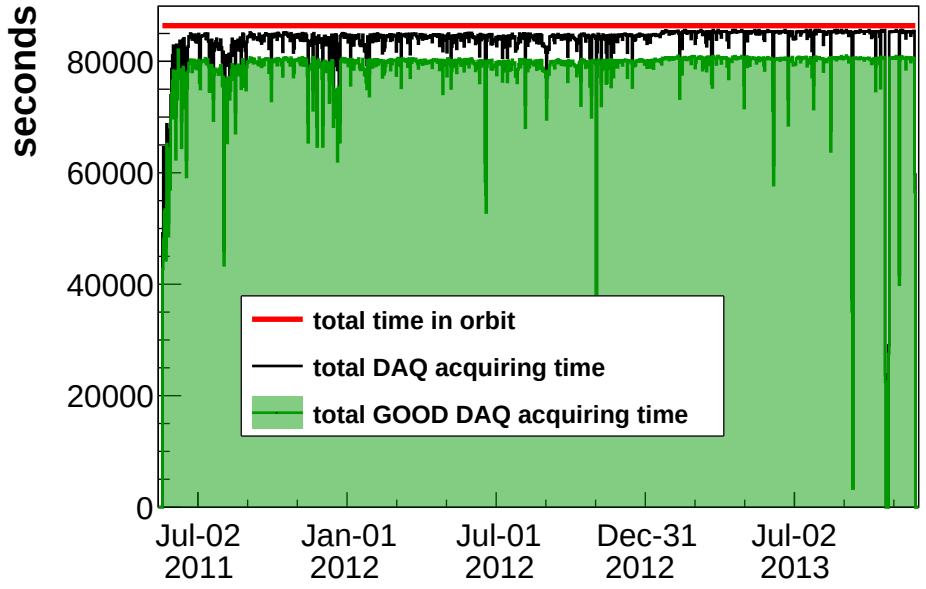

FIGURE 4.1: Seconds as a function of time during which AMS is in orbit (red line), DAQ was acquiring (black line) and DAQ was acquiring without any problems (green line).

shown in figure 4.2 this cut automatically removes the events taken when the ISS is over the SAA[1]. It is also important assure that the events to be analyzed were not taken when the material of ISS (like for example a solar panel) intercept the field of view of AMS. Moreover, due to special ISS operations like a docking/undocking of a Soyuz, the AMS can be tilted respect to the zenith angle. Since the field of view of AMS is $\sim 40^o$ the events taken with a deviation from the zenith angle greater then 40^o have been rejected.

The run that are not good for the analysis (test, TRD gas refill, etc..) have been removed.

This part of preselection is important to assure that the data on which the analysis is performed are not affected by DAQ or hardware problems and has an efficiency of 90 % over all the data acquired by AMS.

4.1.2 Geometrical selection and clean event reconstruction

The request to have no problems during the acquisition, is not enough in order to have a sample of events useful for the analysis. It is not possible for all the events

[1]SAA = South Atlantic Anomaly

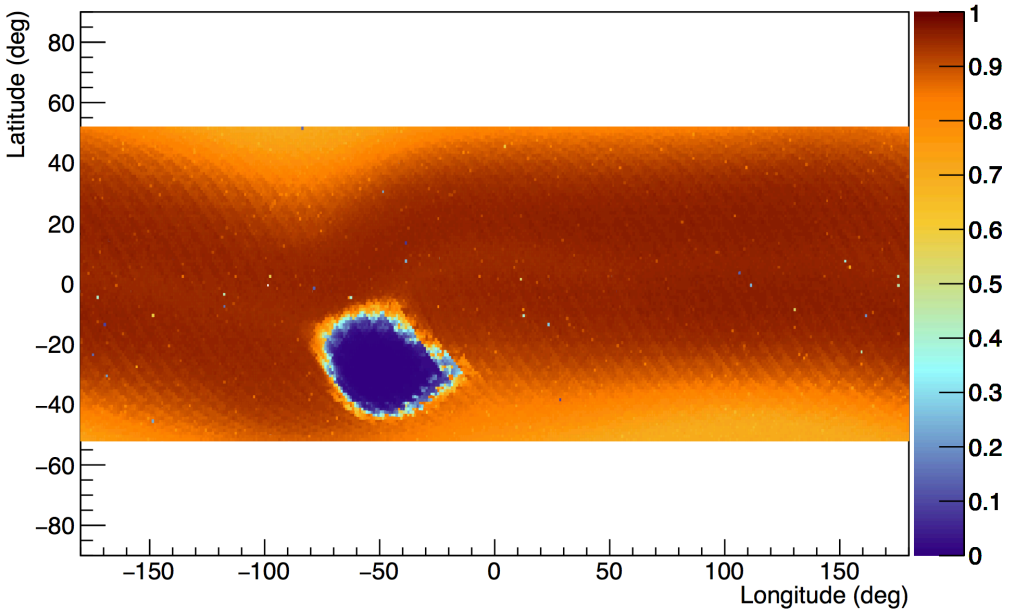

FIGURE 4.2: Value of AMS livetime as a function of the ISS orbit position in geographical coordinates. The request*livetime*> 0.4 automatically removes the events taken when the ISS is over the SAA.

to reconstruct clear and univocal informations. For one single event, two or more different particles can be reconstructed by the detector. This can be due to the presence of secondary particles produced by the cosmic rays interaction with AMS material or can be due to the *pile-up* effect (i.e. when two cosmic rays are triggered together). Moreover without no cosmic ray that crosses the detector, the trigger may nevertheless give a signal due to the intrinsic noise of the electronics. In order to have a clean event reconstruction, the kind of events described above should be removed.
The sample to analyze can be further reduced without any loss of good electrons, applying some geometrical cuts. The purpose of these cuts is to obtain only events in which the informations coming from the various sub-detector are matching to each other. Moreover, all the events that are not geometrically contained in the interested volume for a $e^{\pm}$ analysis (for example, the events outside the calorimeter) should be rejected.

The first request that has been applied in this part of preselection is the presence of a physic trigger (see 3.6). As will be shown, this cut has an efficiency of 100% for energies above 3 GeV that decreases up to ∼70% for lower energies.

For each sub-detector the raw data are clustered together in order to build an high-level physic object (as example: `TRD track` for the TRD, `ToF Track` for the ToF, etc...). Some sub-detectors can be used in a standalone way: for example, the raw data taken just by the electromagnetic calorimeter can be clustered in order to build `ECAL Shower` object that contains all the information related to the reconstructed shower in the ECAL (energy, lateral dispersion, maxim, etc...). Others subdetectors, cannot be used in a standalone way. This is the case of the raw data collected by the tracker that need of some informations coming from the others sub detectors before to be collected in the `Tracker Track` object.

The high-level physics objects are combined into the most high level physics object: the `Particle`. The basic criteria to have a `Particle` defined for an event is the presence of the `ToF Track`. Since the energy used in the $e^{\pm}$ analysis is the one reconstructed by the ECAL, only events that have at least one `Particle` with an associated `ToF Track`, `Tracker Track` and `ECAL Shower` have been taken into account. Figure 4.3 shows the distribution for the number of reconstructed `Particle` objects for each event at different levels of preselection. For the events in which is present `Tracker Track`, `ToF Track` and `ECAL shower`, the percentage in which these object are associate to a `Particle` object is ∼40%.

The information coming from the `ToF Track` have been used to select *downgoing* and relativistic particles applying a cut on the value of reconstructed velocity $\beta = v/c$. The β is reconstructed using the time measured by the ToF and the know distance between the upper and lower ToF. For this reason the quantity $1/\beta$ follows a gaussian distribution and in the case of downgoing electrons is a gaussian which peak is ~ 1. The symmetric cut 0.8¡$1/\beta$¡1.2 has been applied. As shown in figure 4.4 this request assures that only downgoing particles are taken and moreover this cut has an e fficiency ∼100% on the electrons.

Further requests have been applied on `Tracker Track` and `ECAL shower` both of them associated to the `Particle` object.
First of all only events with the `Tracker Track` inside the ECAL fiducial volume are taken. This is a fundamental request in order to use a good reconstructed energy value. The particles that cross the border of ECAL, as Figure 4.5 shows, have a bad energy resolution. This is due to the lateral leakage of the shower and to the presence of the PMTs and read-out electronics. The bad resolution that can be observe around x_{ECAL}=∼18 cm is due to a dead PMT on layers 6 and 7.

The definition of the ECAL fiducial volume should be carefully defined. If only particles fully contained in ECAL are taken, the energy resolution improves but the ECAL acceptance is significantly reduced (as shown in **??**). In order to chose the

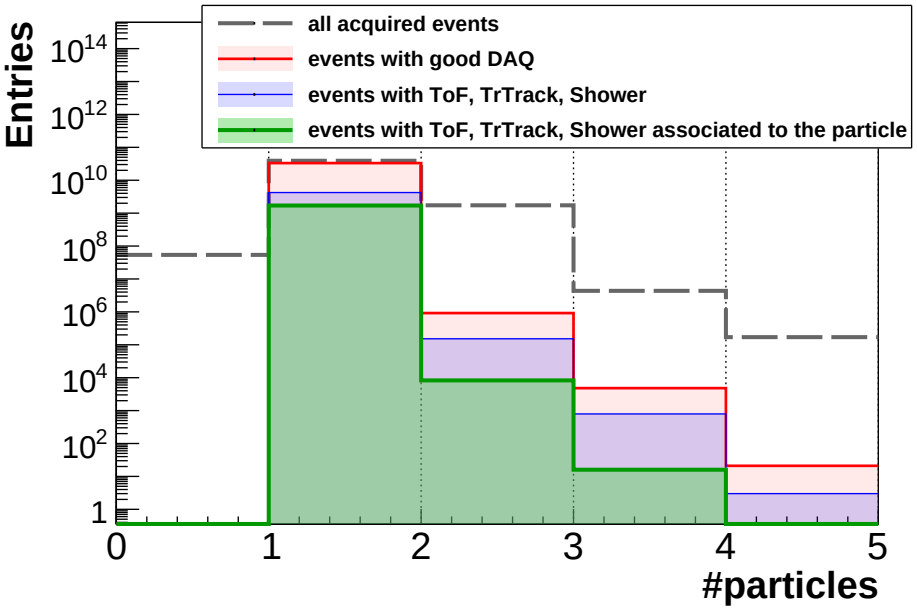

FIGURE 4.3: Number of reconstructed `Particle` objects for each event at different levels of preselection.

fiducial volume a good compromise between a good ECAL resolution and ECAL acceptance large enough should be found. The cut that has been applied is the following. Only `Tracker Tracks` that cross the top and the bottom of calorimeter inside 32.4 cm (both in x and y side) are taken. This cut removes all the border of the ECAL where is mounted the PMTs and the read-out electronics. Furthermore, also the `Tracker Tracks` that cross vertically the border of calorimeter (defined as x/y >31.4 cm) are removed, in this way the showers with a significant lateral leakage are removed.

Also the matching between the `Tracker Track` and `ECAL shower` has been checked. Figure 4.7, show the distance between the `Tracker Track` and the `ECAL shower` in x (Δx) and in y (Δy).

The distance has been calculated in the *Center of Gravity* of the shower. Both the distributions show larger tails at low energies, due to the multiple scattering effect but only (Δx) is a symmetric distribution. The (Δy) distribution has an asymmetric tail due to the bremsstrahlung effect. An electron (positron) that goes through the tracker, has an high probability to emit bremsstrahlung photons that follow the direction in which they are emitted and reach the ECAL starting an electromagnetic shower. The electron, after the emission of the photon, decreases its energy and the curvature of trajectory increase. As consequence, when the track reaches the calorimeter will be shifted respect to the shower axis. This effect is schematically represented in figure **??**. Only events with Δx <3.6 cm have been

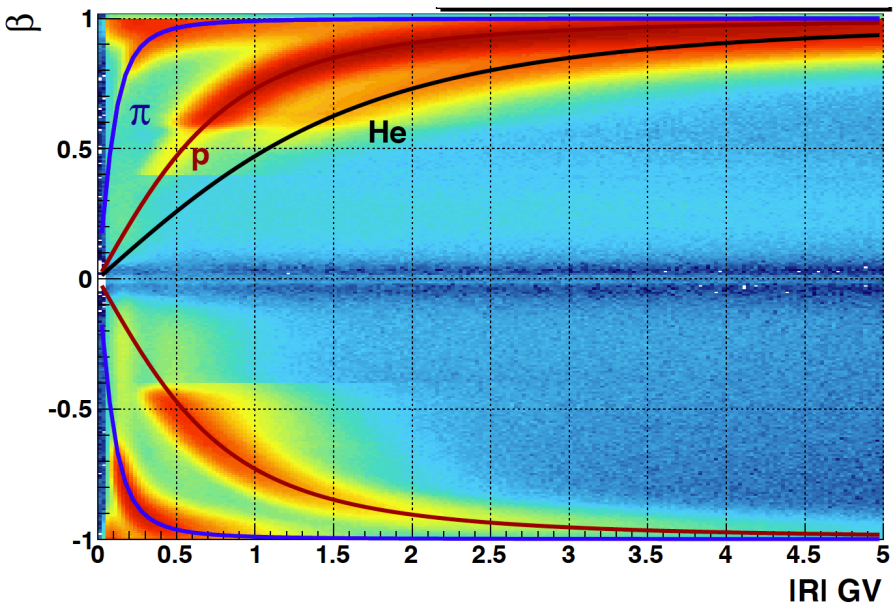

FIGURE 4.4: β measured by the ToF as a function of rigidity.

taken. Since the effect of bremmstrhalung should be taken into account the cut applied on Δy is larger and only events with Δy <7.2 cm have been taken.

A fundamental tool for the electrons and positrons analysis, is the TRD estimator built through the information coming from the different energy deposits per unit length for electrons and protons. The `Tracker Track` has been extrapolated inside the TRD volume and only the TRD hits that are along the `Tracker Track` are taken into account in building the TRD estimator. This contributes to reject the events with a wrong reconstruction of `Tracker Track` and the events that are affected by the multiple scattering. Moreover only the events with a minimum number of TRD hits are taken. This assures a good reconstruction of the TRD classification tools. Only the events with a number of TRD hits along `Tracker Track` > 9 have been taken. This cut has a total efficiency of 99.2 % and is less efficient at low energies as shown in Figure **??**.

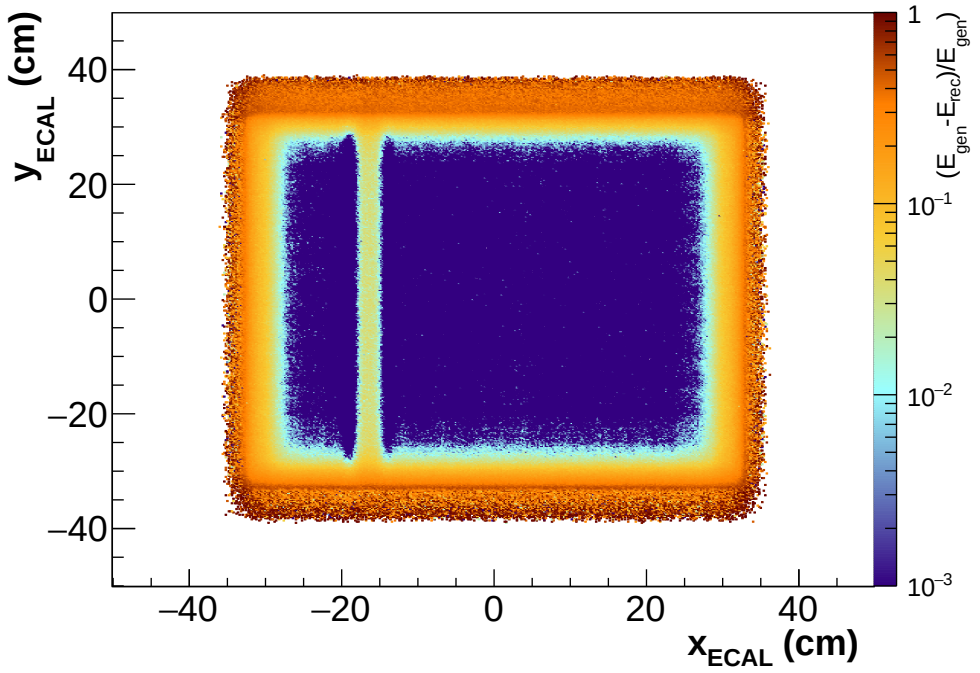

FIGURE 4.5: Energy resolution for different position on the first layer of ECAL of the crossing particle.

4.1.3 Unitary charge sample

At the end of the geometrical and clean sample selection, the sample contains only events with downgoing relativistic particles which have an associated `Tracker Track` and `Ecal Shower`. Moreover the `Tracker Track` of the particles is inside the TRD and ECAL volume and it is combined with `Ecal Shower`. However, the sample still contains CRs nuclei and secondary particles produced by the primary event through the interaction with AMS materials. The rejection of these kind of events is the purpose of this part of selection.

The charge reconstructed by the inner tracker (layers 2-8) using the energy deposit dE/dx in each layer was used in order to select the unitary charge particles. Only the events with the inner tracker charge (Z_{inn}) <1.5 have been taken. As will be discussed in details in section 5.1, the efficiency of this cut is high and doesn't represent a problem in the calculation of systematics. However it shows a slight decrease with the energy due to an asymmetric shape of Z_{inn} distribution for electrons sample where the energy starts to increase as shown in figures 4.9. The asymmetric tail is due to secondary particles produced before the inner tracker or due to Bremsstrahlung events. This behavior is confirmed also by MC simulation.

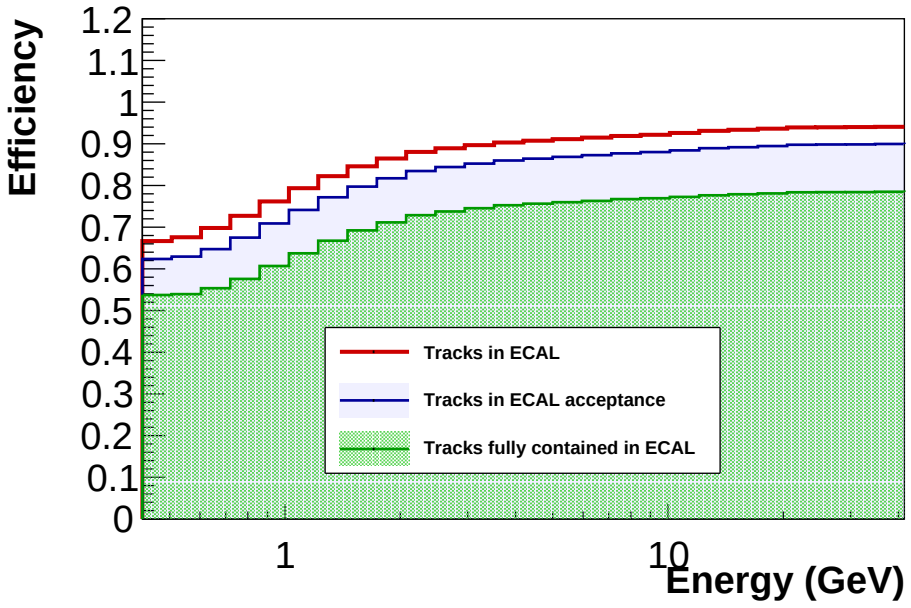

FIGURE 4.6: Efficiencies on electrons obtained for three different definition of ECAL fiducial volume.

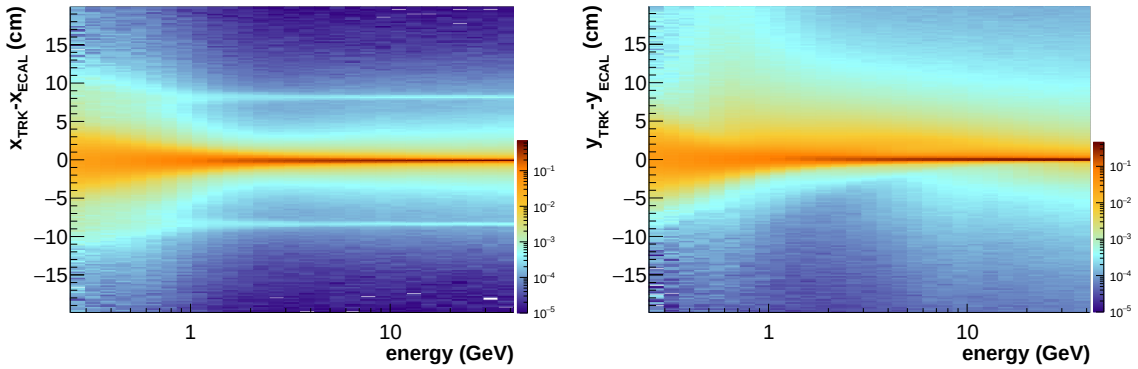

FIGURE 4.7: Distance between the `Tracker Track` and the `ECAL shower` in x (left) and y (right) calculated in the Center of Gravity of the shower.

AMS can provide a redundant charge measurement from the various sub-detectors. In figure 4.10 is shown the charge reconstructed through the energy deposition on the ToF paddles (Z_{ToF}) versus the charge obtained from del energy deposition on the inner tracker layers. However a cut on Z_{ToF} introduces one more cut in the systematic calculation without significantly remove the residual nuclei after the request (Z_{inn}) <1.5 since the resolution of (Z_{ToF}) is worst respect to (Z_{inn}).

Another tool used for the unitary charge selection, is the TRD. Thanks to the

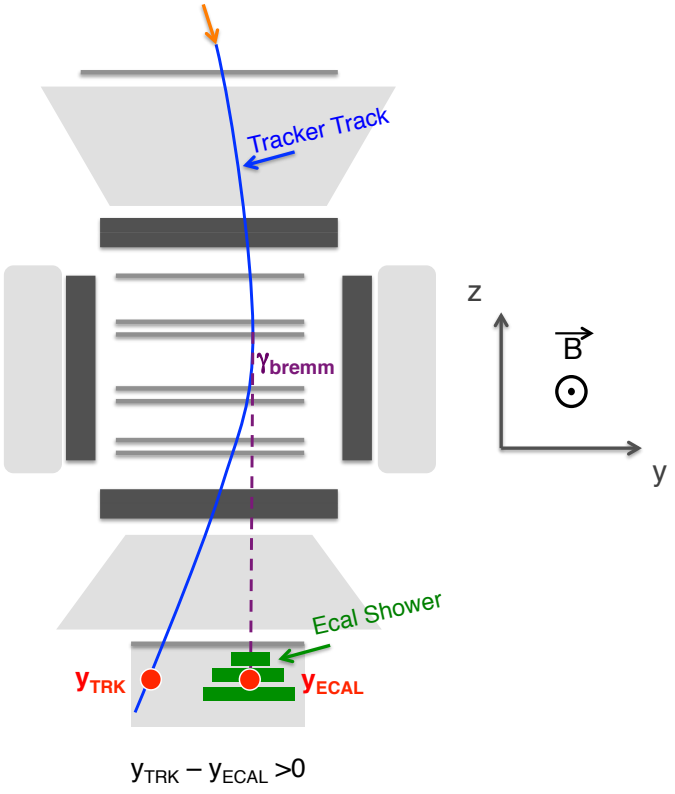

FIGURE 4.8: Bremmstrhalung effect on Δy for an electron.

different energy deposition in the various TRD layers between electrons and Helium, it is possible to build a TRD estimator to separate electrons from Helium (*TRD estimator e/He*). A cut of *TRD estimator e/He*<0.8 has been applied. This cut helps in removing Helium from the sample with an efficiency of $\sim 100\%$ over electrons: it doesn't enter in the systematic calculation.

More cuts should be applied in order to remove the number of the events interactions with the AMS material. The interactions produce secondary particles which introduce an high level of activity in the sub-detector electronics making hard the properly reconstruction of the informations related to the primary particle. Moreover, the interactions can introduce unwanted correlations between the various subdetectors: for example, high energy secondaries produced in the TRD can be clustered as primaries in ECAL.
The interaction events can be individuate by mean of the energy deposits on ToF paddles looking if the deposited energy is greater than the one for the single particles. Or is it possible to defined the *number of the interactions* using both the information coming from the ACC both from the ToF. In general, a big number of interactions correspond to an high ACC value but this is true also in case of backsplash events. In order to distinguish between the two cases it is possible to use the time information coming from ToF and ACC as described in figure 4.11. However a

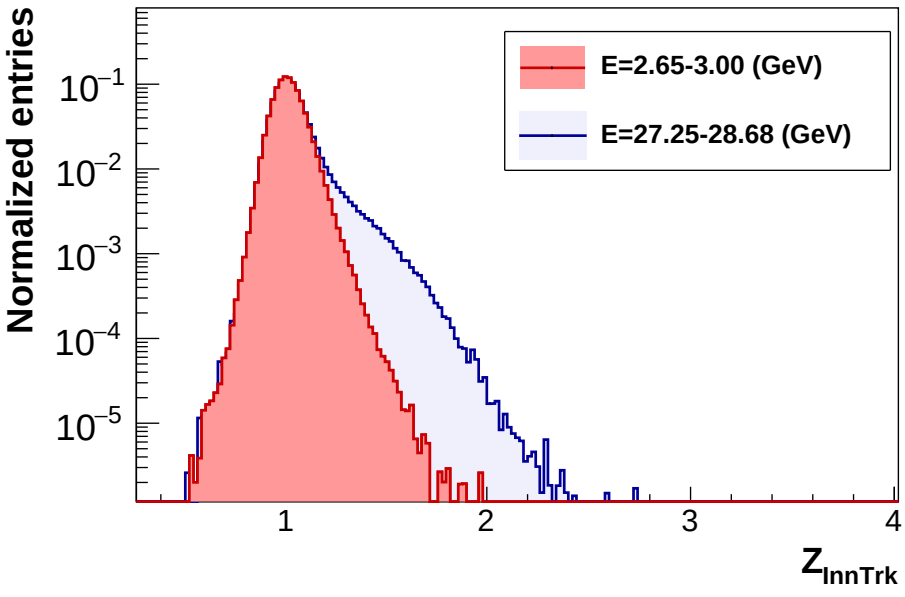

FIGURE 4.9: Distribution of charge reconstructed using the energy deposit on the Inner tracker Layers (Z_{InnTrk}) for 2 different energy bin. The distribution starts to become asymmetric with the increase of energy.

cut based on the number of ACC or on ToF energy deposits is not so efficient on an electrons sample and moreover the MC data are not able to satisfactorily simulate the ACC and ToF responses as show in figure 4.12.

The number of interactions seems to be related to the number of reconstructed tracks as shown in figure 4.13. Only the events with a number of reconstructed `Tracker Track` equal to one have been taken into account. This cut helps to remove the interacting events, has an efficiency of $\sim 90\%$ and doesn't depend by energy. Moreover this request helps to reduced the *irreducible background*. A typical event that constitutes this kind of background is shown in figure 4.14: the primary particle is a proton that interacts in the first part of the TRD and produces a secondary high energetic electron. Both the signal in TRD and ECAL are associated to the secondary electron that will be reconstructed as the primary particle. The effect of this *irreducible background* has been studied over a MC protons sample and it is negligible especially over a single `Tracker Track` sample.

In order to reduced the charge confusion (cc), more requests have been applied on the `Tracker Track`. Only the events which tracker pattern contains also layer 2 have been taken. Figure 4.15 shows the cc as a function of energy evaluated from MC electrons and defined as the ratio between the events with the wrong

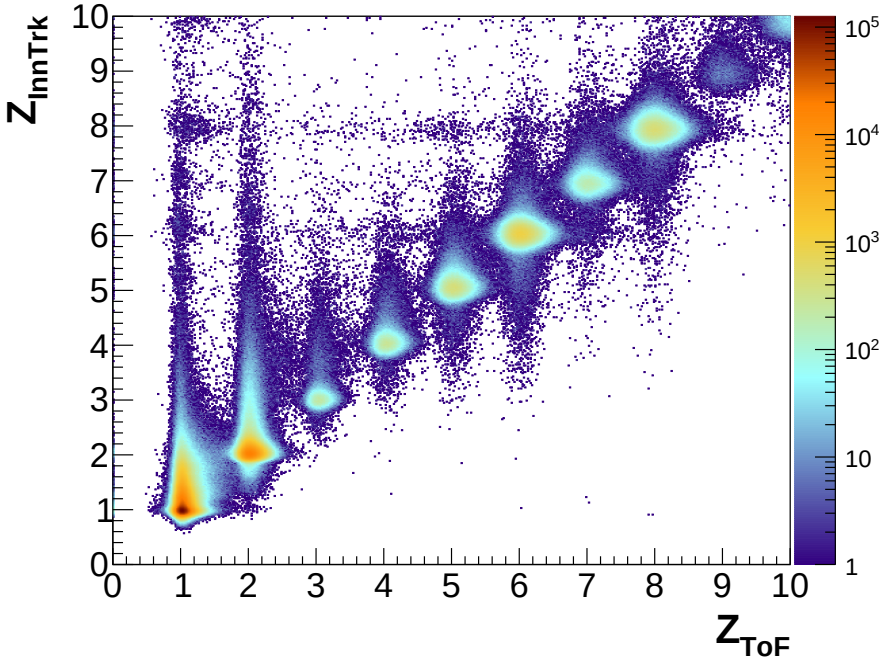

FIGURE 4.10: Charge measured by the Inner Tracker (Z_{InnTrk}) versus the charge measured using the energy deposition on ToF paddles.

reconstructed rigidity sign (R¿0) and all electrons. The cc in a sample which tracker pattern contains also layer 2 is $\sim 50\%$ less respect the one in a sample with the all Tracker patterns. This cut helps in having a good Tracker reconstruction without the introduction of a significant systematic.

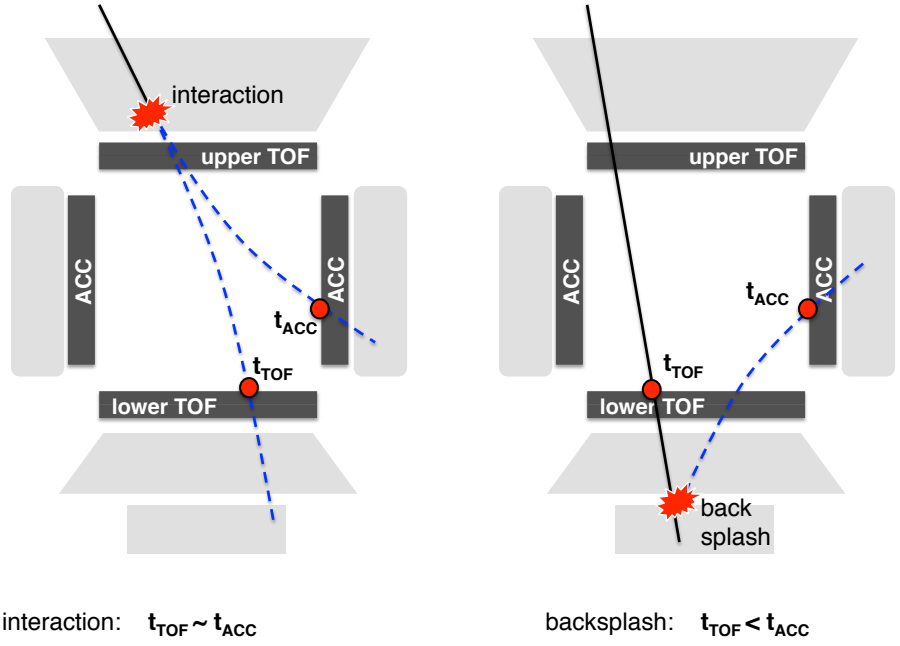

FIGURE 4.11: The time detection of ToF and ACC can be used in order to separate between the interaction events and back-splash events.

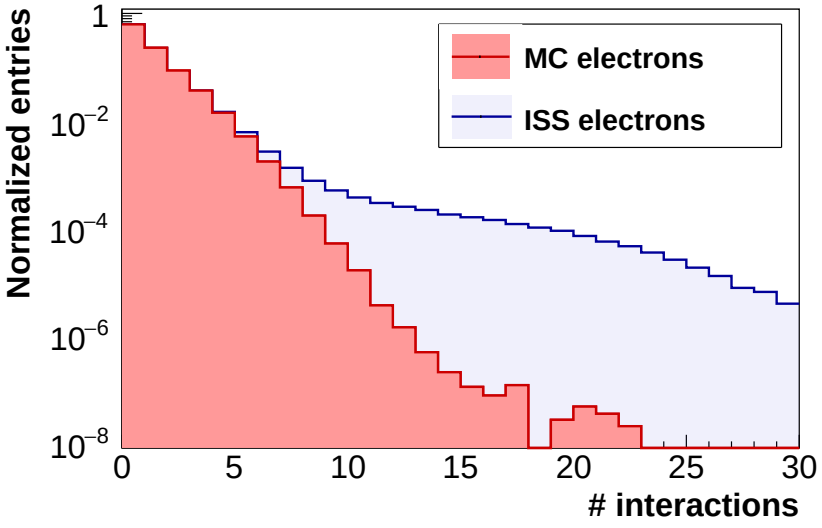

FIGURE 4.12: The distributions of the number of interactions (# interactions) between electrons selected from DATA and MC electrons are not in agreement.

4.1.4 Above cut-off

The last request that have been applied has the scope to select only primary particle. A fraction of the events that cross AMS are secondary particle trapped in the geomagnetic field. In order to reject those kind of particles, a cut over the energy of the particles compared with the value of the Støermer Rigidity Cutoff ($R^{\pm}_{cutoff}(\theta,\phi)$). $R^{\pm}_{cutoff}(\theta,\phi)$ is calculated assuming positive and negative charged particle using equation 1.16 as a function of the geomagnetic galactic altitude and azimuthal angles θ^{gal}, ϕ^{gal} and then transformed in the AMS reference frame direction θ, ϕ. For the cut, has been used the Maximum Rigidity cutoff $R^{40^o}_{max}$ calculated as the maximum value of $R^{\pm}_{cutoff}(\theta,\phi)$ for positive and negative particle in the whole AMS field of view, conservatively assumed to be 40^o:

$$R^{40^o}_{max} = max\{R^{+}_{cutoff}(\theta,\phi), R^{-}_{cutoff}\}, \qquad \theta,\phi \in \Omega^{AMS_{FoV}}_{40^o} \tag{4.1}$$

Where $\Omega^{AMS_{FoV}}_{40^o}$ is the domain of θ and ϕ for the AMS filed of view.

The figure 4.16 shows the $R^{40^o}_{max}$ for the various value ISS geographic latitude and longitude. The value goes from few GV (at the pole) up to $\sim$ 30 GV (at the equator). In order to select only primary particle, for each events belonging to the energy interval $[E_{min}, E_{max}]$ only the events with the E_{min} $1.2 \cdot R^{40^o}_{max}$ have been selected. The requirement has been applied over the minimum value of energy to

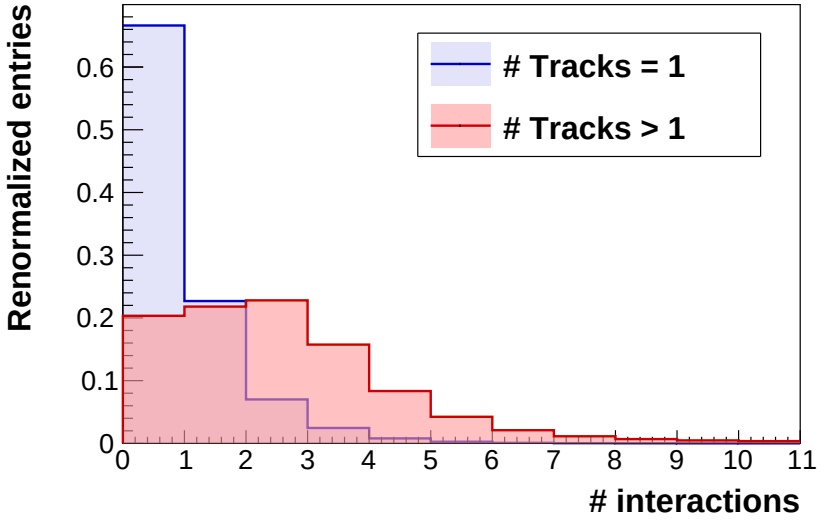

FIGURE 4.13: Number of interactions in a single track sample (# Tracks=1) and in a multi Tracks sample (# Tracks¿1).

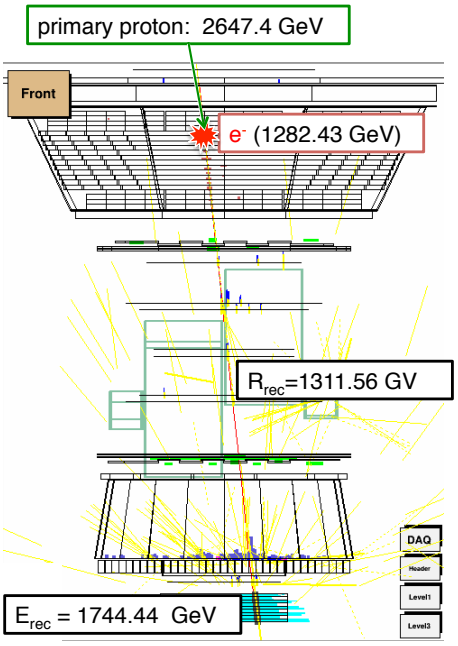

FIGURE 4.14: A typical event of proton (from MC) that constitute an irreducible background.

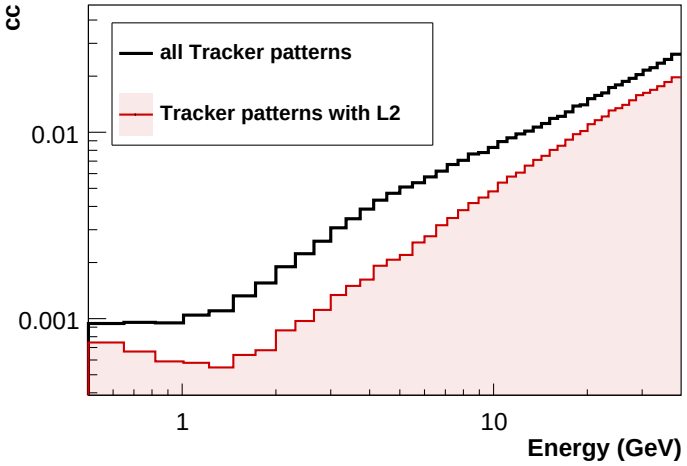

FIGURE 4.15: Charge confusion (cc) as a function of energy estimated from MC electrons, for a electron sample without any request on the Tracker pattern (black line) and for an electron sample which Tracker pattern has layer 2 (red and filled line). cc has been defined as the ratio between electrons with wrong reconstructed rigidity sign (R¿0) and all electrons.

be consistent with the evaluation of the exposure time (see section 3.5). The factor 1.2 has been added in order to have a conservative cut, since the value value of $R_{max}^{40^o}$ has uncertainties due to the geomagnetic model used. As shown in figure 4.17, the efficiency of this cut is $\sim 10\%$. However the inefficiency is dominated mostly by the protons component of the cosmic rays, since the cut energy used for the cut, is the one measured by the ECAL and it is smaller than the true protons energy. Most of

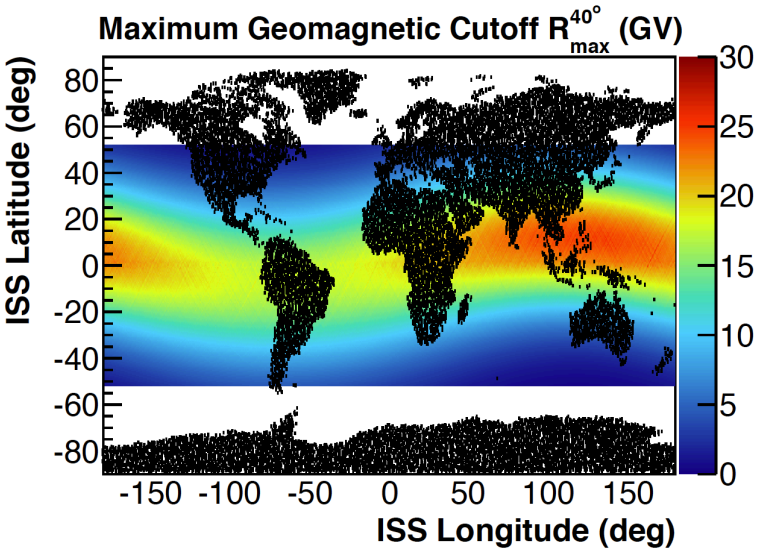

FIGURE 4.16: Maximum geomagnetic cutoff as a function of the ISS orbit position in geographical coordinates.

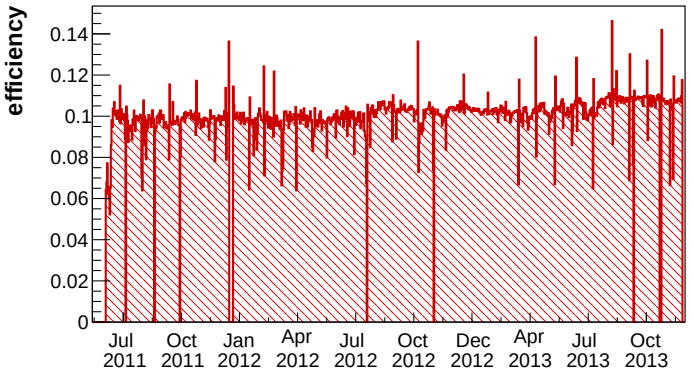

FIGURE 4.17: Efficiency of the cutoff request as a function of time.

the protons over cutoff are rejected by the cut E_{min} $1.2 \cdot R^{40^o}_{max}$. For $e^{\pm}$ component, the efficiency of the cutoff request is $\sim 100\%$.

4.1.5 Conclusion about preselection

The preselection has been applied over a total of 4.09×10^{10} events taken by AMS. The number of events that have been selected is 1.14×10^{8}, the correspond at $\sim 0.3\%$ of the initial sample, as shown in figure 4.18. The final sample consist in good reconstructed events of downgoing relativistic charge one particle. All the cuts applied in the preselection have an high efficiency over $e^{\pm}$ particles.

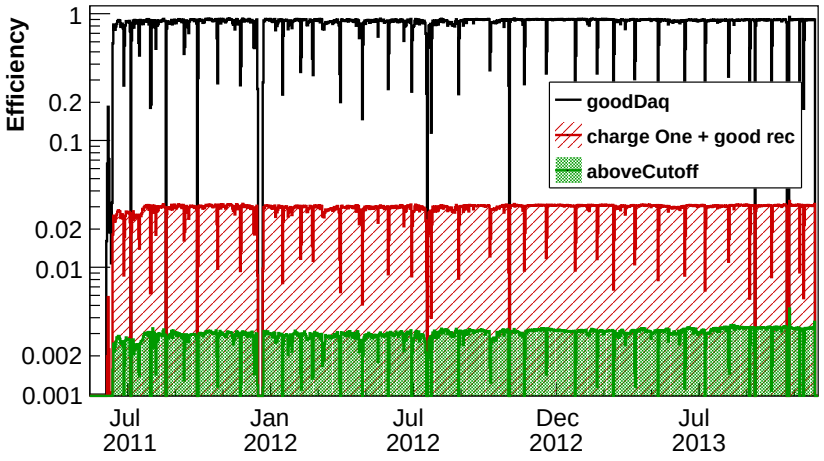

FIGURE 4.18: Efficiency of the pre selection at different levels: after the request to have good DAQ(black line), adding the request to have a sample of unitary charge events and good reconstructed (red line) and adding the request to have events above cutoff (green line).

4.2 ECAL,TRD and TRACKER in e^+, e^- measurement

The sample obtained at the end of the preselection is mainly constituted by protons, that compose the *background* that has to been removed, and contains a little percentages of *signal*, constituted by e^+ and e^-. It also contains a negligible amount of anti-protons.

In order to extract the *signal* from the overwhelming protons *background*, ECAL and TRD detectors responses have been used.
Using a deep knowledge of the different responses release by the *signal* and by the *background* both in ECAL and TRD, it is possible to reach a very high e/p rejection power. Since ECAL and TRD are uncorrelated, it is possible select a sample for the *signal* and *background* with ECAL in order to study the response in TRD and viceversa. Since the major part of the selected sample, is constituted by protons, is quite simple to obtain a *background* sample in order to study the response of the sub/detectors. The request to have positive charge sign is enough. Anyway it is possible obtained an high purity even for the *signal* sample, by mean of a strong cut on the ECAL variables (or TRD variables) and asking for negative charge sign (i.e. negative rigidity). This assure a deep and accurate study of ECAL and TRD

detectors, without using MC data which would introduce systematic errors to take into accounts.

In order to distinguish between e^+ and e^-, the sign of charge should be known with very high accuracy. The sign of the rigidity measured by the Tracker has been used to identify the charge sign taking into account the *charge confusion* problem as will be discuss in the section 4.2.3.

4.2.1 e\p separation with ECAL

The signal released in a calorimeter, is quite different for $e^{\pm}$ and protons [75]. When an electron (or a positron) reaches the first layer of ECAL, starts to emit photons due to the bremmstralungh effect. Then the photon produces an electron-positron pair through the interaction with the atomic nuclei of the material. The secondary $e^{\pm}$ produced, again emits photons for the bremmstralhung effect. These two process (bremsstrahlung and pair-production) continue until photons fall below the pair production threshold, and energy losses of electrons due to ionization start to dominate over the losses due to bremsstrahlung. What it is produced it is the so called *electromagnetic shower*. The parametrization of the electromagnetic showers in a sampling calorimeter is well know [76] When a proton reaches the calorimeter, the situation is quite different. Since the the nuclear radiation length of ECAL is 0.6λ, the 50% of the protons go through the whole calorimeter losing their energy only trough the ionization process. These kind of protons are called MIP ("minimum ionizing particles") and the energy that they depose in the calorimeter is very low ($\sim$200-400 MeV).

Remove the *background* constituted by MIP protons, is trivial.

The problematic *background* is due by protons that give a shower in the calorimeter. The *hadronic shower* has very different characteristics respect to the *electromagnetic* one. The hadronic showering process is dominated by a succession of inelastic hadronic interactions. At high energy, these are characterized by multiparticle production (mostly charge pions and nucleons) and particle emission originating from nuclear decay of excited nuclei. Due to the generation of π^0 that decay into $\gamma\gamma$, there is also an electromagnetic component present in hadronic showers.

Thank to the 3D reconstruction of the shower performed by ECAL, is it possible to exploit the different characteristic between *electromagnetic* and *hadronic* showers. The variables useful for distinguishing between *signal* and *background* (like the transverse and longitudinal shower development, the shower maximum, ecc...) are combined into a MultiVariate Approach (MVA), in particular, into a Boosted Decision Tree (BDT) [77], in order to maximize the rejection power of the calorimeter.

The BDT has been trained on electrons and proton samples selected from ISS data, without using MC. Thanks to a strong selection on TRD variables (as will be shown in section 4.2.2 and to the selection of the charge sign reconstructed by Tracker, it is possible to have electrons and protons samples clean enough to tune the BDT.

The classification tool used in this analysis, $ECAL_{BDT}$, relies on a total of 22 variables describing the longitudinal shower development and 39 variables describing the lateral shower development. The variables have been renormalized in order to remove their energy dependence, as described in [78]. The $ECAL_{BDT}$ has been trained in 14 separate energy bins, the last one starting at ∼250 GeV, in order to locally maximize the e
p separation.

Figure 4.19 shows the distribution of BDT as a function of energy for an electrons sample (left) and for a protons sample (right) and figure 4.20 shows the BDT distribution in one energy bin (E=15.14–16.05 GeV). In the case of electrons, the BDT shows a major peak for value 0. This is not true for the protons sample that show different populations according to the starting point of the shower. The most "dangerous" protons are the ones that start the shower quite early in ECAL since they have an high probability to be tagged as electrons by the BDT.

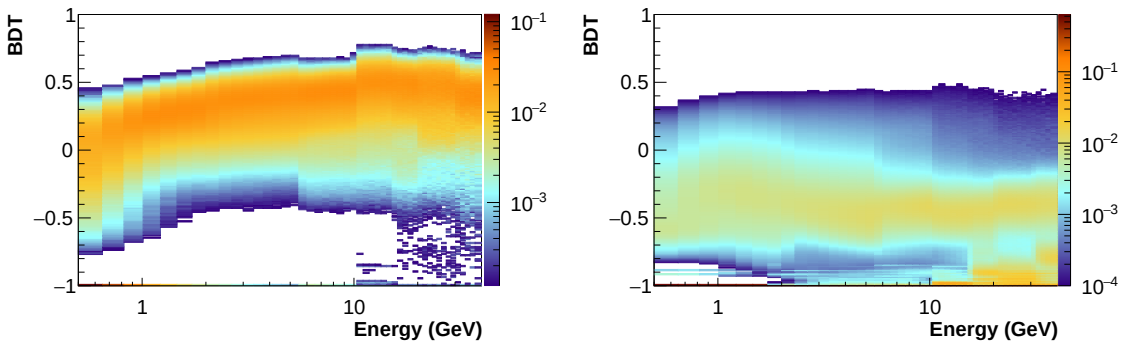

FIGURE 4.19: Distribution of BDT as a function of energy for an electrons sample (left) and for a protons sample (right).

Figures 4.21 and4.22 show the typical signal release in the AMS calorimeter by an electron, a MIP protons, a early showering proton and a deep showering proton.

4.2.2 e\p separation with TRD

The Transition radiation (TR) is the process where a charged particle emits soft x-rays in the crossing of a boundary between two media with different dielectric constants. The TR is emitted collinear to the primary particle's trajectory, and the amount of radiation emitted is proportional to the *Lorentz boost* γ and thus inversely proportional to that same particle's rest mass. This dependence is the key for the e/p separation performed by the TRD: since the proton mass is 1836 times the one for electron, a proton with kinetic energy 1TeV is like a 0.5 GeV electron in terms of transition radiation. Up to 300 GeV, electrons and positrons have a much higher probability of emitting transition radiation photons than protons. This difference in signal between protons and electrons is used to reach an high e/p rejection power through the TRD.

However, the signal of TRD has a strong dependence from the temperature gradients throughout the detector due to the environments conditions [79]. The gas contained in the straw tube (mixture of 90:10 of Xe and CO_2) continuously diffuses out of the

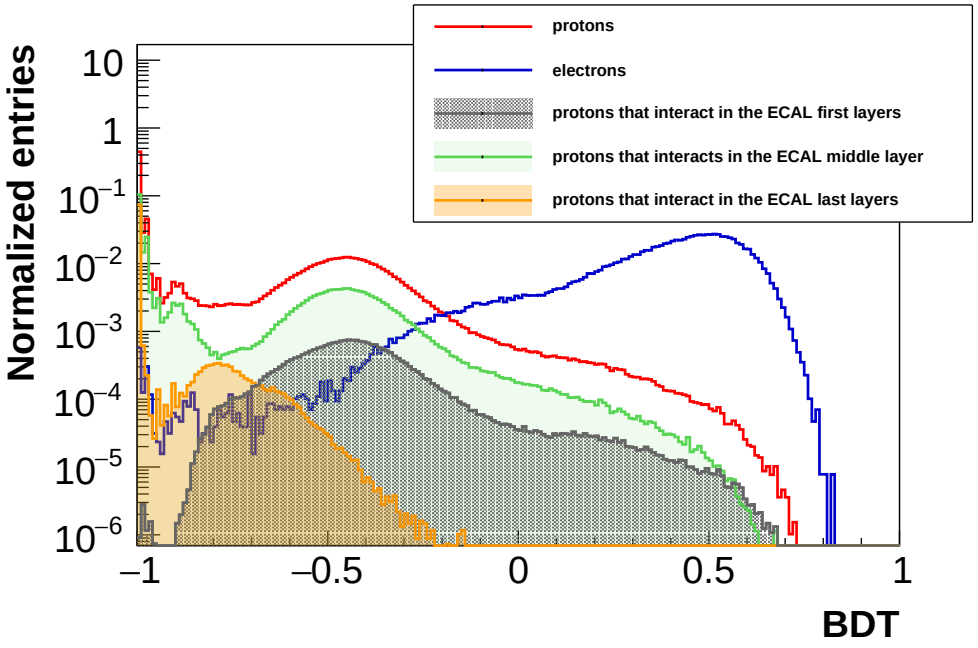

FIGURE 4.20: BDT distribution in one energy bin (E=15.14–16.05 GeV) for an electrons sample and protons samples that interact in different ECAL layers.

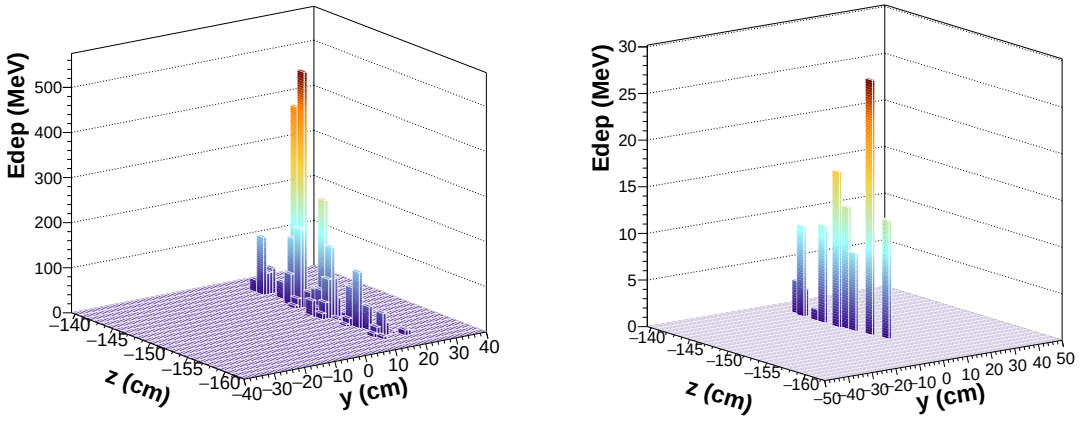

FIGURE 4.21: Left: Signal releases by an electron in the calorimeter. Right: Signal releases by a no-interacting proton in the calorimeter.

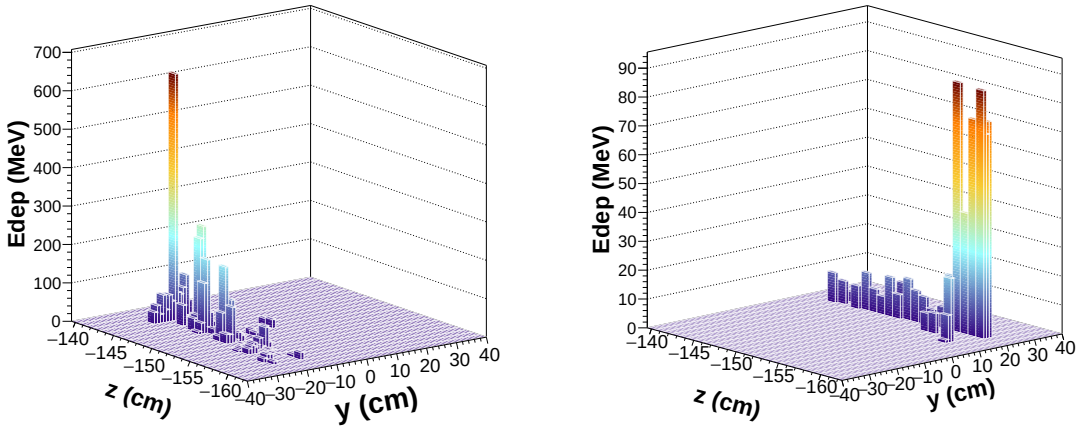

FIGURE 4.22: Signal releases by a proton that interact in the first layers of the calorimeter (left) and a proton that interact in the last layers of the calorimeter (right).

pressurized proportional tubes. This causes a increase in the gas gain and therefor an increase of the most probable value (MPV) of the energy deposited. For this reason, it is necessary to keep the gas mixture as stable as possible over time by means of two types of adjustments: high voltage adjustments (a decrease in high voltage will will decrease the signal amplitudes), and gas refills (which increase the pressure and modify the gas composition).

In order to perform these adjustments, a fast calibration is necessary. For this purpose a clean, single-track protons sample is used, since protons are the most abundant component ($\sim 90\%$) of the cosmic rays observed by AMS and they have a low probability to emit transition radiation, which allows in the calibration to use only the ionization signal. After applying the calibration, the detector response is

stable for all tubes within 2%.

Moreover the temperature variations gradients affect also the physical positioning of the proportional tubes, which results in systematic errors in physics analysis. A standard alignment method is therefore present in the official AMS software. This method extrapolates the tracker track (the best known estimation of the particle track) to each TRD tube, where the track position is compared to the default position of the tube wire.

In this analysis, the `TrdK TRD` reconstruction package [80], which provides calibration, alignment and particle identification tools, has been used.

The straw tubes of the TRD, are able to measure both the signal due to the ionization process, both the signal from the transition radiation. Figure **??** reports the signal in terms of ADC counts released in the TRD by a protons sample and by electrons sample (selected from ISS data by means of ECAL BDT and charge sign). In the protons sample is visible only the peak due to the dE/dx loss for ionization process. In the case of electrons, there is the peak due to the ionization process plus a secondary peak due to the TR. The information from the energy deposited in all the TRD 20 layers can be combined in a classifier that is able to discriminate between electrons and protons. Since the ionization loss and transition radiation depends on various quantities like particle momentum p, path length in the tube l and Xe pressure f_{X_e}, the classifier should take into account these dependencies. In order to build this classifier, two clean samples of protons and electrons selected from ISS data by means of ECAL and Tracker have been used to defined a parametrization of the *Probability Density Function* (PDF) $P_i^{e,p}(x|p,l,f_{X_e})$ for the ADC deposit x in the i^{th} layer and for the electrons e and proton p hypothesis.

The PDFs are used to defined the *TRD likelihood* for the single event:

$$L^{e,p} = \sqrt[n]{\prod_{i=1}^{N} P_i^{e,p}(x_i|p,l,f_{X_e}} \tag{4.2}$$

where n is the number of TRD layers with energy deposit above threshold.

For the analysis, has been used a combination of L_e and L_p in order to build a dedicated classifier for e/p separation, the $TRDlikelihoodratio$ (the same used in

the published positron fraction analysis [5]):

$$TRD_{lhr}^{e/p} = -log(\frac{L^e}{L^e + L^p}) \tag{4.3}$$

In the figure 4.23 are shown the distribution of the likelihood ratio as a function of energy for electrons and protons samples selected from ISS data and for MC electrons and the figure 4.24 show the likelihood ratio distribution for one energy bin for the electrons sample compared both with protons and with MC electrons. As can be see, the MC doesn't reproduce the data distribution for this reason it can't be used for the definition of the templates that will be used to fit the signal (see section **??**).

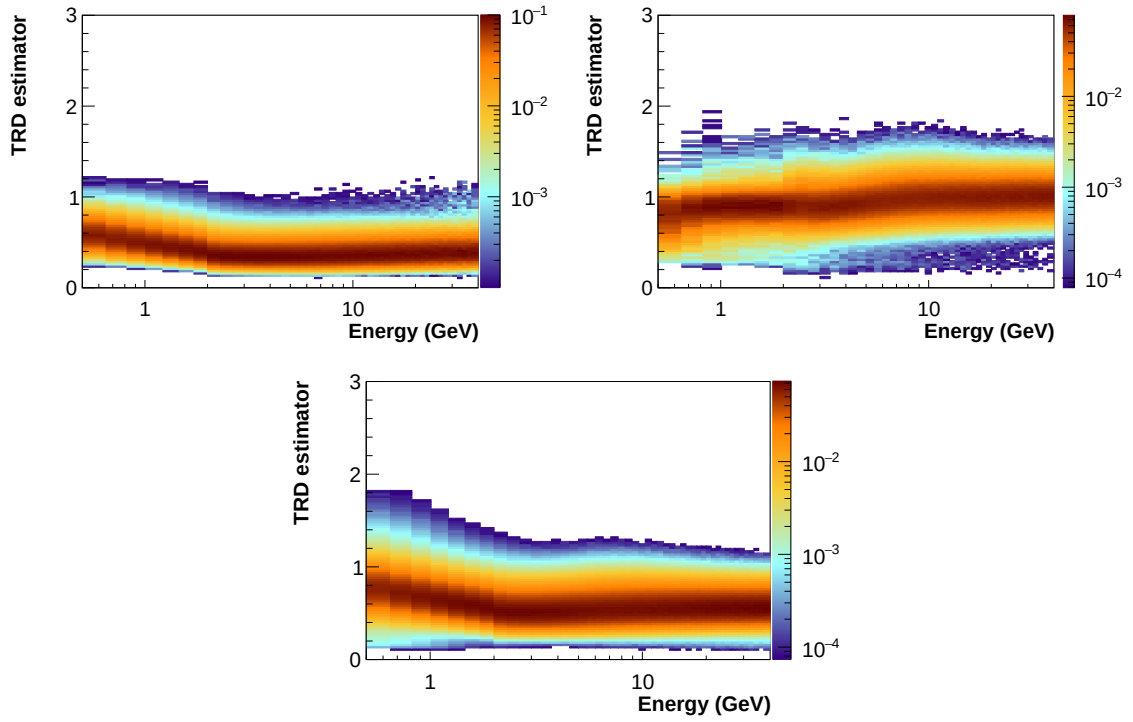

FIGURE 4.23: TRD electrons protons likelihood ratio distribution ($TRD_{lhr}^{e/p}$) as a function of energy for different samples: DATA electrons (top left), DATA protons (top right) and MC electrons(bottom).

4.2.3 Tracker role in e^+, e^- measurement

The Tracker plays a fundamental role in the measurement of e^+ and e^-. The sign of the reconstructed rigidity together with the information coming from the ToF (*downgoing* or *upgoing* particle) give the sign of the charge and the possibility to

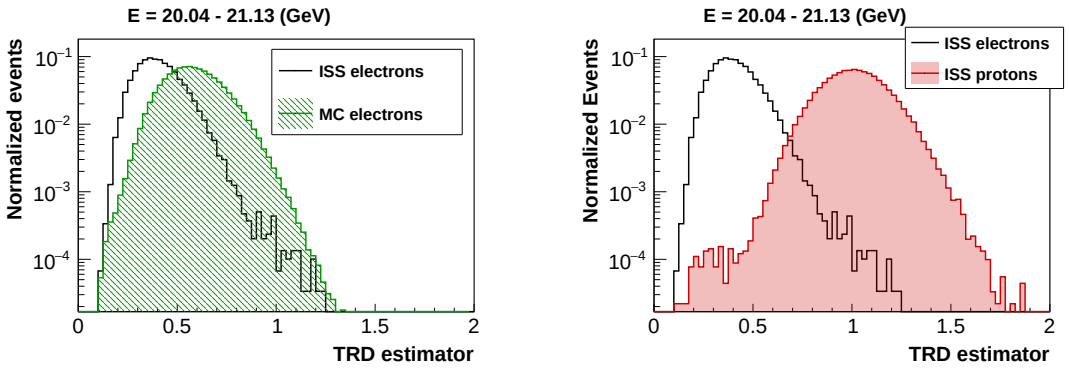

FIGURE 4.24: TRD electrons protons likelihood ratio distribution ($TRD_{lhr}^{e/p}$) for one energy bin (20.04–21.13 GeV) for DATA electrons (black line) compared with the same distribution for DATA protons (red filled line) and MC electrons (green filled line).

distinguish between e^+ and e^-. However, the effect of *charge confusion* (CC) should be taken into account in order to have the correct number of e^+ and e^-. Due to the CC a negative electron can be reconstructed as a positron and viceversa. This means that even for a background free e^+, e^- sample, the CC can spoil the electrons and positrons fluxes measurement.

The sources of CC are mainly two: the *spillover* and the *wrong hits* associated to the track [81].
The spillover is the dominant source of CC for high momentum particles: the curvature radius of the track inside the magnetic field increases with increasing particle momentum and, due to the finite measurement resolution of the trajectory, it becomes more probable to reconstruct the trajectory with a flipped curvature sign. At the MDR $\sim$ 16% of the particles are reconstructed with the wrong sign of the rigidity. This is a statistical effect and there's no way, except the comparison of the absolute energy or momentum of the particle given by an independent detector, to reduce the resulting CC. However, since the analysis for the fluxes in time, is focused on the low energy part (up to $\sim$40 GeV), the *spillover* doesn't represent the main source of CC.

At lower energies, the largest source of CC is related to spurious hits in the tracker - it is related to noise or interactions in the detector material - which are erroneously associated to the particle track in the pattern recognition, inducing a wrong reconstruction of its trajectory hence of its rigidity value and charge sign. This effect can be mitigated through the search for the effects of the interactions in the other sub detectors, once their topology in the instrument is known they can be either rejected or statistically subtracted based on their characteristics distributions.

As have been shown in section 4.1.3, the request to have a hit in layer 2 in the tracker pattern, helps in decreasing the charge confusion, but it is not enough. Up to $\sim 40\,\text{GeV}$, the effect of charge confusion can be negligible for the electrons but not for the positrons. If $\#e^{\pm}_{observed}$ are the numbers of observed electrons or positrons and $\#e^{\pm}_{true}$ are the real numbers of electrons or positrons, they are connected by the relations:

$$\begin{cases} \#e^{+}_{obs} = \#e^{+}_{true} \cdot (1 - cc) + \#e^{-}_{true} \cdot cc \\ \#e^{-}_{obs} = \#e^{-}_{true} \cdot (1 - cc) + \#e^{+}_{true} \cdot cc \end{cases} \tag{4.4}$$

The percentages of the wrong reconstructed numbers of $e^{\pm}$ ($\delta^{\pm}$) can be defined as follow:

$$\begin{cases} \delta^{+} = \frac{\#e^{+}_{true} - \#e^{+}_{obs}}{\#e^{+}_{true}} \\ \delta^{-} = \frac{\#e^{-}_{true} - \#e^{-}_{obs}}{\#e^{-}_{true}} \end{cases} \rightarrow \begin{cases} \delta^{+} = cc \cdot (1 - \frac{\#e^{-}_{true}}{\#e^{+}_{true}}) \\ \delta^{-} = cc \cdot (1 - \frac{\#e^{+}_{true}}{\#e^{-}_{true}}) \end{cases} \tag{4.5}$$

At $\sim 10\,\text{GeV}$, the cc evaluated from electrons MC and defined as the ratio between the number of the electrons reconstructed with the wrong charge sign and the total number of electrons (see figure 4.15) is ~ 0.005. In the same energy interval, the value of positron fraction is ~ 0.05 [5]. Substituting these value into the equation 4.6:

$$\begin{cases} \delta^{+} \sim 10\% \\ \delta^{-} \sim 0.5\% \end{cases} \tag{4.6}$$

In the case of positrons, the effect of charge confusion is not negligible and should be taken into account. The charge confusion is evaluated from MC electrons and the correct number of electrons and positrons are obtained from equation 4.4:

$$\begin{cases} \#e^{+}_{true} = \frac{\#e^{+}_{obs}(1-cc) - \#e^{-}_{obs} cc}{1-2cc} \\ \#e^{-}_{true} = \frac{\#e^{-}_{obs}(1-cc) - \#e^{+}_{obs} cc}{1-2cc} \end{cases} \tag{4.7}$$

The effect of the charge confusion correction can be appreciated in the case of positrons fraction in figure **??**.

The ratio between the ECAL energy E and the Rigidity measured by the Tracker R can be used as a powerful discriminating variable to increase the e/p rejection capabilities of AMS. As explained in 4.1.3 the electrons that go through the detector are subjected to the bremmstrhalung effect. Due to this phenomena, an electron can emit photons in the Tracker loosing its energy. Consequently the rigidity measured by the Tracker will be less than the true electron energy. However the ECAL is able to measure both the remain energy of electron, both the energy of photons that the

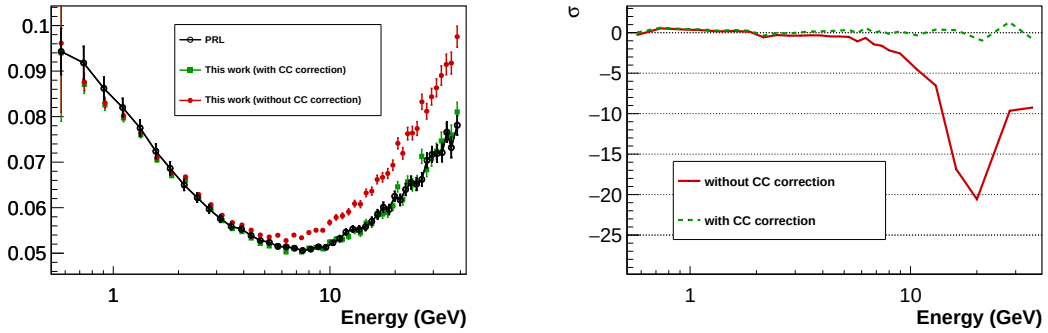

FIGURE 4.25: Result obtained with AMS data of positron fraction before (left) and after (right) cc correction.

electron has been loss in the Tracker with the result that the total energy measured by ECAL is near to the true value of the initial electrons energy. As result, the E/R ratio for electrons will be greater than 1.

Protons are not subjected to great energies losses due to bremmstrhalung effect so the rigidity measured by the tracker is quite similar to the true energy of initial protons. As explained in section 4.2.1 half part of protons arrived in the calorimeter as MIPs with the result that the measured energy is ∼0.4 GeV. The remains protons start an hadronic shower and the measured energy is in general $E \sim 0.5R$. As result the major part of protons will have E/R¡1. Figure **??** shows the distribution of E/R for an electrons and protons sample for one energy bin: the two peak around $E/R \sim 0.5$ and $E/R \sim 1$ can be clearly observed.

The distribution is not constant with the energy and the power of e/p separation of E/R decrease with energy as shown in figure **??**. However for the energy range considered in this work (0.5-40 GeV), E/R is still a powerful e/p discrimination variable.

4.3 Signal Extraction

In order to extract the signal constituted by e^- and e^+ the TRD likelihood e/p ratio ($TRD_{lhr}^{e/p}$), the Boost Decision Tree build with the information coming from the ECAL ($ECAL_{BDT}$), the E/R ratio and the Rigidity sign reconstructed by the Tracker have been used.

The analysis method used is the following:

- The signal has been extracted by means of a fit on the $TRD_{lhr}^{e/p}$ using the `RooFit` package [82, 83].
- The reference distributions (templates) used in the fit, have been defined using the $ECAL_{BDT}$, the E/R ratio and the sign of the charge.
- The electrons and the positrons have been separate using the information on the charge sign coming from the Tracker.

The method is similar to the one used for the all electrons flux measurement [47] with mainly two differences. First, the $ECAL_{BDT}$ is used only to defined the templates and not for the suppression of protons background in the sample to fit. For energies higher than $200\,GeV$, the overlapping between electrons and protons TRD templates increases with increasing energy, making hard the extraction of the signal. A cut over $ECAL_{BDT}$ with high efficiency on signal allows to reduce the systematic uncertainty in the evaluation of the $e^{\pm}$ component [84]. However the energy range analyzed in this work is up to 40 GeV and a cut on $ECAL_{BDT}$ is not needed.

Another difference with the all electrons analysis, is that the templates for signal and background are evaluated not only in each energy bin, but also as a function of time.

In this section will be describe the whole signal extraction procedure. The assessment of systematic uncertainties will be addressed in section 4.4.1.

4.3.1 Definition of TRD templates

?? As already discussed in section 4.2.2, the distributions of TRD_{lhr} for DATA and MC are not in agreement. For this reason, the reference distributions of TRD_{lhr} for signal and background are selected directly from DATA.

The templates have been selected applying a cut over the $ECAL_{BDT}$, E/R and the sign of the charge. These requirements assure an high purity for the templates.

However the shape of templates can depend from the selection applied. This dependence constitutes one of the major systematic uncertainty on the number of electrons and positrons counts obtained from the fit procedure as will be discussed in section **??**.

Figure **??** shows electrons and protons templates for two different energy bin and it shows that there is a strong dependence from the energy. This is also clear from figure ?? that shows the median[2] and RMS of the templates both for signal and protons as a function of the energy. For this reason, at least in the energy range in which the analysis has been performed (0.5-40 GeV), it is not possible use a*universal* reference distributions valid for all energies as it has be done for all electrons analysis, but the templates should be defined in each energy bin.

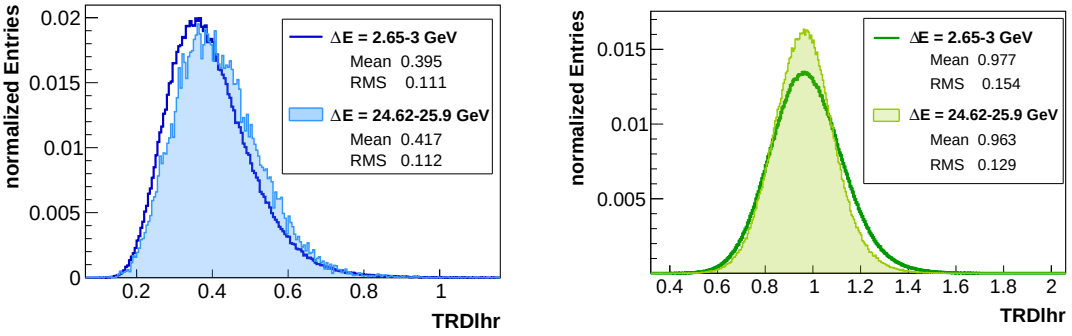

FIGURE 4.26: TRD_{lhr} distribution in two different energy bin for electrons (left) and protons (right) samples selected on DATA.

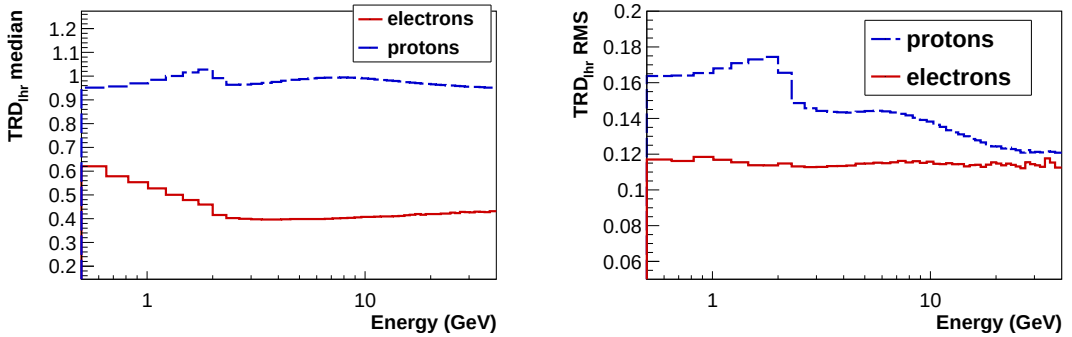

FIGURE 4.27: Median (left) and RMS (right) of TRD_{lhr} distribution as a function of energy for electrons and protons samples selected on DATA.

The same argument can be assessed for the time. Figure ?? shows the distributions for signal and background in two different time intervals of 27 days each, for a given energy bin. As in the case of the energy, the shape of the templates in two different time bin, are different. This is more clear in figure ?? that shows the median and the RMS of the templates as a function of time, in a given energy bin. The change in time in the TRD signal is expected and it is due both to the operation

[2]The median has been chosen instead of the mean of the distribution, because is the quantity more indicative of the peak of the distribution.

periodically performed over the TRD, both to the environment conditions which have been explained in the section 4.2.2.

As example, the median and RMS of templates as a function of time appears more stable after 2011. This is due to the fact that TRD was first operated with weekly adjustments of the high voltage, so that diffusion losses caused a gradual increase of the gas gain. This strategy was changed effective October 26th, 2011, and daily adjustments of the high voltage are now being done, in order to keep the gas gain at a constant level. Whilst the sawtooth trend - more evident in the median and RMS protons template due to less statistical fluctuation respect to the electrons one - is due to the refilling procedure performed $\sim$ every month.

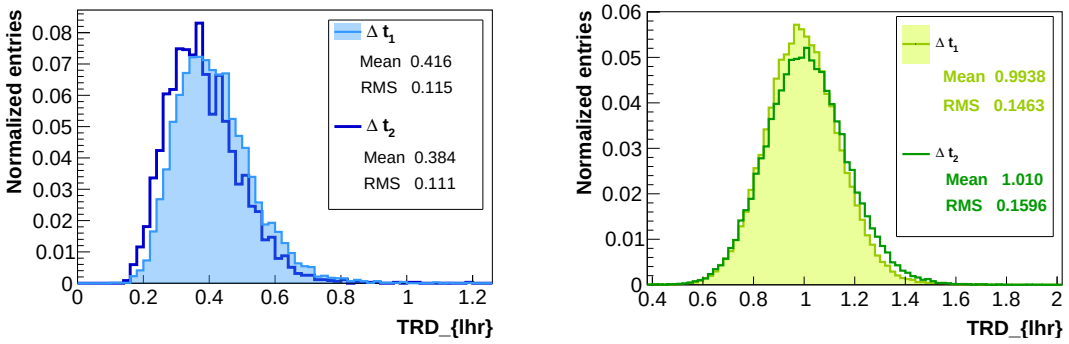

FIGURE 4.28: TRD_{lhr} distribution in two different time bin for electrons (left) and protons (right) samples selected on DATA.

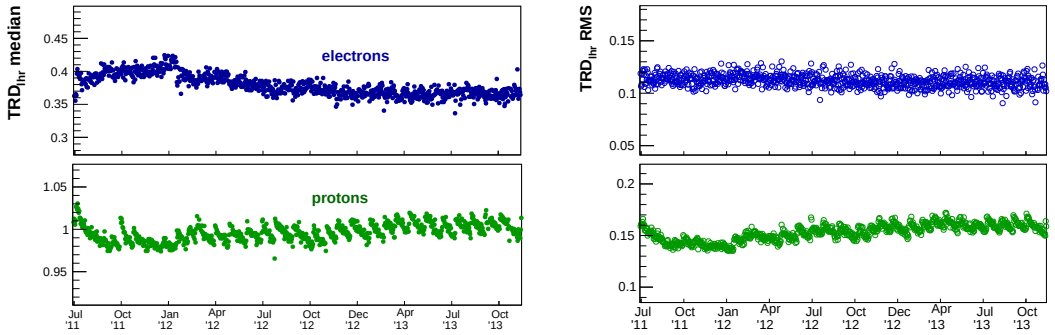

FIGURE 4.29: Median (left) and RMS (right) of TRD_{lhr} distribution as a function of time for electrons and protons samples selected on DATA.

Due to the time dependence of TRD signal show above, the reference distributions should be defined not only for each energy bin, but also for each time bin.

4.4 Fitting procedure

The number of e^- and e^+ have been statistically extracted from the overwhelming background of protons using a fitting procedure performed over the TRD_{lhr} distribution.

The sample to fit has been selected from data applying the preselection (see section 4.1) and the request on the charge sign (negative in case of electrons, positive in case of positrons). The resulting sample contains both signal and background.
For each energy bin and for each time bin, the TRD_{lhr} distribution of data is fitted as a sum of a signal and background contributions using the TRD_{lhr} templates and following the `RooFit` method [82, 83]. As described in **??** and as will be deeper discussed in section **??** the TRD_{lhr} templates have been defined directly from preselected data applying request on $ECAL_{BDT}$, E/R and the charge sign.

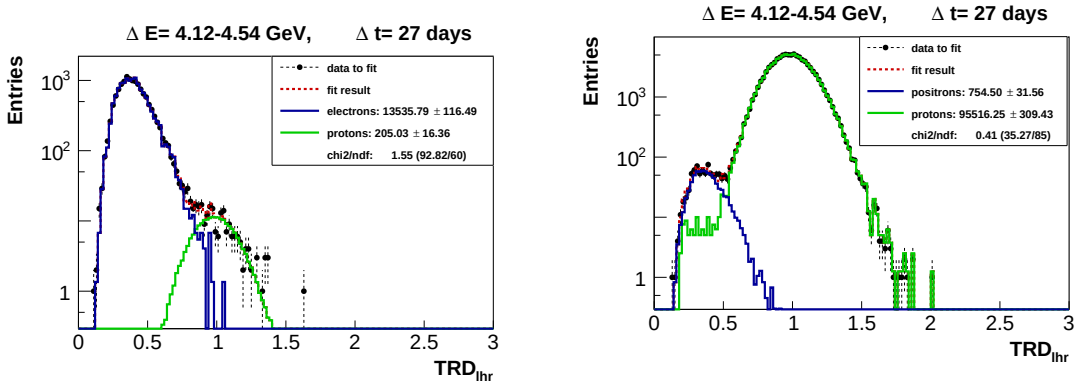

FIGURE 4.30: An example of the fitting procedure in one energy bin ($\Delta E = 3.73 - 4.12\,GeV$) and in one time interval of 27 days for the extraction of e^- (left) and e^+ (right): the black point are preselected data with positive charge sign, the red dashed line is the result of the fit that correspond to the sum of signal (blue line) and background (green line).

An example of the fitting procedure in one energy bin ($\Delta E = 3.73 - 4.12\,GeV$) and in a time interval of 27 days is shown in figure 4.30, both for the extraction of the number of e^- and of the number of e^+. The black point is the sample to fit, defined from data, the red dashed line is the result of the fit that correspond to the sum of signal (blue line) and background (green line).

However, the shape of templates strongly depends from the selection applied to define them. Different templates gives a different fit result. For this reason in each ΔE and Δt several fit have been performed with different signal and background templates. In particular, 436 different templates (i.e. 436 different fits) have been

used to fit the number of electrons and 144 different templates (i.e. 144 different fits) for the number of protons. More details will be given in section 4.4.1.

Each fit gives a different number of fitted electrons or positrons. The results obtained in one energy and time bin for electrons and positrons is shown in figure 4.37 with the relative distribution of reduced χ^2 obtained from the fits. As discussed in section **??**, only the result with the 45 best χ^2 for electrons and with the best 15 χ^2 for positrons have been taken into account. The distributions of the fitted number of electrons and positrons obtained with the best χ^2 are shown in figure **??**. The mean of distribution of fitted electrons or positrons has been taken as the number of observed e^- ($\#e^-_{obs}$) or observed e^+ ($\#e^+_{obs}$)

Figure **??** (left) shows $\#e^-_{obs}$ and observed $\#e^+_{obs}$, coming from the fitting procedure shown above, in one time interval of 27 days as a function of the reconstructed energy.
However, in order to obtained the correct number of electrons and positrons observed ($\#e^{\pm}_{true}$), the fraction of charge confused events has been taken into account in order to correct the number of electrons and positrons ($e^{\pm}_{obs}$) according to the equation 4.4 and using MC as described in section 4.2.3.
The figure **??** (right) shows the fraction of charge confused events ($\#e_{obs}/\#e_{true}$)) as a function of energy. A already discussed in section 4.2.3, the cc confusion affected more positrons than electrons and spoils the result of $\sim 20\%$ at 40 GeV.

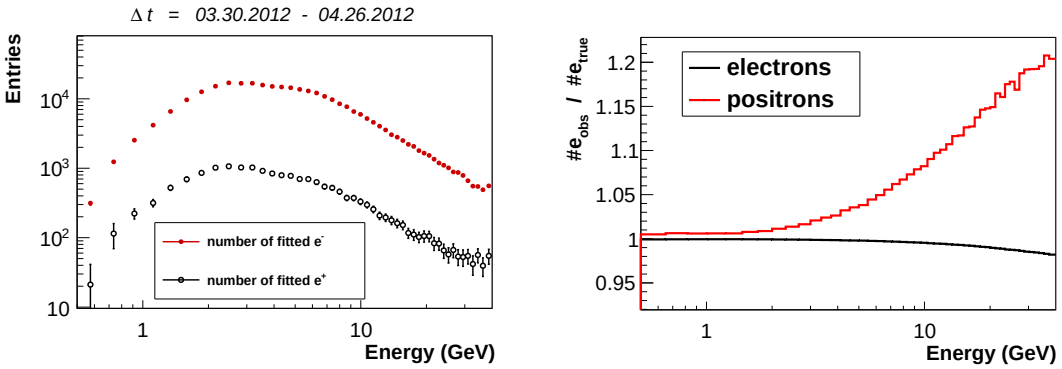

FIGURE 4.31: Left: Number of observed e^- and observed e^+, coming from the fitting procedure, in one time interval of 27 days. Right: Fraction of charge confused events ($\#e_{obs}/\#e_{true}$)) as a function of energy.

4.4.1 Uncertainties

The number of electrons and positrons evaluated by the fitting procedure shown above is affected both by an error that came from the statistical fluctuations, both by an error that came from the systematic uncertainties.

Statistical fluctuation uncertainties

The error due to the statistical fluctuations, is defined by the poisson statistic as $\delta_{poisson} = \sqrt{\#e^{\pm}}$ where $\#e^{\pm}$ is the number of fitted electrons or positrons. As figure **??** shows, the number of $\#e^{\pm}$, hence $\delta_{poisson}$, depends on the energy. Another variable that affects $\delta_{poisson}$ is the width of the time interval in which analysis is performed. As figure ?? shows, at low energies ($\Delta E = 3.73 - 4.12\,GeV$) the number of e^+ and e^- measured using data of 1 day presents a very high statistical fluctuations: $\delta_{poisson}\#e^- \sim 4\%$ in the case of electrons and $\delta_{poisson}\#e^- \sim 20\%$. At higher energies ($\Delta E = 27.25 - 28.68\,GeV$) the situation getting worst: for electrons $\delta_{poisson}\#e^-$ increases up to $\sim 20\%$ and for positrons up to $\sim 70\%$. Using the data taken in one year, $\delta_{poisson}\#e^-(e^+)$ decreases up to $\sim 0.3\%(1\%)$ for low energies and up to $\sim 1\%(3\%)$ at higher energies.

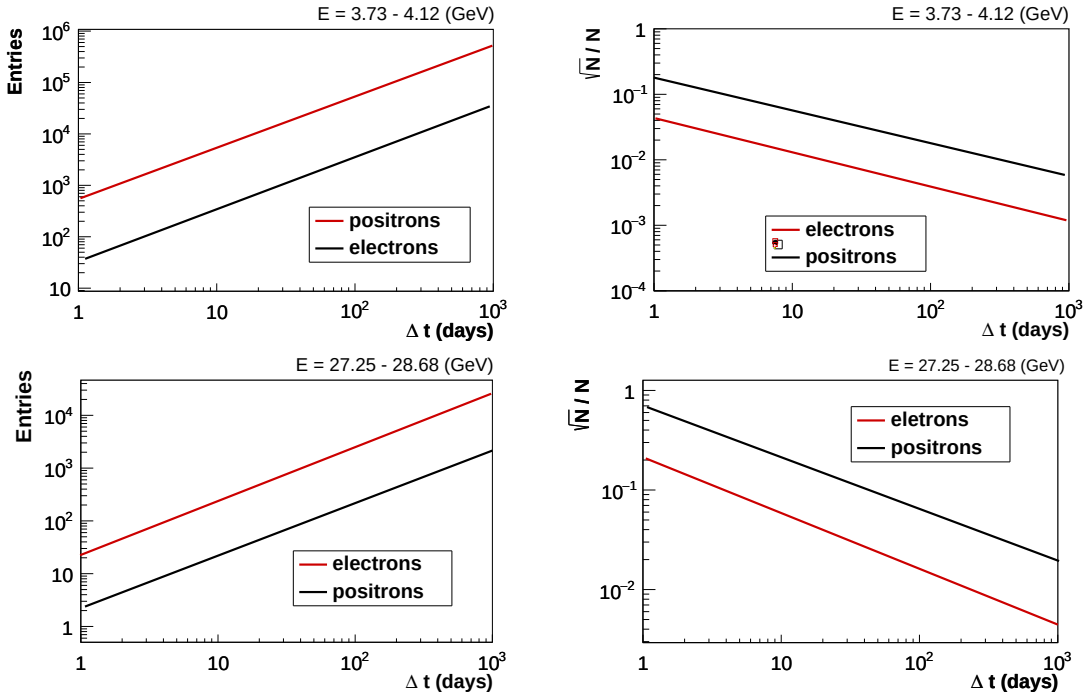

FIGURE 4.32: Number (left) and the relative statistical error (right) of fitted electrons (red point) and positrons (black point) as a function of the time bin used for the analysis, in two different energy bin.

Systematic uncertainties

The systematic uncertainties can be divide in two categories:

- Systematic related to the **finite TRD e/p separation capabilities** (δ_{sep});
- Systematics related to the templates definition, in particular the one related to the selection used to obtain the templates (δ_{sel_tmpl}) and the one related to the finite statistic of the templates (δ_{stat_tmpl}).

From the total error given by the fitting procedure (σ_{fit}), it is possible to obtained the *separation systematic* error (δ_{sep}) according to the following relation:

$$\sigma_{fit} = \delta_{sep} \bigoplus \delta poisson \tag{4.8}$$

Figures **??** and ?? show the relative error $\sigma_{fit}/\#e^{\pm}$ respectively for electrons and positrons as a function of energy and the single components coming from δ_{sep} and $\delta poisson$. For the electrons the mayor contribution to σ_{fit} is given by the statistical error $\delta poisson$ while the error coming from the separation capabilities of TRD can be neglected. This means that there is no need of an additional cut (for example over the ECAL variables) to suppress the proton background as instead is needed for the high energy part [84].
For positrons this is true only above ∼2 GeV. This indicates that below this energy, the TRD is not able to clearly separate protons from positrons. However there is no way to reduce background below this energy applying other cuts without loosing a consistent part of the statistic.

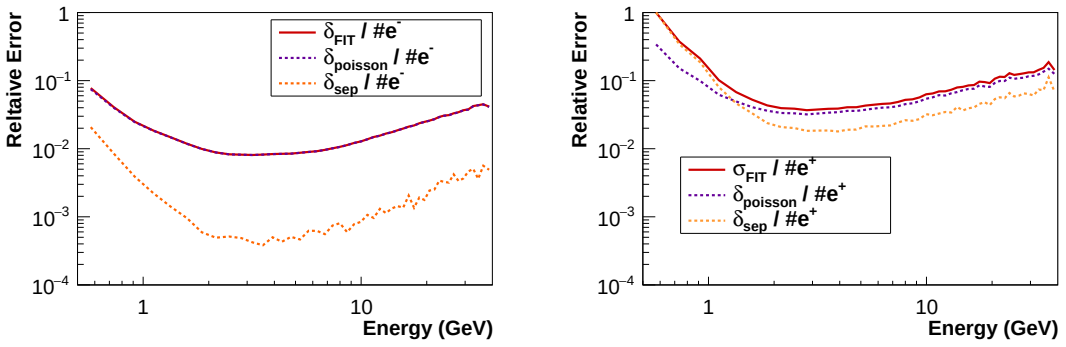

FIGURE 4.33: Relative error coming from the fit (red line) with the single components coming from the statistic (violet dashed line) and from the separation power of TRD_{lhr} variable (orange dashed line) for electrons (left) and positrons (right).

The systematic error due to the selection applied in order to obtain the templates distribution is not correlated with the fitting procedure. It comes from the limit knowledge of the signal and backgrounds templates. In this analysis MC data are not used for the definition of templates, since as explained in section 4.2.2 the TRD distribution between DATA and MC are not in agreement.

This means that the templates should be selected directly from data. In order to have a clean sample of electrons and protons in order to define respectively signal and background templates, a cut over BDT, Sign of Rigidity and energy rigidity ratio, has been applied. However, the templates distribution can be affected by the selection applied to obtain them as show in figures 4.34 and 4.35 for 2 different energy bin.

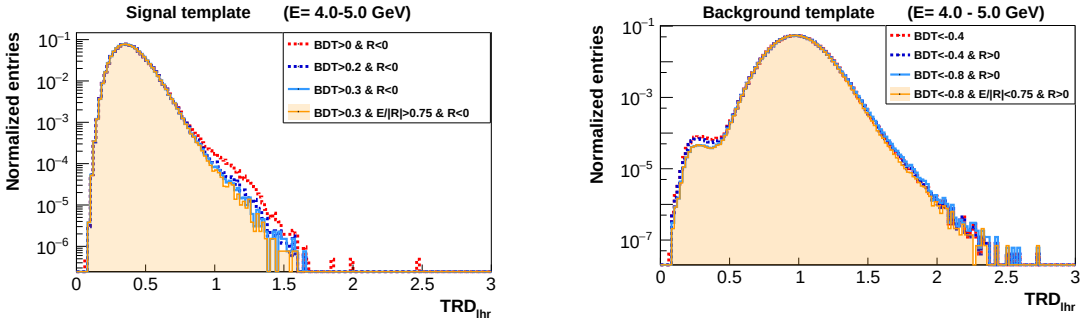

FIGURE 4.34: Templates distribution for signal (*left*) and background (*right*) obtained from different selections, in the energy interval E=4–5 GeV.

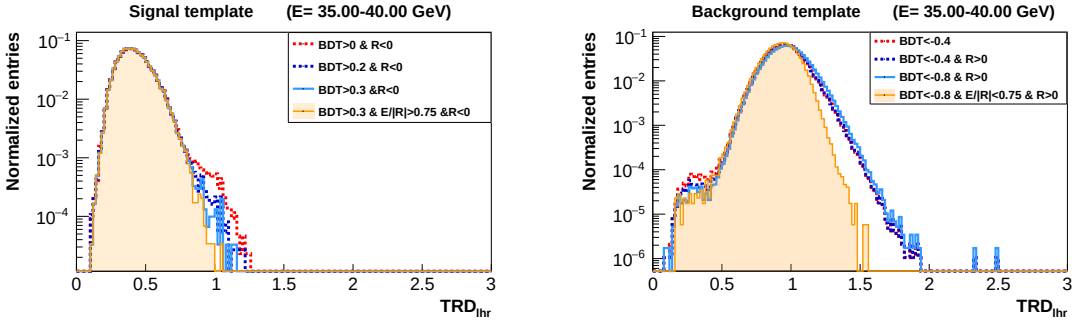

FIGURE 4.35: Templates distribution for signal (*left*) and background (*right*) obtained from different selections, in the energy interval E=35–40 GeV.

The second peak for low energy value of TRD_{lhr} that can be observed in the protons template is due to Helium nuclei that fragment in the top of AMS and that are reconstructed as unitary charge particles by the inner tracker. This can be clearly seen in figure 4.36 that shows, for the protons sample used to defined the template, TRD_{lhr} as a function of the charge measured using only the energy deposited on the first Tracker Layer. In order to select the protons template, the request to have a

unitary charge measured by the inner tracker has been applied. However the figure show a population with likelihood value less then 0.5 that has Z=2 according to the first tracker layer.

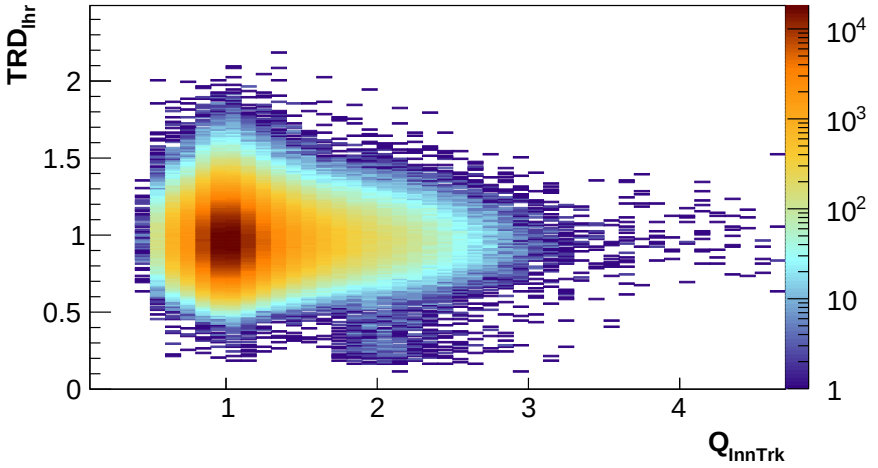

FIGURE 4.36: TRD_{lhr} vs the charge measured by the first layer of tracker (Z_{L1}) for the proton template sample. The second population with low value of TRD_{lhr} are Helium according to Z_{L1}.

Several definitions of templates have been applied in order to estimate the systematic on the selection applied (δ_{sys_tmpl}). For each template, a fit has been performed in order to extract the signal. Since the shape of the templates both for signal and background is different at each fit, this means that at each template will correspond a different number of e^- and e^+.

For the estimation of $\delta_(systempl)$ a time-integrated analysis has been applied, using the data of 30 months. With the time integrated approach the error coming from the finite statistic of template in the calculation of δ_{sys_templ} can be neglected.

For electrons, 12 different templates have been defined, combining 4 different cuts on BDT and 3 different cuts on energy/rigidity ratio (E/R):

$$selection + R < 0 + \begin{bmatrix} ECAL_{BDT} > 0.1 \\ ECAL_{BDT} > 0.2 \\ ECAL_{BDT} > 0.25 \\ ECAL_{BDT} > 0.3 \end{bmatrix} + \begin{bmatrix} E/R > 0 \\ E/R > 0.5 \\ E/R > 0.75 \end{bmatrix} \tag{4.9}$$

For protons, 36 different templates have been defined, combining 4 different cuts on BDT, 3 different cuts on energy/rigidity ratio (E/R) and 3 different cuts on Rigidity

sign:

$$selection \begin{bmatrix} R > 0 \\ R < 0 \\ allR \end{bmatrix} + \begin{bmatrix} ECAL_{BDT} > 0.1 \\ ECAL_{BDT} > 0.2 \\ ECAL_{BDT} > 0.25 \\ ECAL_{BDT} > 0.3 \end{bmatrix} + \begin{bmatrix} E/R > 0 \\ E/R > 0.5 \\ E/R > 0.75 \end{bmatrix} \tag{4.10}$$

In order to extract the signal for e^- all the electrons and protons templates have been used, for a total of 432 combinations, hence 432 fit have been performed.

For the extraction of the signal for e^+, all the 12 electrons templates have been used. For protons template have been taken into account only the templates defined with R¿0 since in the case of positrons, protons with negative rigidity cannot constitute source of background. In order to extract the number of e^+ a total of 144 combination of templates have been used, for a total of 144 different result.

The obtained results for one energy bin and the relative reduced χ^2 distribution obtained from the fit are shown in figures 4.37 and 4.38 respectively for electrons and positrons.

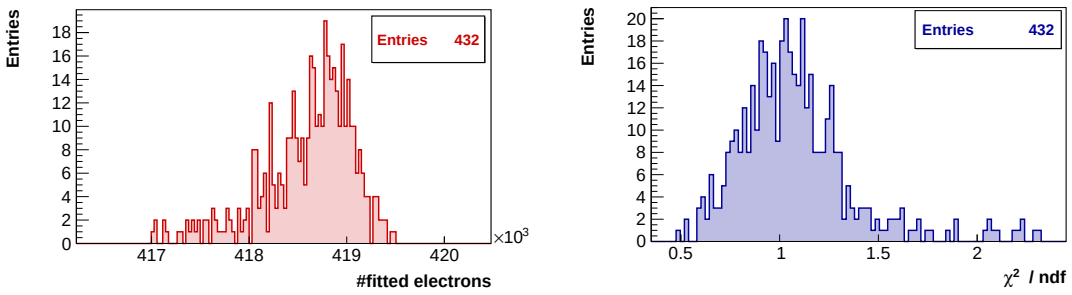

FIGURE 4.37: Obtained number of fitted electrons (left) in one energy bin and the relative reduced χ^2 distribution (right).

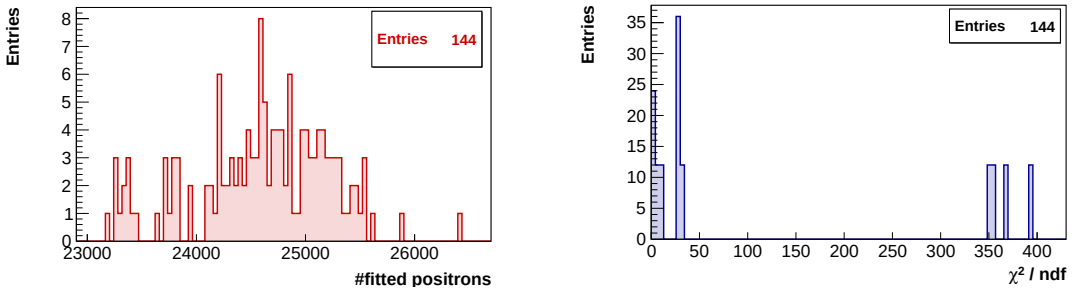

FIGURE 4.38: Obtained number of fitted positrons (left) in one energy bin and the relative reduced χ^2 distribution (right).

Following the same procedure applied for the number of observed events (see section **??**), between the different 432(144) number of $e^-(e^+)$ obtained from the fitting procedure, only the 45(15) results with the best chi^2 returned by the fitting procedure have been taking into account. The MEAN and RMS of the distribution of the results with the best χ^2 have been respectively taken as the time integrated number of observed events $((e^{\pm}_{obs})^{TOT}$ and the time integrated systematic error coming from the selection of template $(\delta^{TOT}_{sys_t empl})$. In order to obtained the value of $\delta_{sys_t empl}$ in one time interval $(\delta^{\Delta t}_{sys_t empl})$ the following formula has been applied:

$$\frac{\delta^{\Delta t}_{sys_t empl}}{e^{\pm}_{obs}}^{\Delta t} = \frac{\delta^{TOT}_{sys_t empl}}{e^{\pm}_{obs}}^{TOT} \quad \rightarrow \quad \delta^{\Delta t}_{sys_t empl} = \frac{\delta^{TOT}_{sys_t empl}}{(e^{\pm}_{obs})^{TOT}} \cdot (e^{\pm}_{obs})^{\Delta t} \tag{4.11}$$

where $(e^{\pm}_{obs})^{\Delta t}$ is the number of observed events in the time interval Δt.

Another systematic error comes from the finite statistic of the templates (δ_{stat_tmpl}). For the estimation of $\delta_{stat_t mpl}$, in each energy bin and in one time interval[3] the following procedure has been applied:

1. Templates distributions for e and p are generated. Each i^{th} template bin has been filled with a random number from a poisson distribution with mean N_i -1, where N_i is the number of the events in each i^{th} bin of the reference distribution obtained from an arbitrary choice between the signal and background templates definitions show above.

2. The fit procedure is performed in order to extract the signal.

This procedure has been applied 1000 times in each energy bin. This means that for each ΔE there are 1000 different numbers of $e^{\pm}$. The RMS of the distribution of these 1000 result for $e^{\pm}$ has been taken as the error coming from the finite statistic of templates.

In figure 4.39 are shown as a function of energy the total relative error on e^- and e^+ $(\delta_{tot}/\#e^{\pm})$ obtained from the fitting procedure and its components σ_{fit}, δ_{sys_tmpl}, δ_{stat_tmpl}[4]. The major contribution to δ_{tot}, is given by the error coming from the fit

[3]Here there is the assumption that the error due to the finite statistic of the templates doesn't change in time. For this reason it is evaluated only in one time interval Δt.

[4]The total error on the number of e^- and e^+ (δ_{tot}) can be written according to this formula: $\delta_{tot} = \sigma_{fit} \bigoplus \delta_{stat_t mpl} \bigoplus \delta_{sys_t mpl}$.

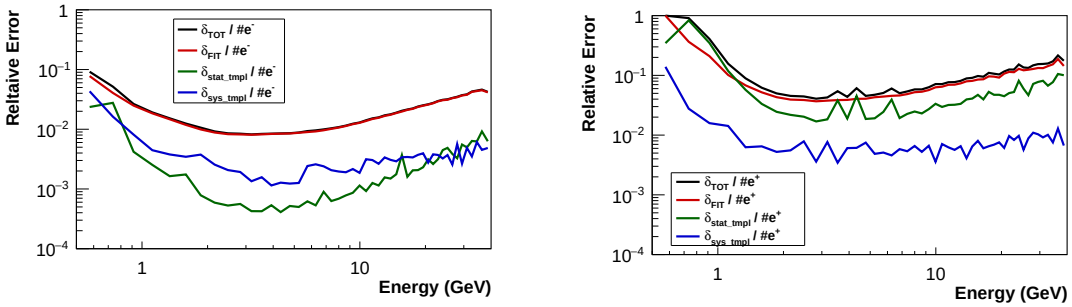

FIGURE 4.39: total relative error on e^- (left) and e^+ (right) obtained from the fitting procedure and its components σ_{fit}, δ_{sys_tmpl}, δ_{stat_tmpl} as a function of energy.

σ_{fit}, hence from the statistical poisson fluctuation (as already discuss for Figures **??** and ??).

Respect to the $\delta_{poisson}$ the contribution given by the systematic uncertainties (which major contribution is given by the uncertainties related to the selection of templates δ_{sel}) is negligible.

Chapter 5

Efficiencies study in time

In this section will be reviewed all the efficiencies of the cuts applied on DATA and MC that are contained in the preselection described in section 4.1.
The efficiencies will be study as a function of time, in order to maximize the statistic used in the acceptance correction factor, defined in chapter 3.

5.1 Efficiency evaluation

As explained in chapter 4, a list of cuts, which constitutes the *preselection* (see section 4.1) has been applied on DATA in order to define the sample from which extract the signal of $e^{\pm}$.

The acceptance of this preselection has been evaluated from MC electrons and corrected for a factor K that take into account DATA/MC discrepancies (see 3.4).

For the evaluation of K all the cuts contained in the preselection have studied on DATA and MC electrons samples as a function of energy and, in case of DATA, also as a function of time.
However, while the MC electron sample has a purity of 100%, on DATA a strong selection has been applied in order to select a pure sample of electrons and to remove any background. The possible bias that a selection can introduce on a sample, should be taken into account and for this reason the same selection applied on DATA has been also applied on MC.

Moreover, a strong selection can introduce some bias on the result of the efficiencies. As example, this happens in the case of the reconstructed β by ToF and reconstructed $Track$ by Tracker. In a first approach, the β efficiency can be evaluated over sample that has at least one reconstructed track by the Tracker and, viceversa, the $Track$ efficiency can be evaluated over a sample of particles that have a reconstructed β by the ToF.
However, the responses of ToF and Tracker are strongly correlated. This introduce a bias in the MC acceptance evaluation that should be avoid. The solution adopted, is the following: the β efficiency has been evaluated using an *unbiased* sample, obtained without any request on Track and the the $Track$ efficiency is evaluated over a *biased* sample defined cutting on β.

The electrons samples used for the β and $Track$ efficiencies have been selected, both on DATA and MC, applying a selection based on ECAL and TRD variables. In addition, for the tracker efficiency, the request to have a unitary charge and relativistic downgoing particle has been added using the information coming from the ToF. The obtained efficiencies as a function of the reconstructed energy both for DATA and MC are shown in figure 5.1 and the relative DATA/MC ratio as a function of energy in figure 5.2. In the case of Track efficiency there is a very good agreement between data and MC, for the β efficiency the agreement is inside $\sim 1-2\%$

The efficiency of the request to have at least one reconstructed shower has been evaluated over an electrons samples selected on DATA by means of a weak selection. Only cuts on the TRD and Tracker variables have been applied since a cut on ECAL variables could completely spoils the value of this efficiency. For the same reason this efficiency has been evaluated as a function of the reconstructed rigidity since any informations coming from ECAL , as the reconstructed energy, imply the presence of a shower and will give an efficiency of 100%. The result as a function of the reconstructed rigidity is shown in figure 5.3a both for DATA and MC and the relative DATA/MC ratio in figure 5.3b that shows a very good agreement between data and MC.

The other two efficiencies related to the ECAL, are checking that the track is inside the ECAL fiducial volume and checking the tTrack-ECAL matching. As in the case of β and $Track$, also these two efficiencies are strongly correlated and a special care is needed in order to not repress any feature with a strong selection.
The check of Track inside the ECAL fiducial volume, has been evaluated over an

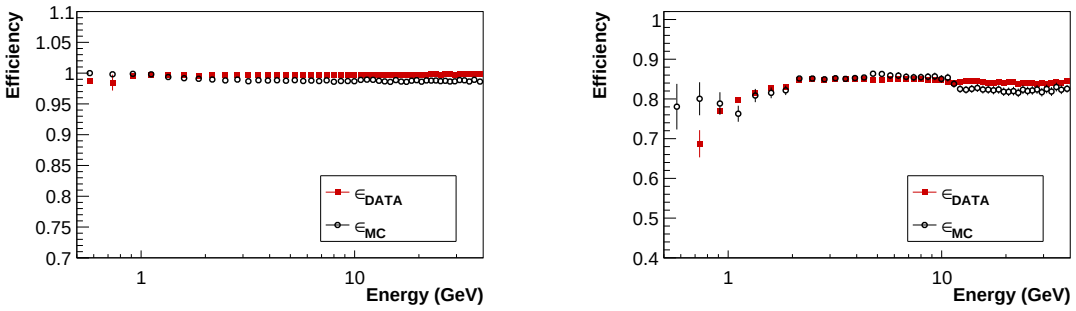

FIGURE 5.1: Efficiencies of β reconstruction (left) and Track reconstruction (right) as a function of the reconstructed energy both for DATA and MC.

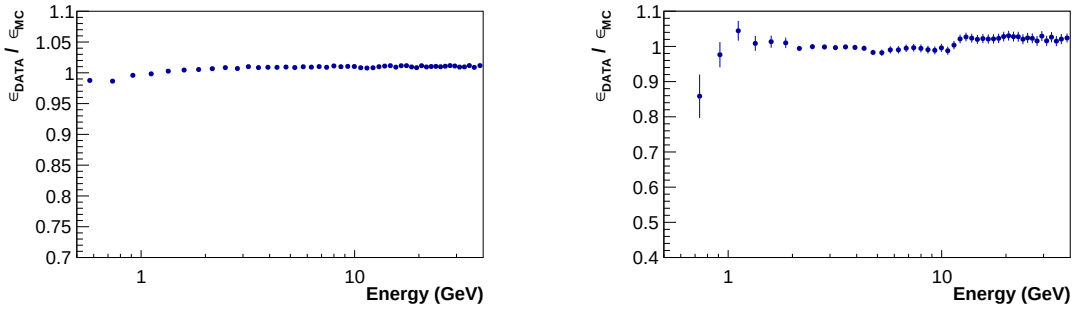

FIGURE 5.2: DATA/MC ratio of β reconstruction efficiency (left) and Track reconstruction efficiency (right) as a function of the reconstructed energy.

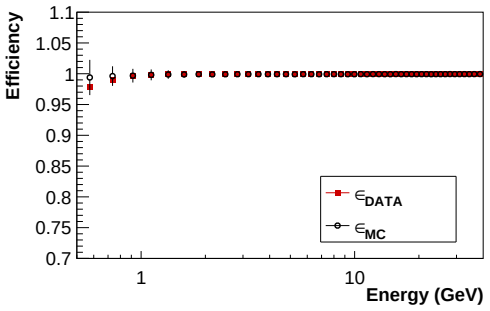

(A) Efficiencies of the request of ECAL reconstruction as a function of the reconstructed rigidity both for DATA and MC.

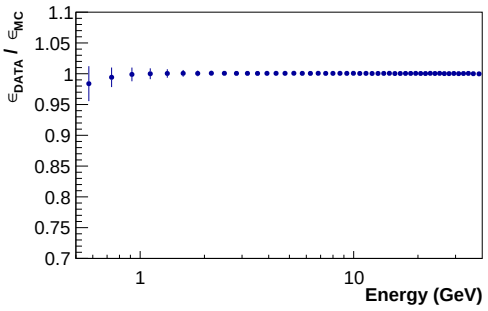

(B) DATA/MC ratio of request of ECAL reconstruction as a function of the reconstructed rigidity.

electrons samples selected using the informations coming from TRD, Tracker and also ECAL, excluding the request of Tracker-ECAL matching. The same sample, but adding the request to have the reconstructed track inside the ECAL fiducial volume, has been used for the evaluation of Tracker-ECAL match. The obtained results as a function of reconstructed energy are shown in figure 5.3 and the relative DATA/MC ratio in figure 5.4. For both efficiencies there is a very good agreement between DATA and MC except for energies below 1 GeV in the case of Track in ECAL fiducial volume.

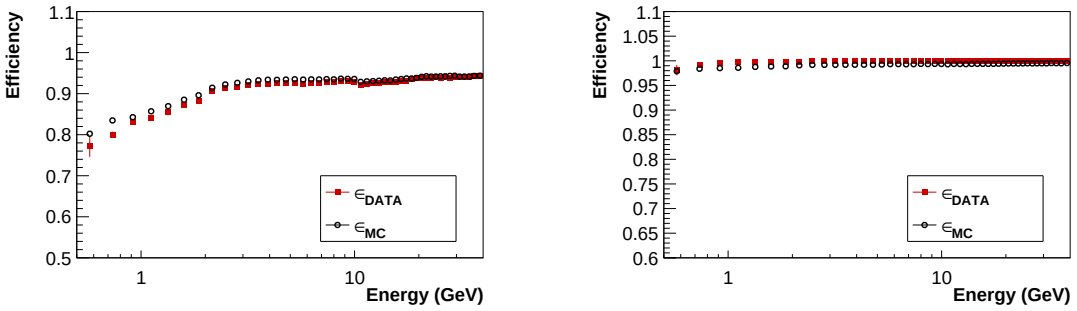

FIGURE 5.3: Efficiencies of the request to have Track inside the ECAL fiducial volume (left) and Track-ECAL matching (right) as a function of the reconstructed energy both for DATA and MC.

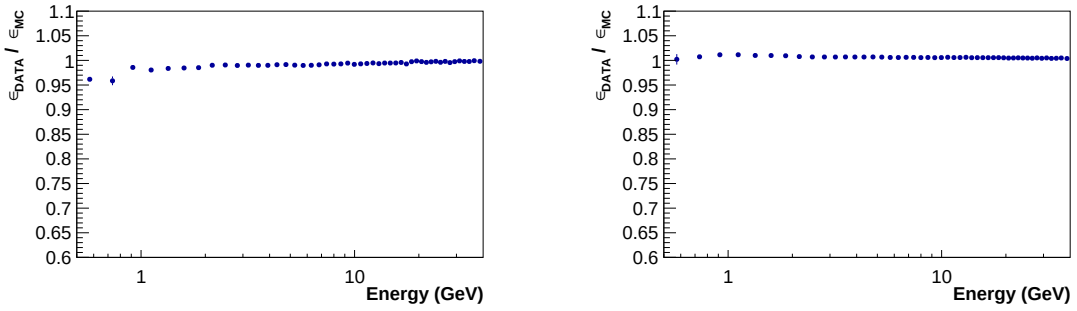

FIGURE 5.4: DATA/MC ratio of the request to have Track inside the ECAL fiducial volume (left) and Track-ECAL matching (right) as a function of the reconstructed energy both for DATA and MC.

The efficiency of the requests on TRD has been evaluated over an electrons samples selected using the ECAL variables and Tracker variables. no cuts on the TRD variables have been applied. The results for DATA and MC as a function of reconstructed energy and the relative DATA/MC ratio are shown in figures 5.5a and 5.5b. The requests on TRD include, as explained in section 4.1, three different cuts: a minimum number on the TRD hits used for the likelihood reconstruction, the existence of e/p likelihood ratio and a tight cut on e/He likelihood ratio used to remove residual helium. However the cuts on the likelihoods ratio have an efficiency of $\sim 100\%$ after the request on the number of TRD hits. So the trends as a function of energy shown in figures 5.5a and 5.5b are due only to the request on the number of TRD hits. For this cut, there is a good agreement between DATA and MC above 5 GeV but below this energy the comparison getting worst reaching a desagrement of $\sim 5\%$.

The efficiency of the requirement to have a unitary charge reconstructed by the inner Tracker (Z_{inn}) has been evaluated over an electrons samples selected using information coming from TRD, ECAL, ToF and Tracker. The obtained results for DATA and MC as a function of reconstructed energy are in good agreement as

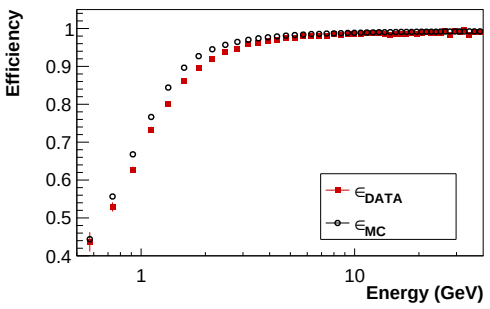

(A) Efficiencies of the request on the minimum number of reconstructed hits on TRD used for the likelihood as a function of the reconstructed energy both for DATA and MC.

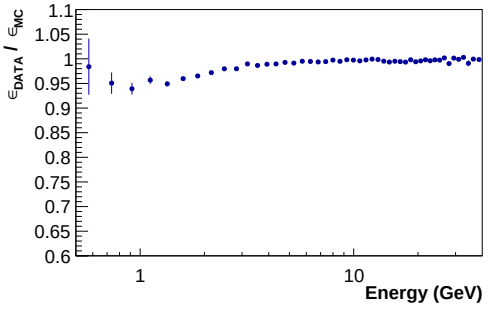

(B) DATA/MC efficiencies ratio of the request on the minimum number of reconstructed hits on TRD used for the likelihood as a function of the reconstructed energy.

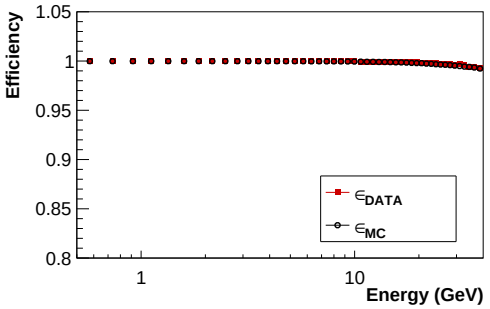

(C) Efficiencies of the request of unitary charge as a function of the reconstructed energy both for DATA and MC.

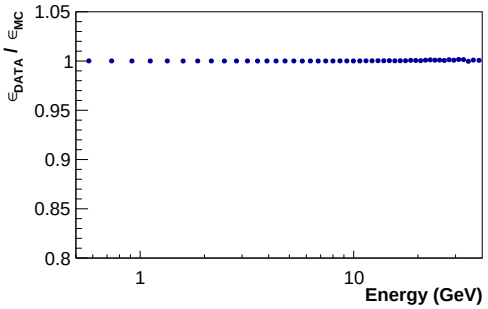

(D) DATA/MC efficiencies ratio of unitary charge as a function of the reconstructed energy.

shown in figures 5.5c and 5.5d. However this efficiency shows a slight decrease with the energy due to an asymmetric shape of Z_{inn} distribution for electrons sample where the energy starts to increase as explained in section 4.1.3. The asymmetric tail is due to secondary particles produced before the inner tracker or due to Bremsstrahlung events. This behavior is confirmed also by MC simulation.

The efficiencies of the requests to have only one reconstructed track and layer 2 in the tracker pattern have been evaluated on a clean sample of downgoing unitary charge particles selected using TRD, ECAL, ToF and Tracker. For the layer 2 efficiency is also required the single track. The results as a function of reconstructed energy both for DATA and MC are shown in figure 5.5 and the relative DATA/MC efficiencies ratio in figure 5.6. The single track efficiency is the one that present the major DATA/MC discrepancy. The DATA/MC discrepancy is up to $\sim 3\%$ in the considered energy range.

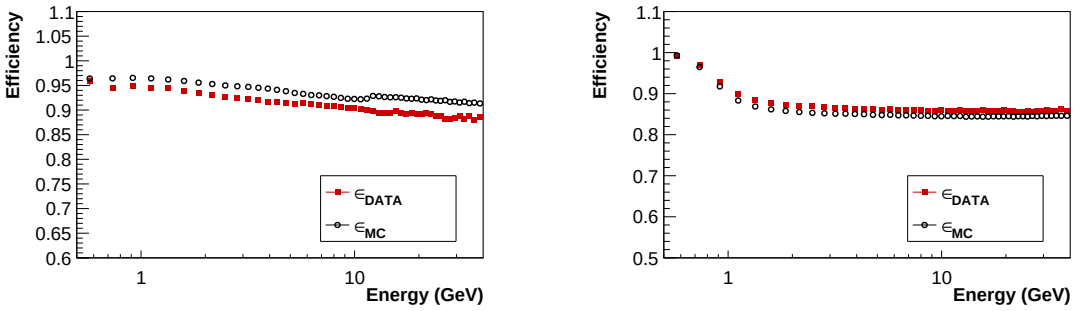

FIGURE 5.5: Efficiencies of the request to have one single Track (left) and layer 2 in tracker reconstruction (right) as a function of the reconstructed energy both for DATA and MC.

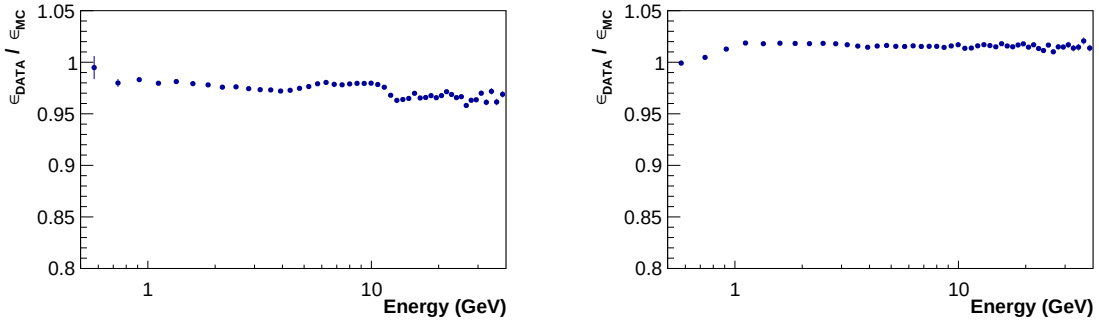

FIGURE 5.6: DATA/MC ratio of the request to have one single Track (left) and layer 2 in tracker reconstruction (right) as a function of the reconstructed energy both for DATA and MC.

5.1.1 DATA efficiencies as a function of time

An analytical way has been used to study the DATA efficiencies dependences on time as will be explained in section 5.3. However, a first look of the efficiencies trend as a function of time and energy integrated, can show some important features.

Figure 5.7, shows the efficiencies evaluated on DATA as a function of time and energy integrated for the request on charge, β, reconstructed shower, Track in ECAL acceptance and Track-ECAL matching. These efficiencies don't show particular trends as a function of time at least at the level.

In figure 5.8 are shown the efficiencies that present some trend as a function of time. The efficiencies related to the requests on Track reconstructed by the Tracker, show two jump: the first one between July and August 2011 and the second one between December 2011 and January 2012. These are due to well known events:

- On 24th August 2011, the procedure for the Tracker calibration has been

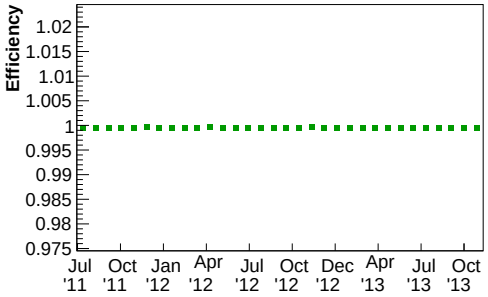

(A) Unitary charge request efficiency.

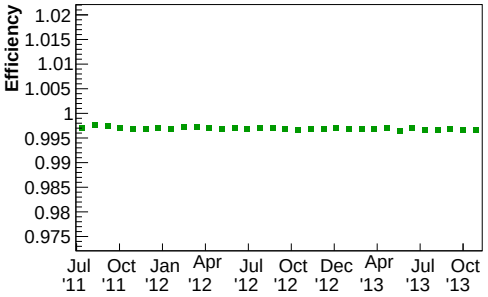

(B) β efficiency.

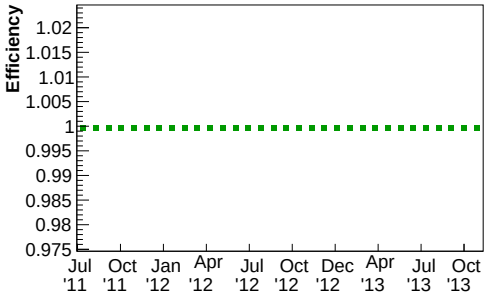

(C) Presence of a reconstructed shower efficiency.

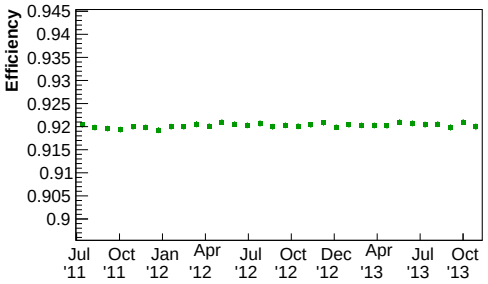

(D) Track in ECAL acceptance efficiency.

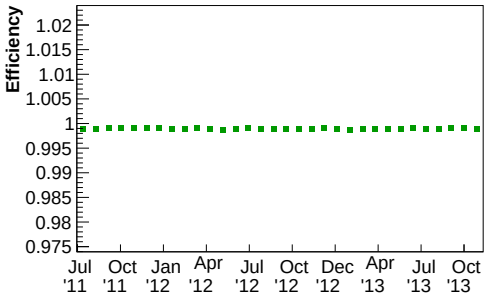

(E) Track-ECAL matching efficiency

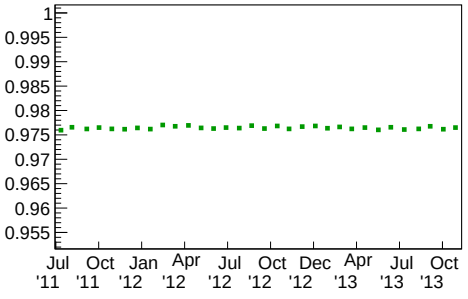

(F) Trigger efficiency.

FIGURE 5.7: Efficiencies on DATA as a function of time and energy integrated that don't show particular trend as a function of time at least at the level.

changed and this caused an increase in the tracker track reconstruction efficiency;

- On 1st December 2011, six ladders broke on x-side. This caused a decrease of the tracker track reconstruction efficiency.

Following the method shown in section 5.3.2, it has been observed that the time dependence of the requests related to the Track don't depend on energy.

The TRD efficiency clearly increase with time and the variation is $\sim 1.5\%$. Moreover, it has been found (with the method explained in section 5.3.2) that the time

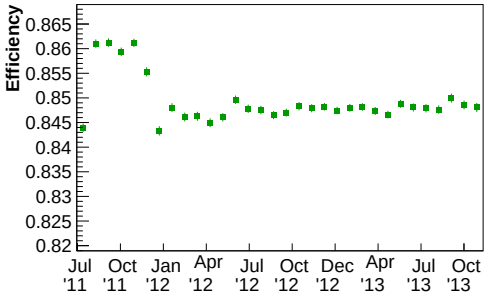

(A) Track reconstruction efficiency.

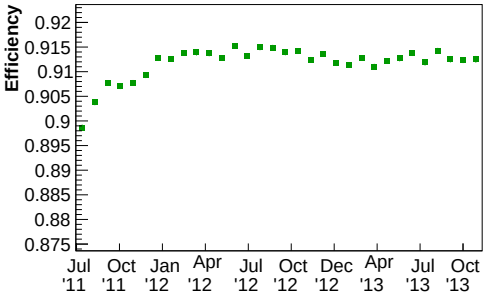

(B) Single track efficiency.

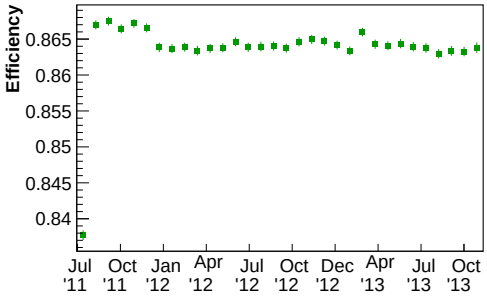

(C) Request of layer 2 efficiency.

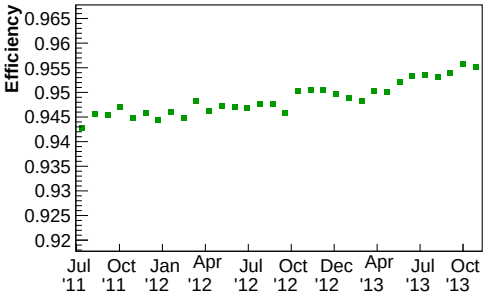

(D) TRD efficiency.

FIGURE 5.8: Efficiencies on DATA as a function of time and energy integrated that clearly show particulars trends as a function of time.

dependence of the TRD request changes with energy. Due to this correlation between energy and time dependences, the TRD efficiency is the only one that should be evaluated at each energy interval and at each time interval.

5.2 Method used to minimize the statistic fluctuation on K

As explained in section 3.4 the acceptance correction factor for a list of cuts, can be described by the equation 3.24:

$$\kappa(\Delta E, \Delta t) = \prod_i K(\Delta E, \Delta t)^i$$

where $K(\Delta E, \Delta t)^i$ is defined by the ratio between the efficiency for the i^{th} cut evaluated on DATA (ϵ_{DATA}) and the efficiency for the i^{th} cut evaluated on MC (ϵ_{MC}).

Both ϵ_{DATA} and ϵ_{MC} should be evaluated as a function of energy since all the efficiencies are energy dependent. In addition, only on DATA, the efficiencies should be evaluated as a function of time, in order to take into account possible time dependences.

This means that at each time interval and energy interval, will be correspond a different $K(\Delta E, \Delta t)$.

5.2.1 First approach for the evaluation of $K(\Delta E, \Delta t)$

According to the equation 3.24, the *first approach* that can be followed for the evaluation of $K(\Delta E, \Delta t)$ is the following: the efficiencies in each ΔE and Δt on electrons DATA ($\epsilon^{i}_{DATA}(\Delta E, \Delta t)$) for each cut applied in the preselection, have been evaluated using only the data taking during the time interval Δt.

As example, the efficiency on electrons data of the request to have only one reconstructed track evaluated in a time interval of 27 days is reported in figure 5.9 as a function of energy compared with the one obtained from MC electrons. Figure 5.9b show the contribution (calculated as the ratio between DATA/MC efficiency) to the factor K coming from the single track efficiency.

Evaluating al the DATA/MC ratio for the others efficiencies and performing the product according to 3.24, it is possible to obtain the factor K for the considered time interval Δt. The result is show in figure 5.10 as a function of energy and for one time interval of 27 days.

However this method presents some statistical problems, since the efficiencies on DATA are evaluated using only the data taken in the considered time interval As result, the evaluated K is subjected to a quite large statistical fluctuations, especially above 10 GeV as shown in figure 5.10.

5.2.2 *Time integrated approach* for $K(\Delta E, \Delta t)$ evaluation.

All the efficiencies that should be taken into account for the K evaluation are energy dependent. However, there are some efficiencies that don't change in time. For these efficiencies it is possible to use the whole statistic in order to decrease the statistical

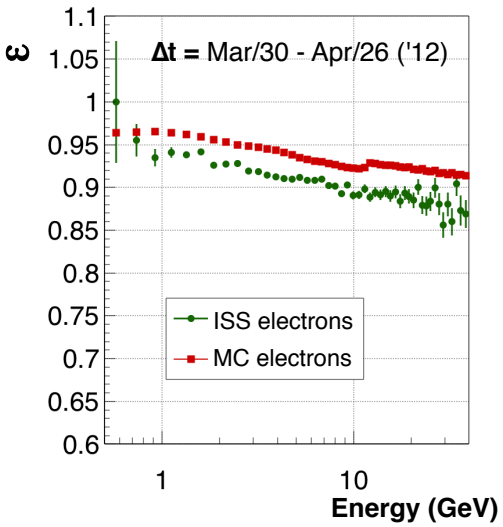

(A) Efficiency as a function of energy for MC electrons (red squared point) and ISS electrons data (green circle points). In the last case, in the calculation of the efficiency only the events taken during Δt = Mar/30–Apr/26 ('12) are taking into account.

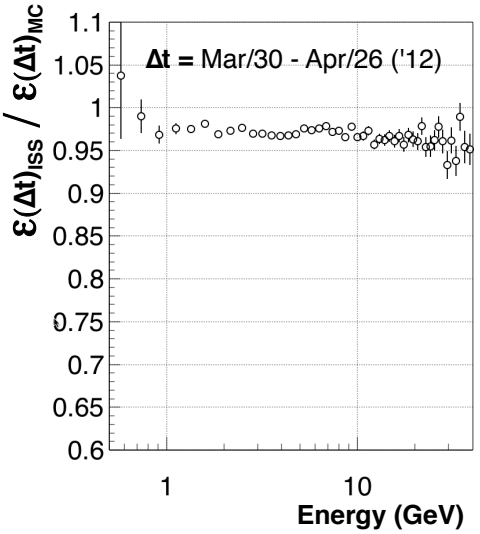

(B) Ratio between the ISS and MC efficiencies show in figure 5.9a.

FIGURE 5.9: Contribution to the acceptance correction due to the request to have only one reconstructed track in the time interval Δt = Mar/30–Apr/26 ('12)

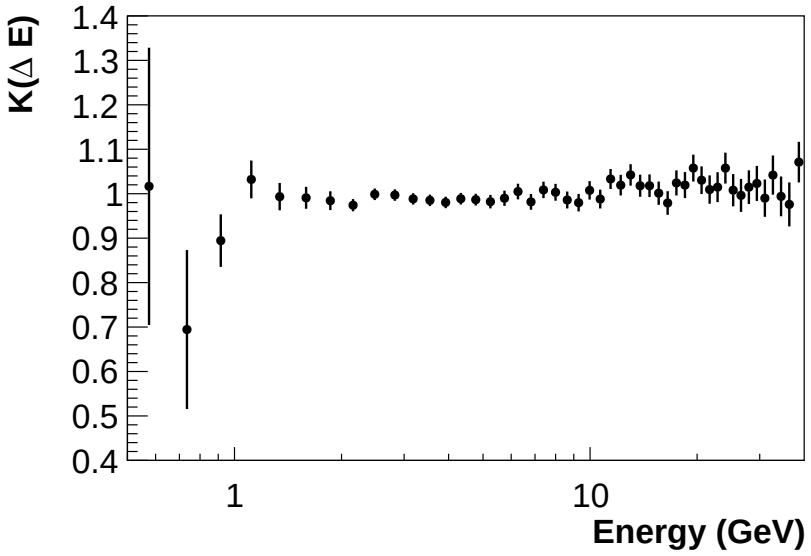

FIGURE 5.10: The obtained K as a function of energy for one time interval of 27 days with the *first approach*.

fluctuations on the final correction $K(\Delta E, \Delta t)$. For this purpose, a deep study of variation in time and energy of each efficiency is needed.

According to the kind of time dependence, the efficiencies can be divided into the following classes:

a. **Only E dependent**
   Efficiencies that depend from energy (E), but not from time.

b. **E and t dependent, E and t uncorrelated**
   Efficiencies that depend both from energy (E) and time (t), with the energy and time dependences *uncorrelated*.

c. **E and t dependent, E and t correlated**
   Efficiencies that depend both from energy (E) and time (t), with the energy and time dependences *correlated*.

In order to use the highest possible statistic, each class of efficiency is treated in a different way that will be explained in this section. The method used to divided the efficiencies into the three classes show above is explained in section 5.3.

The kind of time dependence can be described by a parameter ρ defined as follow:

$$\rho(\Delta E, \Delta t) = \frac{\epsilon(\Delta E, \Delta t)}{< \epsilon(\Delta E) >} \tag{5.1}$$

where:

- $\epsilon(\Delta E, \Delta t)$ is the efficiency in the time interval Δt and in the energy interval ΔE;
- $< \epsilon(\Delta E) >$ is the mean efficiency time integrated for the energy interval ΔE;

The time variation energy integrated ($< \rho(\Delta t) >$) will be:

$$< \rho(\Delta t) >= \frac{< \epsilon(\Delta t) >}{< \epsilon >} \tag{5.2}$$

where:

- $< \epsilon(\Delta t) >$ is the efficiency in the time interval Δt energy integrated;
- $< \epsilon >$ is the mean efficiency time and energy integrated;

a. Efficiencies only energy dependent

The efficiencies that belong to this class, are the following:

- trigger efficiency;
- TRD likelihood efficiencies;
- particle with shower;
- Track inside ECAL;
- Trk-ECAL match;
- β effciency;
- $Z_{TRK} < 1.5$;

These efficiencies doesn't depend on time and from equations 5.1 and 5.2 for these kind of efficiencies:

$$\rho(\Delta E, \Delta t) =< \rho(\Delta t) >= 1 \quad \rightarrow \quad \epsilon(\Delta E, \Delta t) =< \epsilon(\Delta E) > \tag{5.3}$$

Equation 5.5 said that for the calculation of $\epsilon^i_{DATA}(\Delta E, \Delta t)$ which is applied in order to obtained of $K(\Delta E, \Delta t)$, there is no reason to use only the data taken in the time interval Δt, but it can be evaluated was a function of energy and time integrated. In this way, it is possible to obtain a great improvement from the statistical point of view.

As example, the efficiency on DATA electrons of the request $Z_{TRK} < 1.5$ as a function of time, is shown in figure 5.11a both integrated over all energies, both for 2 different energy intervals (2.65–3.00 GeV and 14.25–15.14 GeV). Figure 5.11b shows the DATA/MC ratio for the Z efficiency, evaluated using only data taken in a time interval of 27 days and using a time integrated method. With the second method the statistical fluctuation are clearly decreased.

b. Efficiencies energy and time dependent, energy and time uncorrelated

The efficiencies that belong to this class, are the following:

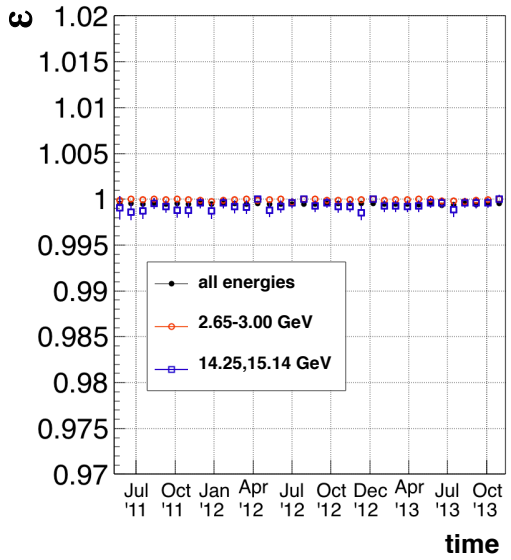

(A) Z_{TRK} <1.5 efficiency on DATA electrons as a function of time, integrated over all energies (black circle filled dots), and for 2 different energy interval, 2.65–3.00 GeV (black hollowed circle dots) and 14.25–15.14 GeV (blue hollowed square dots). There is no evidence of a time dependence at least at the level of 0.1%.

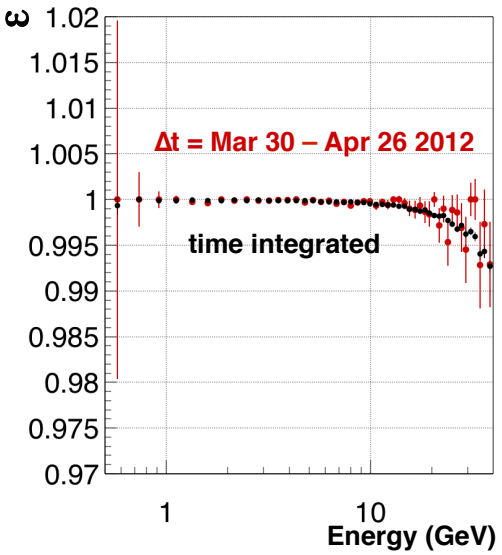

(B) Z_{TRK} <1.5 efficiency on DATA electrons as a function of energy. The red points are obtained using the DATA data taken in 27 days, the black points are obtained using data taken over all the 30 months. Since there is no time dependence evidence for the $K_(\Delta E, \Delta t)$ can be used the time integrated efficiency in order to improve the statistic.

- nTrTracks>0;
- nTrTracks=1;
- Layer2;

These efficiencies are both energy and time dependent, but the time and energy variations are uncorrelated. From equations 5.1 and 5.2 this means that:

$$\rho(\Delta E, \Delta t) =< \rho(\Delta t) > \quad \rightarrow \quad \epsilon(\Delta E, \Delta t) =< \epsilon(\Delta E) >< \epsilon(\Delta t) > \tag{5.4}$$

This means, that we can calculate $\epsilon(\Delta E, \Delta t)$ through $< \epsilon(\Delta E) >$ and $< \epsilon(\Delta t) >$ that are, respectively, energy and time integrated efficiencies.

As example, the figure 5.11, shows this method applied to the track efficiency.

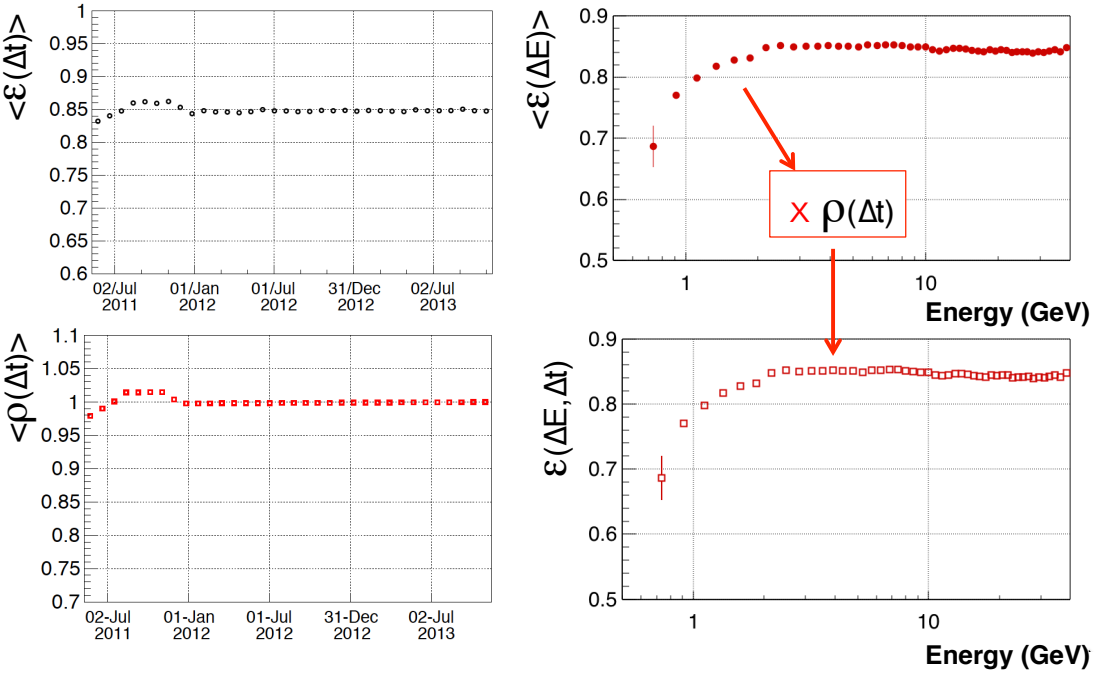

FIGURE 5.11: Method for the calculation of $\epsilon(\Delta E, \Delta t)$ applied in the case of the track efficiency (that belong to the class of efficiencies with time dependence and energy dependence uncorrelated).

c. Efficiencies energy and time dependent, energy and time correlated

The efficiency that belong to this class, is the request to have at leaf 9 hits on TRD for the likelihood reconstruction. Figure 5.12a shows the TRD cuts efficiencies as a function of time, energy integrated (black filled point) and for two different energy bins, 2.65–3.00 GeV (blue squared hollowed points) and 14.25-15.14 GeV (orange circle hollowed points). This efficiency depends both from energy and time, and the energy and time variations are *correlated*.
In this case, equations 5.1 and 5.2 give:

$$\rho(\Delta E, \Delta t) \neq < \rho(\Delta t) > \quad \rightarrow \quad \epsilon(\Delta E, \Delta t) = \epsilon(\Delta E, \Delta t) > \tag{5.5}$$

In this case, it is possible to calculate $\epsilon(\Delta E, \Delta t)$ only using the data taken in time interval Δt and which energy is in the interval ΔE as described in the *first approach* (see section 5.2.1). There is no way to increase the statistics and the TRD efficiency obtained in a time interval of 27 days is shows in figure 5.12b

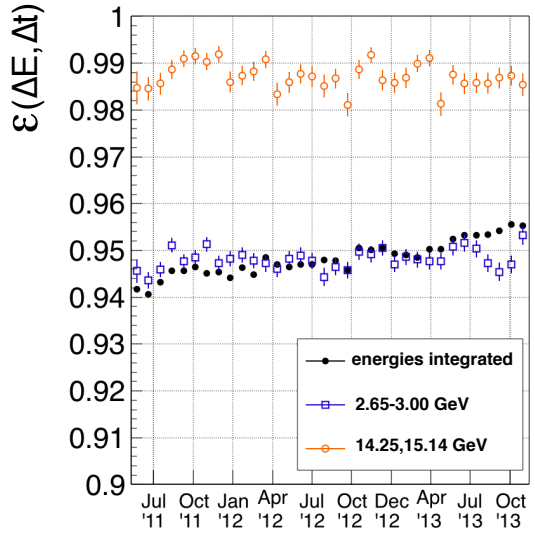

(A) TRD cuts efficiency as a function of time energy integrated (black filled point) and for two different energy bins, 2.65–3.00 GeV (blue squared hollowed points) and 14.25-15.14 GeV (orange circle hollowed points).

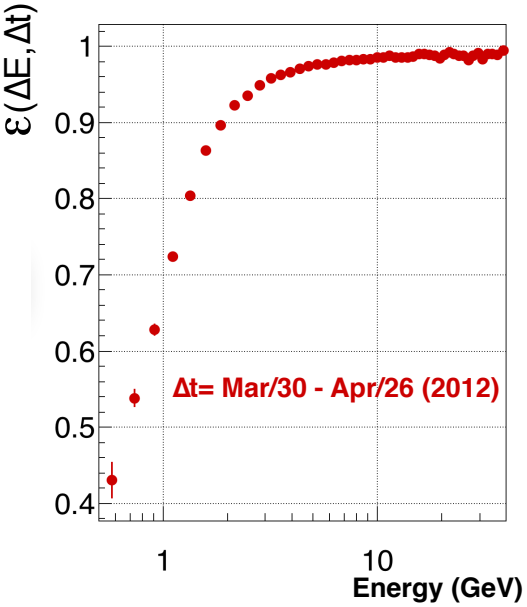

(B) TRD cuts efficiency as a function of energy calculate in a time interval of 27 days.

5.2.3 *First approach* vs *time integrated approach*

Figure 5.12 shows the improvement reached with the *integrated approach* in the $K(\Delta E, \Delta t)$ calculation, respect to the *first approach*.

5.3 Study of the time dependence

In order to divide the efficiencies on DATA into the three class described in section 5.2.2, the following method has been used.

5.3.1 Find the time dependence

For each efficiency ϵ, the following variable has been defined:

$$t_{var} = 1 - \frac{\epsilon(\Delta E, \Delta t_i)}{< \epsilon(\Delta E) >} \tag{5.6}$$

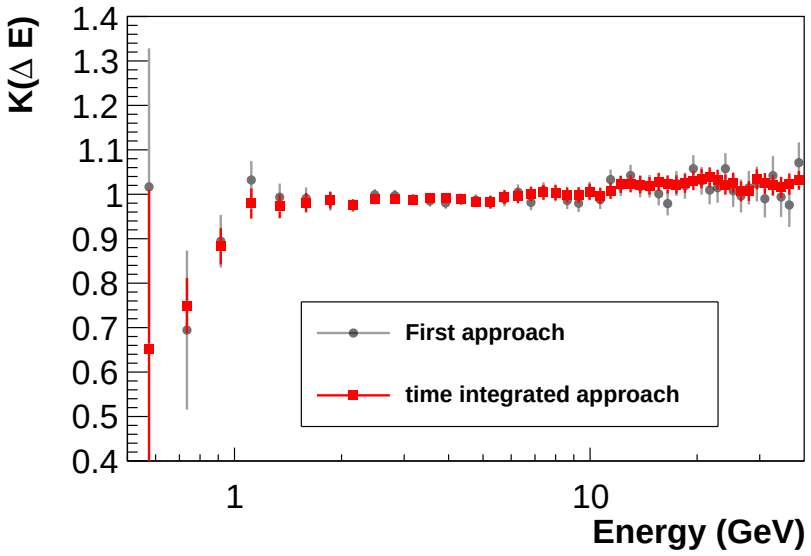

FIGURE 5.12: Comparison between K obtained with the *first approach* (gray points) and K obtained with the *integrated approach* (red points), in a time interval of 27 days.

where $\epsilon(\Delta E, \Delta t_i)$ is the efficiency evaluated as a function of energy and in the time interval Δt_i and $< \epsilon(\Delta E) >$ the efficiency evaluated in the the energy bin ΔE and time integrated.

The distribution of t_{var} for all the time intervals and all energy intervals indicates how much is the deviation for an efficiency at time Δt_i from the time integrated efficiency. If there aren't time dependences t_{var} is a symmetric distribution around 0 where the spread is given only by the statistical fluctuation.

Dividing t_{var} by the statistical errors of $\Delta E, \Delta t_i$ (δ_S)[1] a gaussian distribution is obtained which σ gives the information about the time dependence of the efficiency:

- a gaussian with $\sigma = 1$ implies no time dependences
- a gaussian with $\sigma \neq 1$ implies time dependences

As example, the distribution of t_{var} for the efficiency of the Track-ECAL and for the track efficiency are shown in figure 5.13. Both the distribution are symmetric respect to 0. Figure 5.14 shown the distribution of t_{var} divided by the statistical error δ_S with a superimposed gaussian fit. The sigma obtained in case of Track-ECAL matching efficiency is 1.056±0.059 and indicates that there aren't time dependences.

[1]The statistical errors coming from $\epsilon(\Delta E)$ are negligible respect to the ones coming from $\Delta E, \Delta t_i$.

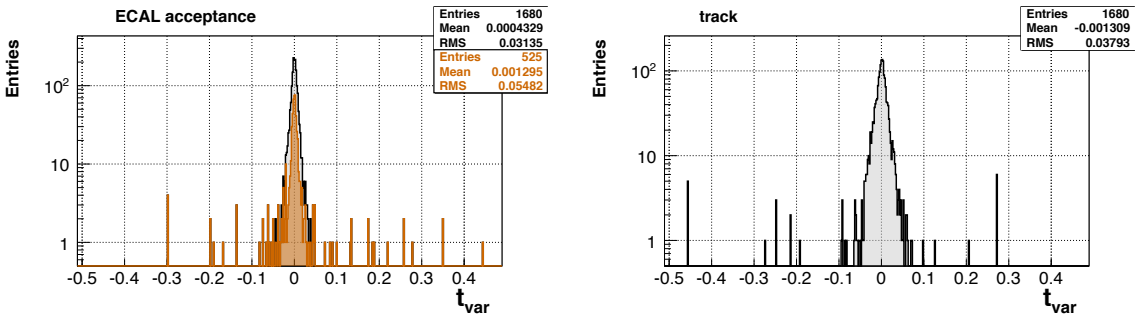

FIGURE 5.13: Distribution of t_{var} for the efficiency of the Track-ECAL (left)and for the track efficiency (right).

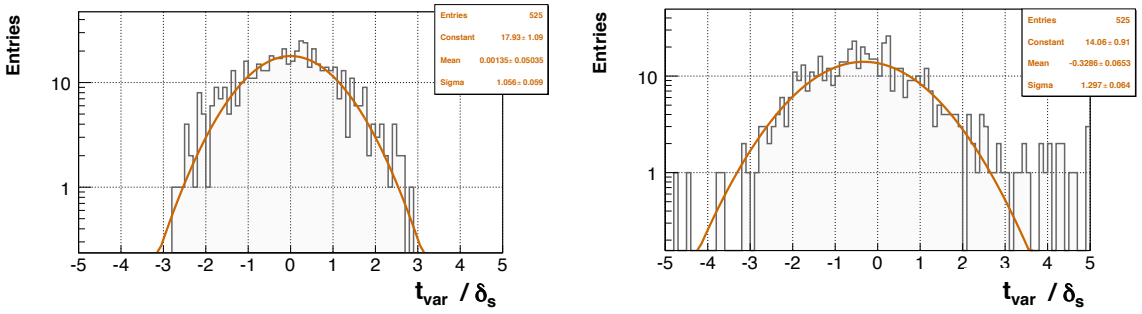

FIGURE 5.14: Distribution of t_{var} divided by the statistical error δ_S with a superimposed gaussian fit, for the Track-ECAL (left)and for the track efficiency (right).

In case of Track efficiency is 1.29±0.064 and this means that there are time dependences.

5.3.2 Correlation between time and energy dependences

With the method shows above, it is possible distinguish between the efficiency time dependent and not time dependent. However, there are no information about possible correlation between energy and time dependences.

In order to study this correlation, for each efficiency the following quantity have been study:

$$< \Delta\epsilon >=< \epsilon > - < \epsilon(\Delta E) > \tag{5.7}$$

and

$$\Delta\epsilon(\Delta t) =< \epsilon(\Delta t) > -\epsilon(\Delta E, \Delta t) \tag{5.8}$$

where:

- $< \epsilon >$ is the efficiency energy and time integrated;

- $< \epsilon(\Delta E) >$ is the efficiency time integrated in a given energy bin ΔE
- $< \epsilon(\Delta t) >$ is the efficiency energy integrated in a given time bin Δt
- $\epsilon(\Delta E, \Delta t)$ is the efficiency evaluated in a energy binΔE and in a time bin Δt

The equation evaluated in each ΔE gives a distribution which shape depends on the energy dependence of the efficiency ϵ.

The quantity $\Delta\epsilon(\Delta t)$ defined by the equation 5.8 is $< \Delta\epsilon >$ but evaluated in a given time interval Δt.

If the energy dependence of ϵ doesn't depend on time, this means that $\Delta\epsilon(\Delta t) \sim < \Delta\epsilon >$ otherwise $\Delta\epsilon(\Delta t) \neq < \Delta\epsilon >$. This feature can be described by the quantity:

$$\nu = < \Delta\epsilon > -\Delta\epsilon(\Delta t) \tag{5.9}$$

The distribution obtained for all the time interval Δt and all energy intervals ΔE of ν and divided by the statistical errors of $\epsilon(\Delta E, \Delta t)$ (δ_S)[2], gives a gaussian distribution which sigma contains the information about the energy and time correlations:

- $\sigma = 1$: the differences between $< \Delta\epsilon >$ and $\Delta\epsilon(\Delta t)$ are due only to the statistical fluctuation. There are no energy/time correlations;
- $\sigma > 1$: the differences between $< \Delta\epsilon >$ and $\Delta\epsilon(\Delta t)$ are due to the statistical fluctuation and to a systematic component. This last one is a sign of an energy/time correlation.

The distributions of ν/δ_S for the 4 efficiencies that are time dependent is reported in figure 5.15. A gaussian fit has been performed and the value of the σ has been taken in order to study the energy/time correlation.As result the efficiencies related to the track (presence of track, single track and presence of layer 2) as $\sigma = 1$ so they are classified as efficiencies without energy/time correlations. The distribution for TRD hits efficiency shows a $\sigma > 1$ so it is classified as an efficiency with energy/time correlations.

[2]The statistical errors on $< \epsilon >$,$< \epsilon(\Delta E) >$ and $< \epsilon(\Delta t) >$ are negligible respect to the ones on $\epsilon(\Delta E, \Delta t)$.

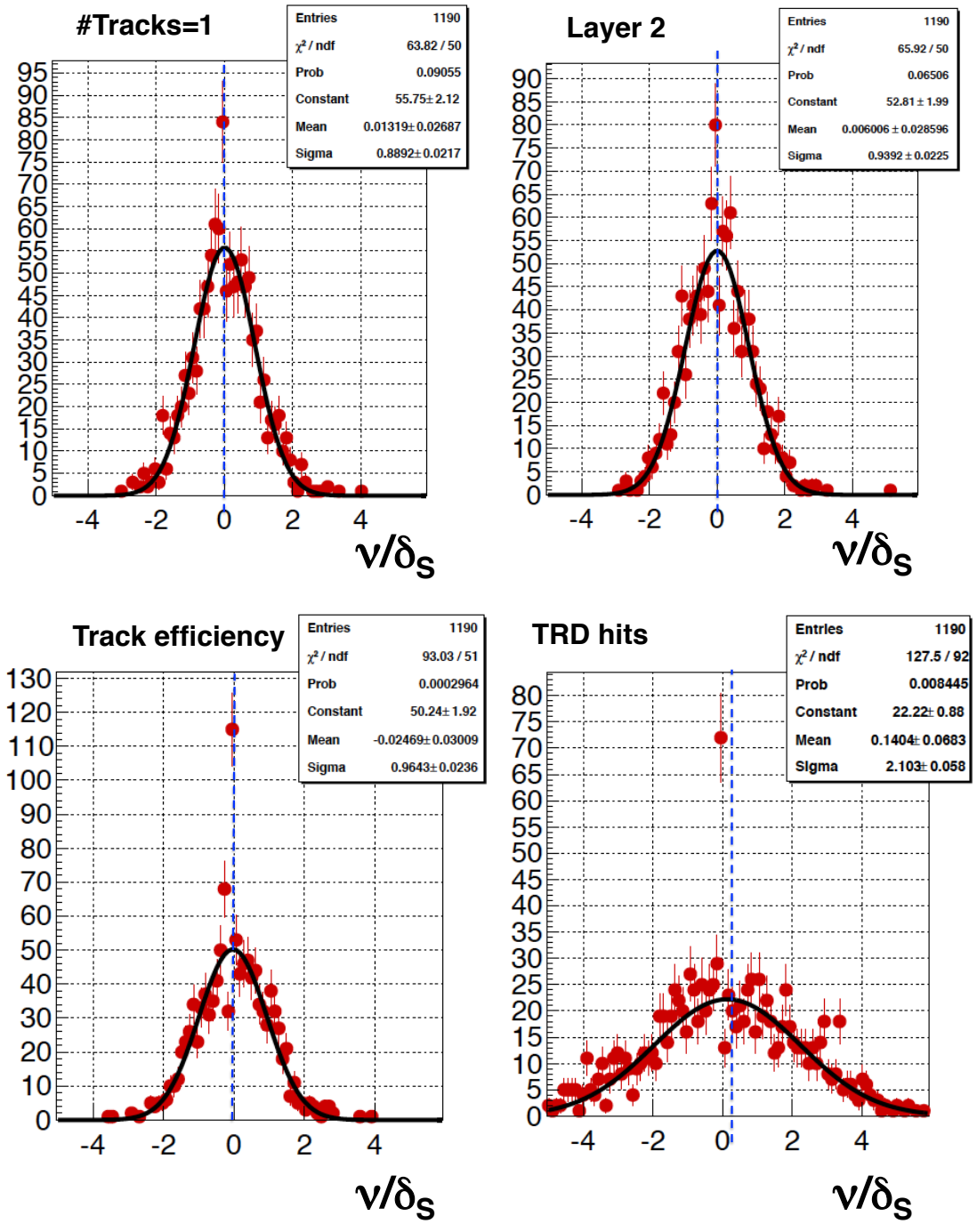

FIGURE 5.15: ν/δ_S distribution for the single track efficiency, layer 2 efficiency, track efficiency and TRD hits efficiency. A gaussian fit is performed over the distributions in order to evaluate the energy/time correlations according to the method described in this section.

Chapter 6

Electrons and positrons fluxes in time

6.1 Electrons and positrons fluxes results

Using the techniques described in chapters **??** the electrons and positrons fluxes have been measured from AMS data in the energy range 0.5–40. GeV and in different 32 time intervals of 27 days starting on 1^{st} July 2011.

The electron fluxes multiply by E^3 as a function of the energy obtained in the 32 different time interval is shown in figure 6.3. Each color corresponds to a different time interval of 27 days and it is clear that the intensity of the flux in the low energy part decrease with time as also shown in figure 6.4.

The same features can be observed on the obtained results for positrons fluxes in the 32 time intervals as shown in figures **??** and **??**.

Figure 6.5 shows the normalized fluxes in each time interval respect to the time integrated fluxes both for electrons and positrons in two different energy bin. Electrons and positrons following the same trend (more evident at low energies) with the intensity that decrease as a function of time. The results are in agreement with the solar activity that occurde during the data taking. The data analyzed have been taken during the 24^{th} solar cycle[1] that began on January 4, 2008 [86]. The recent solar cycle is represented in terms of sunspot number in figure 6.6. Each

[1]The solar cycles are count since 1755, when extensive recording of solar sunspot activity began[85].

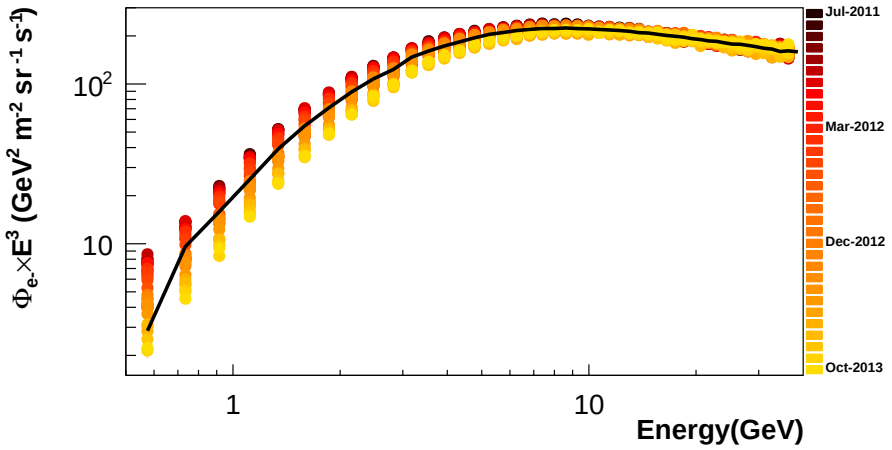

FIGURE 6.1: Electron fluxes multiply by E^3 as a function of the energy obtained in the 32 different time interval. Each color corresponds to a different time interval of 27.

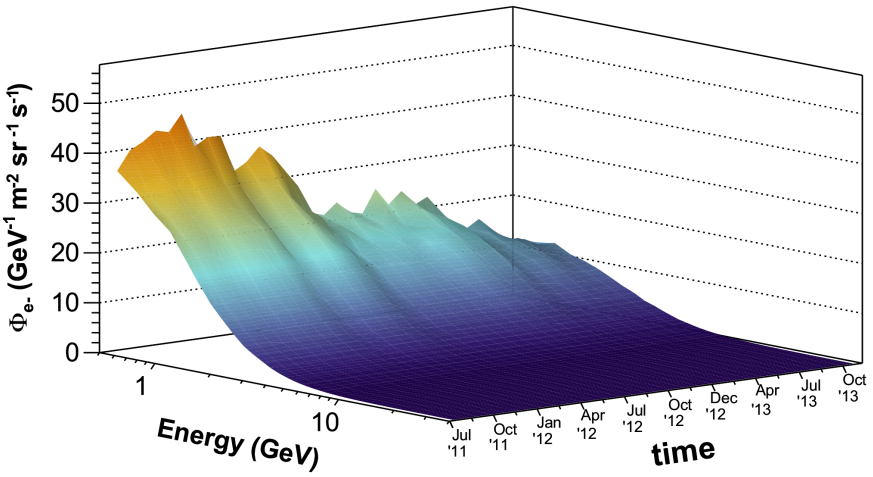

FIGURE 6.2: Electron fluxes as a function of energy and time. The decrease of the intensity at low energies as a function of time is clearly visible.

point represent the monthly averaged sunspots number and the line represents a smoothed version of the monthly averaged data. The data are still preliminary, however, while awaiting final confirmation, all evidence points to the most recent solar maximum having peaked at 82 sunspot number in April, 2014[87]. The data used for this analysis have been taken in a period during which the solar activity was reaching its maximum as already discussed in section 1.4.2 this means that the intensity of comics rays should decrease with time as indeed observed in figure 6.5.

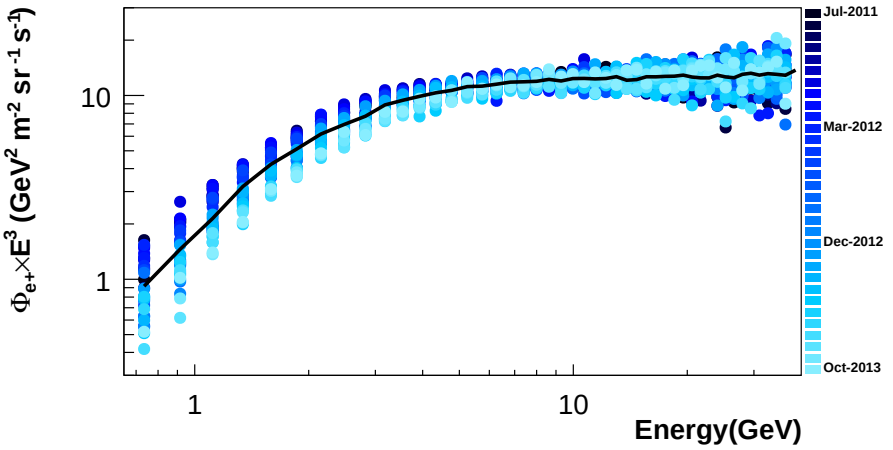

FIGURE 6.3: Positrons fluxes multiply by E^3 as a function of the energy obtained in the 32 different time interval. Each color corresponds to a different time interval of 27.

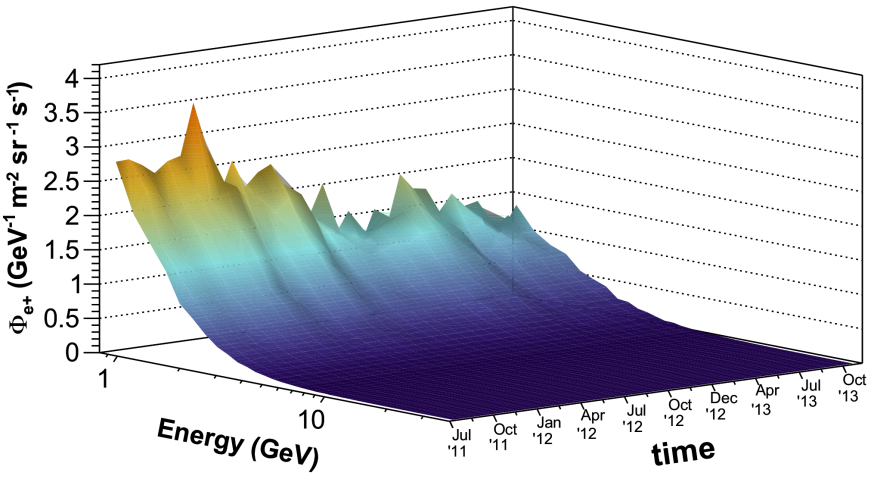

FIGURE 6.4: Positrons fluxes as a function of energy and time. The decrease of the intensity at low energies as a function of time is clearly visible.

Together with the linearity behavior with time due to the reaching maximum solar activity, the trend of fluxes as a function of time is also affected by an annual modulation due to Earth-Sun distance and by the *Furbush decreases*. *Furbush decrease* is a rapid decrease in the observed galactic cosmic ray intensity following a single events like solar flares. Over the following several days from the flare, the solar cosmic ray intensity returns to normal. The flare ejects clouds of electrons, ions, and atoms through the corona of the sun into space. These clouds typically reach Earth a day or two after the event. On ISS the reduction of comics rays intensity during a *Furbush decrease* can reach also 30%. The magnitudo of the *Furbush decrease*

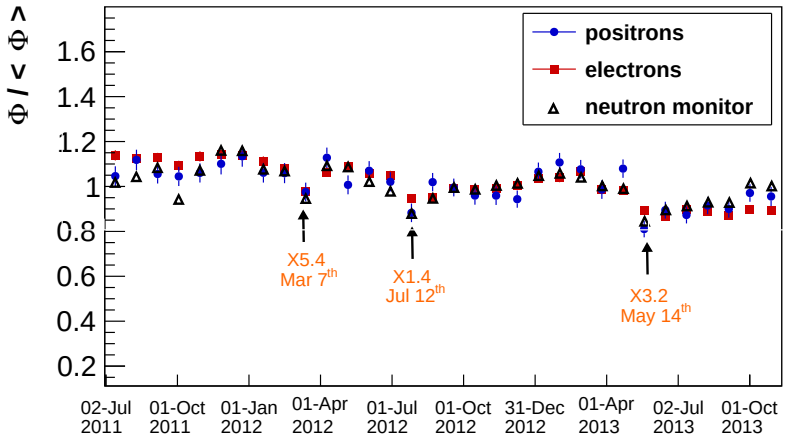

FIGURE 6.5: Normalized electrons and positrons fluxes in each time interval respect to the time integrated fluxes in two different energy bin.

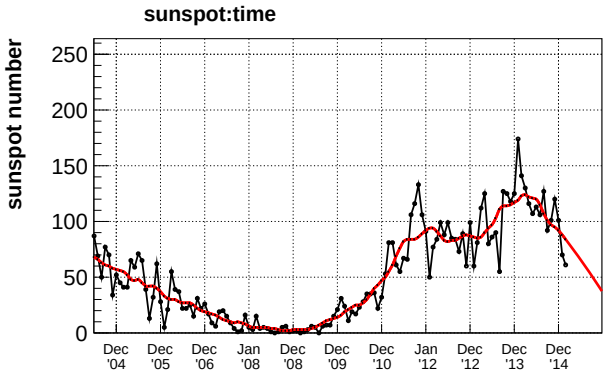

FIGURE 6.6: Sunspot number as a function of time. Each point represent the monthly averaged sunspots number and the line represents a smoothed version of the monthly averaged data. Data taken from [87].

depends from the intensity of the solar flare. The stronger solar flares that occurred during the period used for the analysis are clearly visible as a flux intensity decrease on electrons and positrons fluxes reported in figure 6.5.

Figure ?? shows the flux in time for electrons and positrons in one energy bin with a superimposed fit performed with a polynomial of grade one. The result of the fit shows that the annual variation ($d\Phi/dt$) for the electrons flux and for positrons flux with energy $\sim$4 GeV is respectively of 9.29$\pm$0.31% and 6.41$\pm$0.69%. The observed variation in time is greeter that the systematics errors on the measurements (shown by the light blue colored band around the fit). This confirmed the observe trend is due to a physics causes not to a wring measurement. The difference in the flux

variation between electrons and positrons is due to charge-sign dependent effect of solar modulation. This can be clearly see also on there ratio between the positrons and electrons flux as shown in figure ?? which reports the ratio between fluxes as a function of time in one energy bin. The annual variation observed for the fluxes ratio at energy $\sim$4 GeV is 3.76$\pm$1.01%.

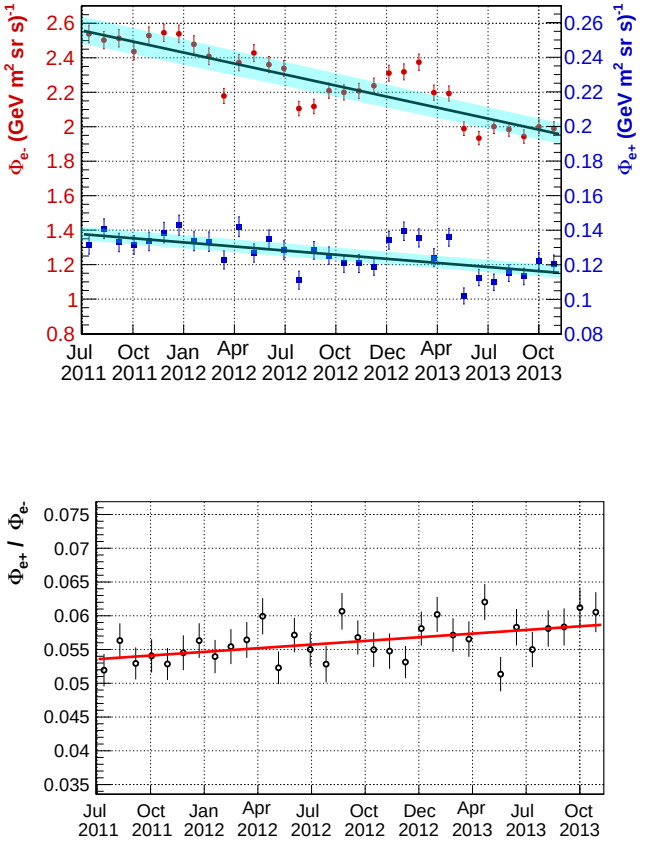

The annual variation of fluxes and their ratio as a function of energy is reported in figure 6.7

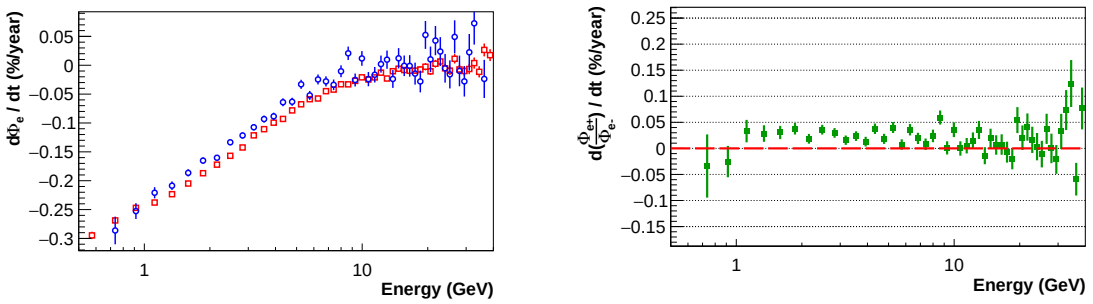

FIGURE 6.7

6.1.1 Cross-check

As cross check of the analysis the same techniques used for the results shown above have been also used to evaluate the electrons and positrons fluxes on the AMS data taken in the first 30 months and the obtained results have been compared with the published fluxes [46]. Both measurements are performed on data taken in the same period, this means that they should be equally affected by the solar modulation and hence they should be in agreement. The comparison between the fluxes obtained with the two independent analysis are shown in figure 6.9 and their difference divide by the errors is shown in figure **??**. The fluxes obtained with the analysis techniques used for this work are in good agreement with the published ones and their differences are inside 1 sigma.

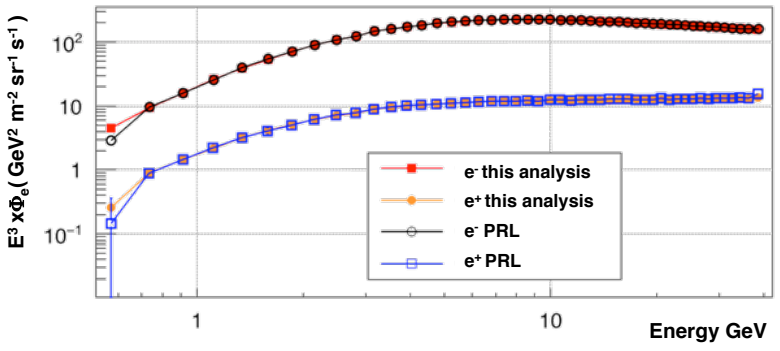

FIGURE 6.8: Comparison between the electrons and positrons fluxes obtained from this work and the published ones [46].

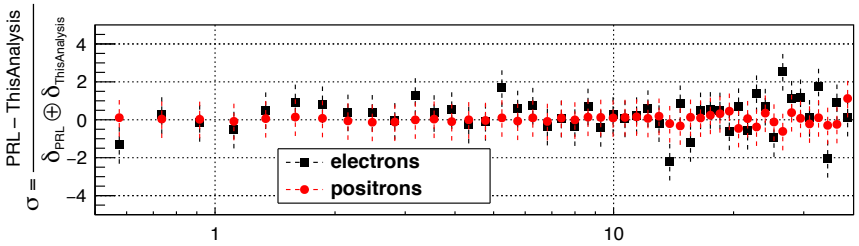

FIGURE 6.9: Differences between the electrons and positrons fluxes obtained from this work and the published ones [46] divided by the errors.

Another cross-check that has bene done is the comparison of the fluxes obtained in each time interval with the time integrated ones. The two results should be in agreement except at low energy due to the solar modulation. In figure 6.11 the ratio

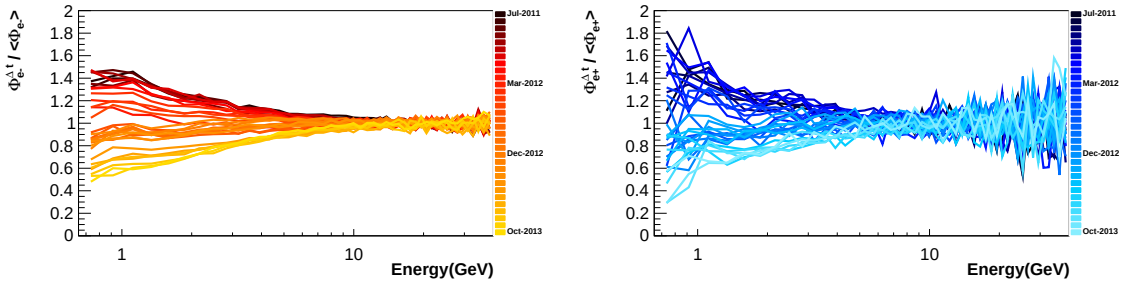

FIGURE 6.10

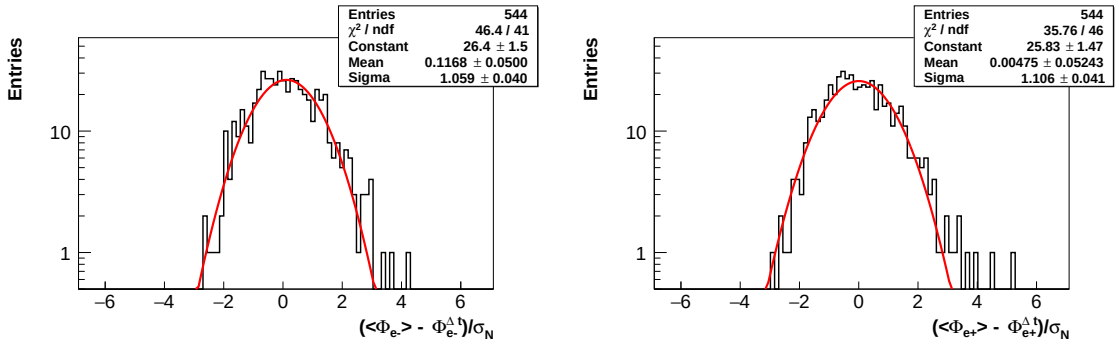

FIGURE 6.11

between the fluxes evaluated in all the 32 time interval and the time integrated flux is shown both for electrons and positrons. The fluxes in each time interval are compatible with the time integrated one and the discrepancy that can be observed for energies ¿10 GeV is due to statistical fluctuations. This is confirmed in figure **??** in which is reported the the value of normalized flux for energies ¿20 GeV divided by the statistical errors. The obtained distribution is a gaussian with sigma 1.

6.2 Fluxes uncertainties

Severals errors for the flux measurement have been taken into account in each time and energy intervals. They came from the number of electrons and positrons events ($N_{e^{\pm}}$), from the acceptance correction (K), from Energy reconstructed by ECAL and from the knowledge of charge confusion correction (CC) and they are:

- statistics errors related to $N^{e^{\pm}}$ (see section 4.4.1)
  - σ_N: Statistical error on the number of electrons and positrons extracted with the fitting procedure;
- systematic errors related to $N^{e^{\pm}}$

  - σ_{stat_templ}: Error coming from the fine statistic of templates used in the fitting procedure applied for the extraction of the number of electrons and positrons;
  - σ_{sel_templ}: Error coming from the selection applied in order to obtain the templates used in the fitting procedure applied for the extraction of the number of electrons and positrons;

- systematic errors related to K (see section **??**)
  - σ_K^{abs}: error that takes into account the deviation of $K(\Delta E)$ from 1;
  - σ_K^{stab}: error that takes into account the stability in time of K;
  - σ_K^{par}: error that takes into account the errors on parameter resulting from the fit performed above 2 GeV on $K(\Delta E, \Delta t)$;
  - σ_K^{res}: gives the goodness of the fit performed above 2 GeV on $K(\Delta E, \Delta t)$.

- systematic errors related to CC (see section **??**) (see section **??**)
  - σ_{CC}

- systematic errors related to the Energy reconstruction (see section **??**)
  - σ_{ECAL_stab}
  - σ_{ECAL_abs}

The errors due to $N^{e^{\pm}}$ and CC have been already discussed in chapter 4, as the errors on K has been discussed in chapter 3. In the next section will be discussed the the errors coming from the reconstructed energy from ECAL.

According to the kind of correlation bin to bin in time or energy, the errors can be divided into 4 different (but not disjoint) categories:

1. errors that do not correlate bin at different times
2. errors that correlate bin at different times
3. errors that do not correlate bin at different energies
4. errors that correlate bin at different energies

The classification of errors according to the criteria shown above, is reported in table **??**.

		time bins		energy bins		coming from:
		corr	uncorr	corr	uncorr	
statistic	σ_N	no	yes	no	yes	$N^{e^\pm}$
sistematic	σ_{stat_tmpl}	no	yes	no	yes	$N^{e^\pm}$
	σ_{sel_tmpl}	yes	no	no	yes	$N^{e^\pm}$
	σ_K^{abs}	yes	no	70% yes	30% yes	K
	σ_K^{stab}	no	yes	no	yes	K
	σ_K^{par}	yes	no	no	yes	K
	σ_K^{res}	yes	no	no	yes	K
	σ_{CC}	yes	no	yes	no	CC
	σ_{ECAL_stab}	no	yes	yes	no	Energy measurement
	σ_{ECAL_abs}	yes	no	yes	no	Energy measurement

Conclusion

The measurement of energy spectra of galactic cosmic rays electrons and positrons provides fundamental information regarding the origin and propagation of cosmic rays. Moreover, the $e^{\pm}$ spectrum measured at Earth can potentially show indirect presence of Dark Matter. A correct understanding of galactic $e^{\pm}$ fluxes is fundamental for a correct interpretation of the measured data. Cosmic rays spectrum measured near Earth is significantly affected by the solar activity in the low energy part (E<20 GeV). The solar activity changes in time inducing a time dependence of the measured CR. A comprehensive description of the cosmic radiation must therefore include the transport and modulation of cosmic rays inside the heliosphere.

In this dissertation we presented a new precise measurement of the e^+ and e^- fluxes in the energy range 0.5–40 GeV based on the statistics collected during the first 30 months of AMS-02 operation in space. Starting from 1^{st} July 2011, the $e^{\pm}$ differential energy spectra have been measured in 48 energy bins following their evolution in time with a granularity of 27 days, for a total of 32 measurements. This is the first direct measurement ever performed at these energies with such a detailed time binning on e^- and on e^+.

A decrease of the $e^{\pm}$ fluxes with time has been observed which is consistent to solar activity in the period of our measurements. Indeed, the beginning of the 24th solar cycle was in January 2008, and our data were collected in 2011-2013 when approaching to the maximum of the solar cycle, which occurred in April 2014. A good agreement was also found with the time evolution of the neutron monitors counting rates on ground, which are related to total CR flux intensity reaching the Earth atmosphere.

The simultaneous measurement of e^- and e^+ has also allowed to study differences of the solar modulation effects which are related only to the charge-sign of the

particles. For example in the energy bin 4.12–4.54 GeV the annual variation observe on electrons and positrons fluxes is respectively (9.29±0.31)% and (6.41±0.69)%.

These new accurate experimental data will be of great relevance to improve the current models of CR propagation in the heliosphere, therefore allowing a deeper understanding of the local interstellar spectrum of cosmic rays.

A deep understanding of detector related effects in the flux measurement was gained during this work and specific analysis techniques were developed to allow the prompt extension of this measurement as more data will be collected by the experiment. The analysis of the data set up to September 2014 is already on-going, showing even larger charge-sign dependent effects at the solar maximum. Since, AMS-02 is foreseen to operate for the entire ISS lifetime, up to 2024, it will be able to follow in detail the time evolution of the e^+ and e^- fluxes along a full solar cycle.

Bibliography

[1] J. Chang *et al. An excess of cosmic ray electrons at energies of 300-800*[*thinsp*]*gev.* Nature*, 456(7220):362–365, 2008.*

[2] O. Adriani et al. An anomalous positron abundance in cosmic rays with energies 1.5-100[*thinsp*]*gev.* Nature*, 458:607–609, 2009.*

[3] M. Ackermann et al. Measurement of separate cosmic-ray electron and positron spectra with the fermi large area telescope. Phys. Rev. Lett.*, 108(1):011103, 2012.*

[4] M. Aguilar et al. First result from the alpha magnetic spectrometer on the international space station: Precision measurement of the positron fraction in primary cosmic rays of 0.5˘350 gev. Phys. Rev. Lett.*, 110:141102, 2013.*

[5] L. Accardo et al. *High statistics measurement of the positron fraction in primary cosmic rays of 0.5˘500 gev with the alpha magnetic spectrometer on the international space station.* Phys. Rev. Lett.*, 113:121101, 2014.*

[6] Ahn, H. S et al. Measurements of cosmic-ray secondary nuclei at high energies with the first flight of the cream balloon-borne experiment. Astroparticle Physics*, 30:133–141, 2008.*

[7] T. Antoni et al. The cosmic-ray experiment kascade. Nuclear Instruments and Methods in Physics Research A*, 513:490–510, 2003.*

[8] G. Navarra, T. Antoni, W.D. Apel, F. Badea, K. Bekk, et al. Kascade-grande: a large acceptance, high-resolution cosmic-ray detector up to 10 ^{18} *ev.* Nuclear Instruments and Methods in Physics Research A*, 518:207–209, 2004.*

*[9] N. Chiba et al. Akeno giant air shower array (agasa) covering 100-km**2 area.* Nuclear Instruments and Methods in Physics Research A*, 311:338–349, 1992.*

[10] J. Abraham et al. Properties and performance of the prototype instrument for the pierre auger observatory. Nuclear Instruments and Methods in Physics Research Section A : Accelerators, Spectrometers, Detectors and Associated Equipment*, 523:50–95, 2004.*

[11] J.A. Hinton. The status of the hess project. New Astron.Rev.*, 48:331–337, 2004.*

[12] Daniel Ferenc. The {MAGIC} gamma-ray observatory. Nuclear Instruments and Methods in Physics Research A*, 553(1–2):274 – 281, 2005.*

[13] R.M. Baltrusaitis et al. The utah fly's eye detector. Nuclear Instruments and Methods in Physics Research A*, 240:410–428, 1985.*

[14] H. Kawai et al. Telescope array experiment. Nuclear Physics B - Proceedings Supplements*, 175–176:221–226, 2008.*

[15] K.A. Olive et al. Particle data group. Chin. Phys. C*, 38, 2014.*

[16] E. Fermi. On the origin of the cosmic radiation. 75:1169–1174, 1949.

[17] Longair, Malcolm S. High energy astrophysics, volume 2.

[18] V. Berezinsky, A. Gazizo and S. Grigorieva. Phys. Rev.*, D74, 043005, 2006.*

[19] K. Greisen. End to the cosmic-ray spectrum? Phys. Rev. Lett.*, 16:748, 1966.*

[20] A. W. Strong, I. V. Moskalenko and V. S. Ptuskin. Cosmic-ray propagation and interactions in the galaxy. Annual Review of Nuclear and Particle Science*, 57:285, 2007.*

[21] R. Beck. Galactic and extragalactic magnetic fields a concise review. Astrophys. Space Sci. Trans.*, 5:43, 2009.*

[22] G. Brunetti et al. Alfvenic reacceleration of relativistic particles in galaxy clusters: Mhd waves, leptons and hadrons. Monthly Notices of the Royal Astronomical Society*, 350:1174, 2004.*

[23] Galprop code. http://galprop.stanford.edu/, .

[24] Dragon code. http://dragon.hepforge.org/DRAGON/Home.html, .

[25] *Craig L. Sarazin. The energy spectrum of primary cosmic-ray electrons in clusters of galaxies and inverse compton emission.* The Astrophysical Journal, *520:529–547, 1999.*

[26] *Swarm (geomagnetic leo constellation), . URL* https://directory.eoportal.org/web/eoportal/satellite-missions/s/swarm#ipkeJ1119Herb .

[27] *C.Z. Stormer.* Astroph., *1:237, 1930.*

[28] *C.Z. Stormer. The polar aurora. 1955.*

[29] *L. J. Gleeson and W. I. Axford. Cosmic rays in the interplanetary medium.* The Astrophysical Journal, *149, 1967.*

[30] *L. J. Gleeson and W. I. Axford. Solar modulation of galactic cosmic rays.* The Astrophysical Journal, *154, 1968.*

[31] *Parker, E.N. Dynamics of the interplanetary gas and magnetic fields.* Astrophys. J., *128:664–676, 1958.*

[32] *R. L. Golden* et al. *Measurement of the positron to electron ratio in the cosmic rays above 5 gev.* Astrophysical Journal, *457:103–106, 1996.*

[33] *M. Boezio* et al. *The cosmic-ray electron and positron spectra measured at 1 au during solar minimum activity.* The Astrophysical Journal, *532(1):653, 2000.*

[34] *S. Torii et al. The energy spectrum of cosmic-ray electrons from 10 to 100 gev observed with a highly granulated imaging calorimeter.* The Astrophysical Journal, *559:973, 2001.*

[35] *K. Yoshida* et al. *Cosmic-ray electron spectrum above 100 gev from ppb-bets experiment in antarctica.* Advances in Space Research, *42:1670–1675, 2008.*

[36] *S. W. Barwick* et al. *The energy spectra and relative abundances of electrons and positrons in the galactic cosmic radiation.* The Astrophysical Journal, *498 (2):779, 1998.*

[37] *M. A. DuVernois* et al. *Cosmic-ray electrons and positrons from 1 to 100 gev: Measurements with heat and their interpretation.* The Astrophysical Journal, *559(1):296, 2001.*

[38] C. Grimani et al. *Measurements of the absolute energy spectra of cosmic-ray positrons and electrons above 7 gev.* Astronomy and Astrophysics, *392:287–294, 2002.*

[39] R. L. Golden et al. *Observations of cosmic ray electrons and positrons using an imaging calorimeter.* Astrophysical Journal, *436:769–775, 1994.*

[40] J. Alcaraz et al. *Leptons in near earth orbit.* Physics Letters B, *484:10–22, 2000.*

[41] M. Aguilar et al. *Cosmic-ray positron fraction measurement from 1 to 30 gev with ams-01.* Physics Letter B, *646:145–154, 2007.*

[42] O. Adriani et al. *Cosmic-ray electron flux measured by the pamela experiment between 1 and 625 gev.* Physical Review Letters, *106:201101, 2011.*

[43] M. Ackermann et al. Fermi lat observations of cosmic-ray electrons from 7 gev to 1 tev. Phys. Rev. D, *82(9):092004, 2010.*

[44] F. Aharonian et al. *Energy spectrum of cosmic-ray electrons at tev energies.* Physical Review Letters, *101(26):261104, 2008.*

[45] F. Aharonian et al. *Probing the atic peak in the cosmic-ray electron spectrum with h.e.s.s.* Astron. Astrophys., *508:561–564, 2009.*

[46] M. Aguilar et al. Electron and positron fluxes in primary cosmic rays measured with the alpha magnetic spectrometer on the international space station. Phys. Rev. Lett., 113:121102, 2014.

[47] M. Aguilar et al. Precision measurement of the $(e^+ + e^-)$ *flux in primary cosmic rays from 0.5 gev to 1 tev with the alpha magnetic spectrometer on the international space station.* Phys. Rev. Lett., *113(221102), 2014.*

[48] Cholis, Ilias and Hooper, Dan. Dark matter and pulsar origins of the rising cosmic ray positron fraction in light of new data from the ams. Phys. Rev. D, *88:023013, 2013.*

[49] Kopp, Joachim. Constraints on dark matter annihilation from ams-02 results. Phys. Rev. D, *88:076013, 2013.*

[50] Bergström, Lars, Bringmann, Torsten, Cholis, Ilias, Hooper, Dan, and Weniger, Christoph. New limits on dark matter annihilation from alpha magnetic spectrometer cosmic ray positron data. Phys. Rev. Lett.*, 111:171101, 2013.*

[51] Blum, Kfir, Katz, Boaz, and Waxman, Eli. Ams-02 results support the secondary origin of cosmic ray positrons. Phys. Rev. Lett.*, 111:211101, 2013.*

[52] Torsten Bringmann, Fiorenza Donato, Roberto A. Lineros. Radio data and synchrotron emission in consistent cosmic ray models. arXiv:1106.4821 [astro-ph.GA]*, 2012.*

[53] M. Aguilar et al. *The alpha magnetic spectrometer (ams) on the international space station: Part i esults from the test flight on the space shuttle.* Physics Reports*, 366:331–405, (2002).*

[54] P. Chardonnet et al. *Production of anti-matter in our galaxy.* Physics Letters B*, 409:313–320, (1997).*

[55] A. Castellina , F. Donato. Diffusion coefficient and acceleration spectrum from direct measurements of charged cosmic ray nuclei. Astroparticle Physics*, (24): 146–159, 2005.*

[56] The AMS Collaboration. Ams on iss: Application of particle physics technology to manned interplanetary flight . to be published on nuclear and instruments methods. AMS collaboration internal report*, .*

[57] B. Alpat et al. The internal alignment and position resolution of the ams-02 silicon tracker determined with cosmic-ray muons. Nucl. Instrum. Methods Phys. Res., Sect. A*, 613(2):207–217, 2010.*

[58] K. Lubelsmeyer et al. Upgrade of the alpha magnetic spectrometer (ams-02) for long term operation on the international space station (iss). Nucl. Instrum. Methods Phys. Res., Sect. A*, 654(1):639, 2011.*

[59] T. Bruch and W. Wallraff. The anti-coincidence counter shield of the ams tracker. Nuclear Instruments and Methods in Physics Research A*, 572:505–507, 2007.*

[60] W. Sun and Z. Weng. Measurement of the absolute charge of cosmic ray nuclei with the ams transition radiation detector. ICRC 2013 proceedings (2013). To be published.

[61] K. Andeen M. Heil and F. Spada. Operations and alignment of the ams-02 transition radiation detector. ICRC 2013 proceedings (2013). To be published.

[62] C. Adlo et al. The ams-02 lead-scintillating fibres electromagnetic calorimeter. Nuclear Instruments and Methods in Physics Research A, *714:147–154, 2013.*

[63] F. Cervelli et al. A reduced scale e.m. calorimeter prototype for the ams-02 experiment. Nuclear Instruments and Methods in Physics Research Section A: Accelerators, Spectrometers, Detectors and Associated Equipment, *490(1–2): 132 – 139, 2002.*

[64] L. Basara. Energy calibration with mip in space and charge measurement with ams-02 electromagnetic calorimeter. ICRC 2013 proceedings (2013). To be published.

[65] G. Grindhammer and S. Peters. The parameterized simulation of electromagnetic showers in homogeneous and sampling calorimeters. arXiv: hep-ex/0001020 [hep-ex], 1993.

[66] S. Di Falco. Performance of the ams-02 electromagnetic calorimeter in space. In ICRC 2013 proceedings (2013). To be published.

[67] M. Vecchi. A 3-dimensional electromagnetic shower characterization and its application to ams-02 pointing capability. In ICRC 2013 proceedings (2013). To be published.

[68] The AMS Collaboration. Ams on iss : Construction of a particle physics detector on the international space station. technical design report (unpublished). .

[69] C. Lin. Trigger logic design specifications. Internal Note, *2005.*

[70] C. Lin. Trigger logic design specifications. Internal AMS-02 note, *2005.*

[71] A. Kounine and V. Koutsenko. Flight software for xdr and jinx nodes in ams-02. AMS internal notes., *2011.*

[72] J. van Es. Ams02 tracker thermal control system overview and spin-off for future spacecraft cooling system developments. Proc. of IAC C2.7.1, *2009.*

[73] R. Brun et al. *Root web page, 2001. URL* http://root.cern.ch/.

[74] M. Aguilar et al. Precision measurement of the proton flux in primary cosmic rays from rigidity 1 gv to 1.8 tv with the alpha magnetic spectrometer on the international space station. Phys. Rev. Lett., *114:171103, 2015.*

[75] William R. Leo. Techniques for nuclear and particle physics experiments.

[76] G. Grindhammer and S. Peters. The parameterized simulation of electromagnetic showers in homogeneous and sampling calorimeters. arXiv: hep-ex/0001020 [hep-ex], *1993.*

[77] B.Roe et al. *Boosted decision trees as an alternative to artificial neural networks for particle identification.* NIM, *A543:577–584, (2005).*

[78] C. Corti M. Incagli and V. Vagelli. A study for an ecal standalone classication algorithm using the boosted decision tree (bdt) technique. AMS internal notes., *2014.*

[79] M. Heil et al. Operations and alignment of the ams-02 transition radiation detector. ICRC Proceeding (to be published), *2013.*

[80] Z. Weng". Particle Identication Using Transition Radiation Detector and Precision Measurement of Cosmic Ray Positron Fraction with the AMS-02 Experiment. *PhD thesis, Sun Yat-Sen University, 2013.*

[81] M. Duranti. Measurement of the Atmospheric Muon Flux on Ground with the AMS-02 Detector. *PhD thesis, Universit'egli Studi di Perugia, Italie, 2011.*

[82] The roofit method, . URL https://root.cern.ch/drupal/content/roofit.

[83] W. Verkerke and D. Kirkby. The roofit toolkit for data modeling, 2003.

[84] V. Vagelli. Measurement of the cosmic $(e^+ + e^-)$ flux from 0.5 GeV to 1 TeV with the Alpha Magnetic Spectrometer (AMS-02) on the International Space Station. *PhD thesis, Fakultat fur Physik der Karlsruher Institut fur Technologie (KIT), 2014.*

[85] R.P. Kane. Some implications using the group sunspot number reconstruction. Solar Physics, *205(2):383–401, 2002. ISSN 0038-0938. doi: 10.1023/A:1014296529097. URL* http://dx.doi.org/10.1023/A%3A1014296529097.

[86] Dr. Tony Phillips. "solar cycle 24 begins".nasa, Retrieved 2010-05-29. URL http://science.nasa.gov/science-news/science-at-nasa/2008/10jan_solarcycle24/.

[87] "solar cycle progression — noaa / nws space weather prediction center", Retrieved 2015-07-06. URL www.swpc.noaa.gov.